Local investigations of gas-liquid mass transfer around Taylor bubbles flowing in straight and meandering millimetric channels using a colorimetric method

Lixia Yang

Université Fédérale

Toulouse Midi-Pyrénées

THÈSE

En vue de l'obtention du

DOCTORAT DE L'UNIVERSITÉ DE TOULOUSE

Délivré par *Institut National des Sciences Appliquées de Toulouse (INSA de Toulouse)*
Discipline ou spécialité : *Génie des Procédés et de l'Environnement*

Présentée et soutenue par ***Lixia YANG***
Le *24/03/2017*

Titre : ***Local investigations of gas-liquid mass transfer around Taylor bubbles flowing in straight and meandering millimetric channels using a colorimetric method***

JURY

M. Philipp RUDOLF VON ROHR	ETH Zürich	Rapporteur
Mme. Katharina ZAHRINGER	University of Magdeburg	Rapporteure
M. Yves GONTHIER	Université de Savoie	Examinateur
M. Jean-Marc COMMENGE	Université de Lorraine	Examinateur
M. Gilles HEBRARD	INSA de Toulouse	Directeur de thèse
M. Christophe GOURDON	INP de Toulouse	Directeur de thèse
M. Nicolas DIETRICH	INSA de Toulouse	Co-Directeur de thèse
Mme. Karine LOUBIERE	CNRS	Co-Directrice de thèse

Ecole doctorale : *ED MEGEP*
Unité de recherche : *Laboratoire d'Ingénierie des Systèmes Biologiques et des Procédés & Laboratoire de Génie Chimique*
Directeur(s) de Thèse : *Prof. Gilles HEBRARD & Prof. Christophe GOURDON (Directeurs de thèse)*
Dr. Nicolas DIETRICH & Dr. Karine LOUBIERE (Co-Directeur/trice de thèse)

Acknowledgement

I sincerely thank Prof. Yves Gonthier, the president of thesis' jury, and also extend my sincere gratitude to the reviewers of my dissertation, Prof. Philipp Rudolf von Rohr and Dr. Katharina Zähringer, for your insightful comments and encouragement, but also for the hard questions which incented me to widen my research from various perspectives. Thank you very much Dr. Jean-Marc Commenge, and I appreciate your kind suggestions and useful comments which help to further improve and complete the dissertation.

I am extremely grateful to my supervisors: Prof. Gilles HEBRARD and Prof. Christophe GOURDON, for your guidance, devotion, and continual support throughout my study in France. Your mentorship, motivation and friendship guided me during this research to achieve our objectives. Your serious attitude and broad vision of scientific research will always impact me in my future work.

I would like to give my special appreciation to my co-supervisors: Dr. Karine LOUBIERE and Dr. Nicolas DIETRICH, for your 'step-by-step' guidance, leading me into the area of visualization of gas-liquid mass transfer and chemical engineering. You guide me not only how to prove a hypothesis and practice an idea theoretically and experimentally, but also how to improve the quality of scientific publications. My special big thanks to you, Karine! for your endless guidance, patience, support and additionally for your always enthusiastic interest in discussing the new results with me, and making every effort to help me and being always ready to spend time to tutor me.

Thank you so much all the colleagues in LISBP and LGC, without your kind help, this work could not be finished. Thanks a lot José Moreau, without your help, it would be impossible to implement the colorimetric method in microchannels. Thank you Claude Le Men, your kind help in image post-treatment really facilitate my analysis of the experimental images. Thank you so much Vincent Loisel and Franck Dunglas for your humor and kind help in fabrication and maintenance of my reactors, without your help, the essential part of my work would not be completed. Thank you Alain Pontier for your kind help in the design of the microchannel devices.

Thank you Bernard Galy for the transportation of the camera between LISBP and LGC. Thank you…

I would like also to thank my supervisor Prof. Youguang MA, from School of Chemical Engineering and Technology of Tianjin University, who firstly introduced me to the world of scientific research and also helped me to get the opportunity of studying in France.

I am willing to thank the China Scholarship Council for the financial support of my Ph.D. study. Besides, I would love to thank a lot of Chinese friends both in Toulouse and in China. I would not write your names here, I will keep you in mind deeply, since these three years and half in France could be a dream we all shared. I hope you all will be successful in your future careers, and have a happy family. In particularly, I sincerely thank my dearest, Feishi XU, for your consistent support and encouragement for my last period of my thesis.

I would like to dedicate this work to my dearest grandma. Although you have been leaving me for almost two years, I know that you are always right beside me. Whenever I lose the way forward, your unconditional love and support could always guide me and give me the power to confront every challenge and go through all the tough days.

The last but not the least, my special appreciation and great thankfulness are dedicated to my grandpa, my parents, for your love, patience, unconditional support and motivation.

Abstract

Compact Heat-EXchanger reactors (HEX) are an important part of process intensification technology. However, most of the existed research dealing with such type of equipment is focused on the application of one-phase reactive flows. For gas-liquid reactions (e.g. hydrogenations, photooxygenations, fluorinations), few investigations have been carried out, whereas such multiphase systems still raise many fundamental questions, in particular with respect to the understanding of the coupling between transport phenomena and reaction kinetics.

With regard to this context, this thesis aims at locally studying gas-liquid mass transfer around Taylor bubbles flowing in straight and meandering millimetric channels; this is a preliminary step essential before implementing two-phase reactive systems. For that, the so-called colorimetric method was implemented. Based on the use of an oxygen-sensitive dye, this innovative method enabled the equivalent dissolved oxygen concentration field around bubbles to be visualized without any laser excitation or inserting a physical sensor, and then is convenient and user friendly.

Firstly, it was necessary to investigate the occurrence of a possible enhancement of the gas-liquid mass transfer by the chemical reaction involved. For that, as data on the associated kinetic are seldom in the literature, the reaction characteristic time was firstly estimated by carrying out experiments in a microchannel equipped with a micromixer. The diffusion coefficients of dihydroresorufin and O_2 were then determined by implementing two original optical methods in a specific co-flow microchannel device, coupled with theoretical modelling. The knowledge of these parameters enabled to calculate the Hatta number and the enhancement factor, and then to give complementary information about the reliability of the colorimetric technique to characterize the gas-liquid mass transfer in milli/micro systems.

Secondly, a special focus was made on the study of the gas-liquid mass transfer occurring in Taylor flows right after the bubble formation stage in a flow-focusing microreactor. The results highlighted that the contribution of the bubble formation stage to the overall gas-liquid mass transfer stage was very important.

Thirdly, the colorimetric technique was implemented in a meandering millimetric square channel. The gas-liquid hydrodynamics was beforehand characterized in terms of bubble length and velocity, gas hold-up, interfacial area. The evolution of equivalent oxygen concentration fields in the liquid slugs passing through one and several bends was then described. It was also observed how the flow structure (recirculation zones) inside the liquid slugs were twisted and split by the periodic bends (centrifugal effect), until reaching, after several bends, a uniform O_2 concentration inside the liquid slugs. The influence of the “turning point” joining two “straight” sections of the meandering channel was also highlighted: a slowing down of the gas-liquid mass transfer was clearly shown.

Then, for comparison purposes, studies were carried out in a straight millimetric square channel of identical diameter and compactness. As in the meandering channel, the gas-liquid hydrodynamics was characterized and mass transfer coefficients were estimated.

At last, a rigorous comparison could be made between the meandering and straight channels. It showed how and why the meandering geometry led to intensify gas-liquid mass transfer. All these findings enabled to formulate a scaling law, expressed in terms of Sherwood, Graetz and Péclet numbers, able to describe the evolution of gas-liquid mass transfer as a function of axial position and operating conditions.

Résumé

Les réacteurs-échangeurs à plaques (HEX) sont une technologie clé en intensification des procédés. Cependant, la plupart des recherches existantes portant sur ce type d'équipement ont été réalisées dans le cas d'écoulements monophasiques. Pour les réactions gaz-liquide (hydrogénations, photo-oxygénations, fluorations), peu d'études ont été conduites, laissant ainsi de nombreuses questions fondamentales non résolues, notamment en ce qui concerne la compréhension du couplage entre les phénomènes de transport et la cinétique des réactions.

Dans ce contexte, cette thèse a pour objectif d'étudier localement le transfert de matière gaz-liquide autour de bulles de Taylor en écoulement dans des canaux millimétriques droits et ondulés. Ceci constitue une étape préliminaire indispensable avant la mise en œuvre de systèmes réactifs diphasiques. Pour cela, une méthode dite colorimétrique a été mise en œuvre. Basée sur l'utilisation d'un colorant sensible à l'oxygène, elle permet de mesurer les champs de concentration équivalente en oxygène dissous autour des bulles, et cela sans aucune excitation laser ou l'insertion d'un capteur physique.

Il a d'abord été nécessaire de déterminer si une possible accélération du transfert de matière gaz-liquide pouvait avoir lieu en présence de la réaction chimique utilisée. Pour cela, le temps caractéristique de la réaction a été quantifié grâce à des expériences dans un micro-canal équipé d'un micro-mélangeur. Les coefficients de diffusion du colorant et de l'oxygène ont été ensuite déterminés en couplant des techniques optiques originales dans un dispositif microstructuré spécifique de type *co-flow*, avec une modélisation théorique. La connaissance de ces paramètres a permis de calculer le nombre de Hatta et le facteur d'accélération, et de définir les conditions d'application de la technique colorimétrique pour caractériser le transfert de matière gaz-liquide en milli/micro systèmes.

La deuxième phase de ce travail s'est focalisée sur l'étape de formation des bulles de Taylor dans un microréacteur de type *flow-focusing*. Les résultats obtenus ont mis en évidence que la contribution de l'étape de formation de bulles est prépondérante dans le mécanisme global transfert de matière gaz-liquide.

Ensuite, la technique colorimétrique a été mise en œuvre dans un canal carré millimétrique ondulé. Les paramètres caractéristiques de l'hydrodynamique gaz-liquide ont été préalablement caractérisés (taille et vitesse des bulles, rétention de gaz, aire interfaciale). L'évolution des champs de concentration en oxygène dissous dans les bouchons liquides le long du canal ondulé a ensuite été décrite. Il a été observé comment la structure de l'écoulement (zones de recirculation) à l'intérieur de la phase liquide est modifiée par la présence des coudes (effet centrifuge), jusqu'à atteindre, après plusieurs coudes, une concentration d'oxygène uniforme à l'intérieur des bouchons liquides. L'influence négative sur le transfert de matière du large coude liant les deux sections rectilignes du canal ondulé a été également mesurée.

Par la suite, afin d'évaluer la plus-value d'une géométrie ondulée de canal, une étude a été réalisée dans un canal droit de même diamètre et compacité. Comme pour le canal ondulé, les paramètres hydrodynamiques gaz-liquide ont été déterminés ainsi que les coefficients de transfert de matière.

Enfin, une comparaison rigoureuse a pu être effectuée entre les différentes géométries de canaux (ondulé et droit). Elle a permis de montrer comment et pourquoi une géométrie ondulée permet d'intensifier le transfert de masse gaz-liquide (notamment en terme d'efficacité de transfert). L'ensemble de ces résultats ont conduit à la formulation d'une loi d'échelle, exprimée en termes de nombres de Sherwood, de Graetz et de Péclet, capable de décrire l'évolution du transfert de matière gaz-liquide en fonction de la position axiale dans le canal et des conditions opératoires mises en œuvre.

LIST OF PUBLICATIONS

Journal Publications

1. Yang, L., Dietrich, N., Loubière, K., Gourdon, C., & Hébrard, G. (2016). Visualization and characterization of gas–liquid mass transfer around a Taylor bubble right after the formation stage in microreactors. ***Chemical Engineering Science***, 143, 364-368.
2. Yang, L., Dietrich, N., Hébrard, G., Loubière, K., & Gourdon, C. (2017). Optical methods to investigate the enhancement factor of an oxygen-sensitive colorimetric reaction using microreactors. ***AIChE Journal***, 63, 2272–2284.
3. Yang, L., Loubière, K., Dietrich, N., Claude, L.M., Gourdon, C., Hébrard, G. (2017) Local investigations on the gas-liquid mass transfer around Taylor bubbles flowing in a meandering millimetric square channel. ***Chemical Engineering Science***, 165, 192-203.

Conference Contributions

1. Yang, L., Loubière, K., Dietrich, N., Gourdon, C., Hébrard, G. An innovative colorimetric technique for visualizing and characterizing gas-liquid mass transfer around Taylor bubbles in milli-/microchannels. Oral presentation. Rencontres Scientifiques IFPEN "Microfluidics: from laboratory tools to process development". November, 2015. Paris, France.
2. Dietrich, N., Yang, L., Loubière, K., Gourdon, C., Hébrard, G. Visualization of gas-liquid mass transfer around a Taylor bubble during the forming-stage and the flowing-Stage in Microreactors. 12th International Conference on Gas-Liquid & Gas-Liquid-Solid Reactor Engineering (GLS12). Poster Presentation. June, 2015, New York, USA.
3. Loubière, K., Yang, L., Dietrich, N., Loubière, K., Gourdon, C., Hébrard, G. Use of a colorimetric technique based on an oxygen-sensitive dye to measure gas-liquid mass transfer around bubbles flowing in millimetric channels. Oral presentation. FERMaT-SPP1740

Symposium on Non-Invasive Measuring Tools and Numerical Methods for the Investigation of Non-Reactive and Reactive Gas-Liquid Flows, 6-8 June 2016, Toulouse, France.

4. Yang, L., Loubière, K., Dietrich, N., Claude, L.M., Gourdon, C., Hébrard, G. New insights on the gas-liquid mass transfer around Taylor bubbles flowing in a meandering millimetric square channel. 13th International Conference on Gas-Liquid & Gas-Liquid-Solid Reactor Engineering (GLS13). August, 2017, Brussels, Belgium.

Content

Abstract ..... **I**

Résumé ..... **III**

List of Publications ..... **V**

Content ..... **VII**

List of figures ..... **XIII**

List of tables ..... **XXI**

Nomenclature ..... **XXIII**

Chapter 1 Introduction **1**

1.1 Context for the presented work **5**

1.2 Brief state-of-art **7**

1.2.1 Gas-liquid hydrodynamics 7

1.2.1.1 Flow regimes *7*

1.2.1.2 Taylor flow *8*

1.2.2 Gas-liquid mass transfer 13

1.3 General principle of the colorimetric method **17**

1.4 Research aim and thesis outline **19**

Chapter 2 Enhancement factor of the oxygen-sensitive colorimetric reaction 23

Introduction **26**

2.1 Background **26**

2.1.1 Theoretical considerations on Hatta number and enhancement factor 27

2.1.2 Conditions required to determine the characteristic time of gas-liquid reactions 30
2.1.3 Brief state- of- art about the optical methods for measuring diffusion coefficients 31

2.2 Material and methods 32

2.2.1 Fluid properties 32
2.2.2 Experimental set-up for measuring the reaction characteristic time 33
2.2.3 Experimental set-up for the measuring the diffusion coefficient of dihydroresorufin D_B 34
2.2.4 Experimental set-up for measuring the diffusion coefficient of oxygen D_{O_2} 36
2.2.5 Image acquisition and post-treatment 37

2.3 Modeling methods 39

2.3.1 Markov Chain Monte Carlo (MCMC) method 40
2.3.2 Finite difference element scheme 42

2.4 Results and discussion 43

2.4.1 Characteristic time of the reaction 43
2.4.2 Diffusion coefficient of dihydroresorufin D_B in deionized water 45
2.4.3 Diffusion coefficient of oxygen D_{O_2} in the dye solution 47
2.4.4 Hatta number Ha and enhancement factor E 52

2.5 Extended study 54

2.6 Conclusion 58

Chapter 3 Gas-liquid mass transfer around a Taylor bubble right after the formation stage in microreactors 61

Introduction 64

3.1 Materials and methods 65

3.1.1 Compositions of the dye solution 65
3.1.2 Description of the experimental set-up 65
3.1.3 Characterization of gas-liquid hydrodynamics and mass transfer 66

3.2 Results and discussion 70

3.3 Extended study 75

3.4 Conclusion 77

Chapter 4 Gas-liquid mass transfer around Taylor bubbles flowing in a meandering millimetric square channel 79

Introduction 82

4.1 Materials and methods 84

4.1.1 Compositions of the dye solution 84

4.1.2 Fluid properties 84

4.1.3 Description of the experimental set-up 85

4.1.4 Image acquisition system 86

4.1.5 Image processing 87

4.1.5.1 Hydrodynamics of the gas-liquid flow 87

4.1.5.2 Gas-liquid mass transfer 89

4.2 Results and discussion 90

4.2.1 Gas-liquid hydrodynamics 90

4.2.1.1 Flow regimes, overall gas hold-up and bubble velocity 90

4.2.1.2 Bubble length and slug length 94

4.2.1.3 Bubble shape 97

4.2.1.4 Interfacial area 98

4.2.2 Gas-liquid mass transfer 100

4.2.2.1 Equivalent O_2 concentration fields 100

4.2.2.2 Overall gas-liquid mass transfer coefficient 105

4.3 Conclusion 109

Chapter 5 Does a meandering geometry of millimetric channels enable to intensify the performances of gas-liquid mass transfer, when compared to a straight one? 111

Introduction 114

5.1 Materials and methods 114

5.1.1 Fluid properties 114
5.1.2 Description of the experimental set-up 115
5.1.3 Image acquisition system 115
5.1.4 Image processing 116

5.2 Gas-liquid hydrodynamics 117

5.2.1 Flow regimes, overall gas hold-up and bubble velocity 117
5.2.2 Bubble length and slug length 121
5.2.3 Bubble shape 124
5.2.4 Interfacial area 125

5.3 Gas-liquid mass transfer 126

5.3.1 Equivalent O_2 concentration fields 126
5.3.2 Mass transfer coefficients 130

5.4 Comparison of mass transfer performances of straight and meandering channels 132

5.4.1 Mass transfer efficiency 132
5.4.2 Scaling laws 136

5.5 Conclusion 142

Chapter 6 Conclusion and outlook 145

6.1 General conclusion of the thesis 145

6.1.1 Hatta number and enhancement factor of the colorimetric reaction 146
6.1.2 Contribution of the bubble formation stage to the overall mass transfer in microreactors 147
6.1.3 Effect of the meandering geometry on the gas-liquid mass transfer mechanism 147
6.1.4 Benefits of the meandering geometry with respect to straight one on the performance of gas-liquid mass transfer 148

6.2 Outlook 149

References 153

Appendices **165**

Appendix A 165

Appendix B 169

List of figures

Fig. 1-1 Examles of Heat-EXchanger Reactors (HEX). 6

Fig. 1-2 Example of a flow regime map for gas-liquid flow in microchannels. Adapted from Triplett et al. (1999) 8

Fig. 1-3 Schematic representation of unit cell, bubble, liquid slug and film in Taylor flow regime. 10

Fig. 1-4 Recirculation flow patterns in a liquid slug of gas-liquid Taylor flow measured by µ-PIV. Adapted from (Völkel, 2009) 12

Fig. 1-5 Recirculation in the liquid slug between two Taylor bubbles in a microchannel bend. Inset: transverse flow patterns in single-phase flow induced by the channel bend. Adapted from Sobieszuk et al. (2012). 13

Fig. 1-6 Mass transfer processes in Taylor flow. Adapted from Sobieszuk et al. (2012). 14

Fig. 1-7 Reaction scheme for the reversible oxidation-reduction colorimetric reactions between resorufin and dihydroresorufin. The oxidation reaction (B→C) is quasi-instantaneous, and the reduction reaction (C→ B) is slow (few minutes). 18

Fig. 2-1 (a) Schematic diagram of micromixer experiment. Pump I: neMESYS high pressure syringe pump for deionized water saturated with O_2; pump II: neMESYS high pressure syringe pump for dye solution (nitrogen flushed). (b) Picture (I); inner structure (II); illustration of the mixing channel (45×200µm) (III) of SIMM-V2 micromixer. 34

Fig. 2-2 (a) Experimental set-up for the measurement of diffusion coefficients: general overview. Schematic diagram at the connector for measuring D_B (b) and D_{O_2} (c)..... 36

Fig. 2-3 Experiments related to the measurement of the diffusion coefficient of dihydroresorufin D_B. (a) Typical image representing the evolution of color intensity distribution inside the tube. (b) Normalized radial profile of grey values (proportional to the normalized concentration of resorufin) for various axial positions *z*. (Q_R'=3 mL·h^{-1}, Q_W'=3 mL·h^{-1}; *Re'* = 3.82). The experimental data in the red rectangular are the ones that will be used afterwards for the comparison with the theoretical profiles. 39

Fig. 2-4 Variation of the average grey value $\overline{GV}$ at the outlet of the micromixer as a function of the residence time in the micromixer t_r. The bars represent the experimental deviations associated to $\overline{GV}$. 44

Fig. 2-5 Determination of the diffusion coefficient of dihydroresorufin: comparison of the experimental radial profiles of normalized grey values with the predicted ones at an axial location z = 2.6 mm, and for Q_R' = 3 mL·h^{-1}, Q_W' = 6 mL·h^{-1}. The associated predicted diffusion coefficient is equal to D_B = 2.25×10^{-9} m²·s^{-1}. 46

Fig. 2-6 Determination of the diffusion coefficient of dihydroresorufin: variation of the predicted D_B as a function of the axial position z. 47

Fig. 2-7 Determination of the diffusion coefficient of oxygen: (a) Typical experimental image representing the diffusion of O_2 in the dye solution; (b) Comparison between the experimental radial profile of the normalized grey values $GV^{*'}$ with the predicted one at an axial location z = 2.30 mm and for Q_R'' = 9 mL·h^{-1}, Q_W'' = 9 mL·h^{-1}. The associated predicted value of diffusion coefficient is D_{O_2} = 5×10^{-7} m^2·s^{-1}..... 48

Fig. 2-8 Determination of the diffusion coefficient of oxygen: comparison between the experimental radial profiles of the normalized grey values with the predicted ones at an axial location z = 4.59 mm for different values of D_{O_2} (Q_R'' = 9 mL·h^{-1}, Q_W'' = 9 mL·h^{-1})..... 49

Fig. 2-9 Determination of the diffusion coefficient of oxygen: comparison between the experimental radial profiles of the normalized grey values with the predicted ones for a predicted value of D_{O_2} equal to 3.2×10^{-9} m^2·s^{-1} and for different axial positions z. (a) z = 3.06 mm. (b) z = 3.82 mm. (c) z = 4.59 mm. (Q_R'' = 9 mL·h^{-1}, Q_W'' = 9 mL·h^{-1}). 51

Fig. 2-10 Variation of the diffusion coefficient of oxygen D_{O_2} as a function of axial position z for different operating conditions. 52

Fig. 2-11 Variation of the average grey value $\overline{GV}$ at the outlet of the micromixer as a function of the residence time in the micromixer t_r under the concentration of resazurin equal to 1.28×10^{-4} mol·L^{-1}. The bars represent the experimental deviations associated to $\overline{GV}$. 55

Fig. 3-1 (a) Geometry of the microchannel (Cross section: $A = l^2$, where l = 500µm)..... 66

Fig. 3-2 (a) Calibration curve between grey levels and equivalent quantities of oxygen transferred per unit of liquid volume. (b) Illustration of the bubble right after pinch-off. $\overline{C}$: average equivalent oxygen concentration in the liquid slug of the unit cell at this location (the blue rectangle); *X*: axial position of the bubble, *X*=0: the two phases enter in contact. (c) Illustration of the complete unit cell bubble flowing within a distance equal to 14 times the channel width from the junction. $\overline{C'}$: average equivalent oxygen concentration in the liquid slug of the unit cell at this location (the green rectangle). The bubbles in the red rectangle represent the bubble observed. (d) Magnification observation of the mass transfer in the liquid slug. 68

Fig. 3-3 Typical images of the mass transfer process (j_G= 0.053 m·s^{-1}, j_L= 0.27 m·s^{-1}). (a) just after the moment where both gas and liquid phases are injected in the microchannel (transient period). (b) when steady state is reached. The bubble in the red rectangle represents the bubble observed..... 70

Fig. 3-4 Liquid side mass transfer coefficient k_L versus the two-phase superficial velocity ($j = j_G + j_L$) at different gas superficial velocities. 72

Fig. 3-5 Variation of the mass transfer amount fraction Φ as a function of the gas superficial velocity at different liquid superficial velocities. 73

Fig. 3-6 Evolution of the mass of oxygen m_{O_2} in a unit cell as a function of time *t* (*t*=0 ms: the time of the pinch-off stage)..... 76

Fig. 3-7 Evolution of the critical time t_{ct} versus the ratio between the gas-liquid flow rates j_G/j_L. 77

Fig. 4-1 (a) Schematic diagram of the experimental set-up. (b) Picture of the meandering channel in the horizontal *xy*-plan defined in (a). *X* corresponds to the location (curvilinear coordinate) in the channel from the gas inlet. *X* = 0 is the location where the two phases enter in contact. The channel has a cross-sectional area *A* = 2×2 mm^2, and a total developed straight length *L* of 1.37 m. Black circles represent the axial positions where the equivalent oxygen concentration fields were measured. The sections of the channel corresponding to the so-called "turning points" are outlined by blue rectangles. The arrows indicate the flow direction. (c) Schematic of elementary units (bends) of the meandering channel. 86

Fig. 4-2 Sequence of image processing. (a) Typical raw image of gas-liquid flows. (b) Raw image of the channel filled with liquid phase. (c) Detection of the bubbles (binary image). (d) Detection of the liquid slugs (binary image). Operating condition: j_L = 0.139 m·s^{-1}, j_G = 0.069 m·s^{-1}. 88

Fig. 4-3 Gas-liquid mass transfer experiments: (a) Typical raw image, where $\overline{C}$ corresponds to the averaged equivalent oxygen concentration in the liquid slug, and at this axial location in the meandering channel, $\overline{C}$ measured refers to the black rectangle. (b) Calibration curve between grey levels and equivalent amounts of oxygen transferred per unit of liquid volume. (c) Equivalent oxygen concentration field, $C(x, y)$, obtained after applying image processing and the calibration curve. Operating condition: j_L = 0.139 m·s^{-1}, j_G = 0.069 m·s^{-1}, flowing distance X = 0.02 m (close to the gas injection). 90

Fig. 4-4 Cartography of gas-liquid flow regimes. The flow regimes in the frame with solid lines correspond to the Taylor regime, with dashed lines the slug-annular regime, and with dash dotted lines the annular regime. The numbers in the brackets correspond to (*Ca, We, Ce*)..... 92

Fig. 4-5 (a) Evolution of gas hold-up as a function of the volumetric quality of gas in the meandering channel. (b) Bubble velocity versus two-phase superficial velocity. The solid line represents $U_B = j_G + j_L$, the dashed line $U_B = 1.1(j_G + j_L)$, the dash dotted line $U_B = 1.45(j_G + j_L)$..... 94

Fig. 4-6 (a) Normalized bubble length and (b) normalized slug length versus gas liquid flow rate ratio for varying liquid phase velocities in Taylor flow regime in the meandering channel..... 96

Fig. 4-7 Evolution of the interfacial area a as a function of gas fraction β..... 100

Fig. 4-8 Temporal evolution of the equivalent oxygen concentration fields in a liquid slug, from the moment right after the bubble pinch-off to the following times where the observed bubble moves in the meandering channel (operating condition: j_L = 0.139 m·s^{-1}, j_G = 0.069 m·s^{-1}, flow direction from left to right). The bubble in the orange rectangle represents the bubble observed..... 101

Fig. 4-9 Evolution of the amount of transferred oxygen in the liquid slug as a function of time, from the moment right after the bubble pinch-off to the following times where the observed bubble moves in the meandering channel (operating condition: j_L = 0.139 m·s^{-1}, j_G = 0.069 m·s^{-1})..... 103

Fig. 4-10 Evolution of the equivalent oxygen concentration fields in the liquid slug as a function of the axial position in the meandering channel. Operating condition: j_L = 0.139 m·s^{-1}, j_G = 0.069 m·s^{-1}... 104

Fig. 4-11 Comparison of the equivalent oxygen concentration fields in the liquid slug under various operating conditions: (a) j_L = 0.069 m·s^{-1}, j_G = 0.042 m·s^{-1}; (b) j_L = 0.069 m·s^{-1}, j_G = 0.069 m·s^{-1}; (c) j_L = 0.104 m·s^{-1}, j_G = 0.042 m·s^{-1}; (d) j_L = 0.104 m·s^{-1}, j_G = 0.069 m·s^{-1}; (e) j_L = 0.139 m·s^{-1}, j_G = 0.042 m·s^{-1}; (f) j_L = 0.139 m·s^{-1}, j_G = 0.069 m·s^{-1}. Axial position X equals to 0.07 m..... 105

Fig. 4-12 (a) Evolution of mass flux of the transferred oxygen φ_{O_2} per unit of bubble surface as a function of the axial position *X* under various liquid superficial velocities j_L at a given gas superficial velocity j_G=0.042 m·s^{-1}. (b) Comparison of the evolution of normalized average oxygen concentration in the liquid slug along the channel with the ones predicted by the plug flow model. For j_L = 0.069 m·s^{-1}, j_G = 0.014 m·s^{-1}, *Re* = 188; j_L = 0.104 m·s^{-1}, j_G = 0.069 m·s^{-1}, *Re* = 379..... 107

Fig. 5-1 Geometry of the long straight channel. *X* corresponds to the location (curvilinear coordinate) in the channel from the gas inlet. *X*=0: the two phases enter in contact. Cross-sectional area *A*=2×2 mm^2, total developed straight length of channel *L*=1.01 m. Red circles represent the observation positions at different axial positions. 115

Fig. 5-2 Sequence of image processing in the straight channel. (a) Typical raw image of gas-liquid flows. (b) Raw image of the channel filled with liquid phase. (c) Detection of the bubbles (binary image). (d) Detection of the liquid slugs (binary image). Operating condition: j_L = 0.139 m·s^{-1}, j_G = 0.069 m·s^{-1}. 117

Fig. 5-3 Cartography of gas-liquid flow regimes in the straight channel. The flow regimes in the frame with solid lines correspond to the Taylor regime ($L_B / l \le 5$), with dash dotted lines the long slug regime ($L_B / l > 5$), and with dotted lines the slug-annular regime. The numbers in the brackets correspond to (*Ca*, *We*)..... 118

Fig. 5-4 (a) Evolution of gas hold-up as a function of the volumetric quality of gas in the straight channel. (b) Bubble velocity versus two-phase superficial velocity. The solid line represents $U_B = j_G + j_L$..... 120

Fig. 5-5 Normalized bubble length and normalized slug length (blue symbols) versus gas liquid flow rate ratio under various liquid phase velocities in Taylor flow regime in the straight channel..... 122

Fig. 5-6 Evolution of the interfacial area *a* as a function of gas fraction β in the straight channel..... 126

Fig. 5-7 Comparison of the equivalent oxygen concentration fields in the liquid slug under various operating conditions at *X* = 0.07 m: a) I. j_L = 0.069 m·s^{-1}, j_G = 0.042 m·s^{-1}; II. j_L = 0.069 m·s^{-1}, j_G = 0.069 m·s^{-1}; b) I. j_L = 0.139 m·s^{-1}, j_G = 0.042 m·s^{-1}; II. j_L = 0.139 m·s^{-1}, j_G = 0.069 m·s^{-1}; c) I. j_L = 0.208 m·s^{-1}, j_G = 0.042 m·s^{-1}; II. j_L = 0.208 m·s^{-1}, j_G = 0.069 m·s^{-1}..... 127

Fig. 5-8 Evolution of the equivalent oxygen concentration fields in the liquid slug as a function of the axial position in the straight channel. Operating condition: j_L = 0.069 m·s^{-1}, j_G = 0.028 m·s^{-1}..... 128

Fig. 5-9 Temporal evolution of the equivalent oxygen concentration fields in one liquid slug. Operating condition: j_L = 0.069 m·s^{-1}, j_G = 0.028 m·s^{-1}. t = 0 ms represents the moment when the entire bubble appears in the observed window. The bubble in the blue rectangle represents the bubble observed.129

Fig. 5-10 Comparison of the equivalent oxygen concentration fields in the liquid slug under various operating conditions in the bend region: a) I. j_L = 0.069 m·s^{-1}, j_G = 0.042 m·s^{-1}; II. j_L = 0.069 m·s^{-1}, j_G = 0.069 m·s^{-1}; b) I. j_L = 0.139 m·s^{-1}, j_G = 0.042 m·s^{-1}; II. j_L = 0.139 m·s^{-1}, j_G = 0.069 m·s^{-1}; c) I. j_L = 0.208 m·s^{-1}, j_G = 0.042 m·s^{-1}; II. j_L = 0.208 m·s^{-1}, j_G = 0.069 m·s^{-1}. 130

Fig. 5-11 Comparison of the evolution of normalized averaged oxygen concentration in the liquid slug along the channel with the ones predicted by the plug flow model under various liquid superficial velocities j_L at a given gas superficial velocity j_G = 0.042 m·s^{-1}. 131

Fig. 5-12 (a) Number of Transfer Units in the liquid phase versus j_G. Empty and dark symbols correspond to the straight and meandering channels, respectively. (b) Comparisons between liquid absorption efficiencies measured and the ones calculated from Eq. (5-11). 134

Fig. 5-13 Evolution of the mass flux of the transferred oxygen per unit of bubble surface φ_{O_2} as a function of the axial position X under various liquid superficial velocities j_L at a given j_G = 0.042 m·s^{-1}. 137

Fig. 5-14 Evolution of the experimental local dimensionless Sherwood number as a function of the dimensionless Graetz number: (a) in the straight channel; (b) in the meandering channel. Triangle marks represent the operating conditions under a given liquid superficial velocity j_L=0.069 m·s^{-1}; square marks under j_L=0.104 m·s^{-1}; diamond marks under j_L=0.139 m·s^{-1}; circle marks under j_L=0.208 m·s^{-1} 138

Fig. 5-15 Comparison of the experimental local dimensionless Sherwood number with the predicted ones: (a) in straight channel; (b) in meandering channel. Triangle marks represent the operating conditions under a given liquid superficial velocity j_L=0.069 m·s^{-1}; square marks under j_L=0.104 m·s^{-1}; diamond marks under j_L=0.139 m·s^{-1}; circle marks under j_L=0.208 m·s^{-1} 140

Fig. 6-1 Illustration of: (a) helical reactor; (b) spiral-shaped microreactor; (c) different meandering channels, adapted from Dai et al. (2015). 151

Fig. A-1 Image processing: (a) raw image; (b) detection of the bubble contour; (c) corrected image after subtracting the contribution of background and noise, and masking the bubble; (d) equivalent oxygen

concentration field obtained after applying the calibration curve. The experiments were conducted with a concentration of resazurin of 0.1 $g \cdot L^{-1}$. Adapted from Dietrich et al. (2013a) 165

List of tables

Table 1-1 Correlations for prediction the values of $k_L a$ in Taylor flows in the literature. Adapted from Butler et al. (2016). 15

Table 2-1 Physicochemical properties of the liquid phases at 293.15K. 33

Table 2-2 Diffusion peak thickness at normalized concentration of O_2 equal to 0.9, $\delta_{0.9}$: comparison between simulation and experimental values (axial distance z = 4.59 mm). Experimental operating conditions: a. Q_R '' = 9 mL·h^{-1}, Q_W '' = 9 mL·h^{-1}; b. Q_R '' = 4.5 mL·h^{-1}, Q_W '' = 9 mL·h^{-1}; c. Q_R '' = 3 mL·h^{-1}, Q_W '' = 6 mL·h^{-1}. 50

Table 2-3 Concentrations of O_2 and dihydroresorufin at different time. 56

Table 3-1 Comparison of volumetric liquid-side mass transfer coefficient $k_L a$ and liquid-side mass transfer coefficient k_L at two positions, right after the pinch-off and for the complete unit cell flowing at a static location equal to 14 times the channel width from the junction. The superscript " ' " notes the value for the latter situations. 75

Table 4-1 Physio-chemical properties of the liquid phases at 293.15K. 84

Table 4-2 Bubble characteristics versus gas and liquid flow rates in the meandering channel. $k_L a_{Roudet}$ represent the values obtained by Roudet et al. (2011) under the same operating conditions in meandering channel. 97

Table 5-1 Bubble characteristics versus gas and liquid flow rates in the straight channel. $k_L a_{Roudet}$ represent the values obtained by Roudet et al. (2011) under the same operating conditions in straight channel. 124

Table B-1 Data of Sh_X as a function of Gz_X under all operating conditions in straight channel. 169

Table B-2 Data of Sh_X as a function of Gz_X under all operating conditions in meandering channel. 171

Nomenclature

Latin letters

Δt	=	time step, s
a	=	the interfacial area, m^{-1}
A	=	l^2, cross-sectional area of the channel, m^2
A'	=	cross-sectional area of the capillary, m^2
C	=	equivalent oxygen concentration, $kg \cdot m^{-3}$
$\overline{C}$	=	average equivalent oxygen concentration in the liquid slug of the unit cell, $kg \cdot m^{-3}$
C^*	=	dissolved oxygen concentration at saturation, $kg \cdot m^{-3}$
D	=	diffusion coefficient, $m^2 \cdot s^{-1}$
d	=	inner diameter of capillary, m
d_h	=	hydraulic diameter of the channel, m
d_h'	=	hydraulic diameter of the capillary, m
e	=	eccentricity, $e^2=1-l^2/L_B^2$
HTU	=	Height of Transfer Units, m
j	=	superficial velocity, $m \cdot s^{-1}$
k_2	=	second order reaction rate constant, $m^3 \cdot mol^{-1} \cdot s^{-1}$
k_L	=	liquid side mass transfer coefficient, $m \cdot s^{-1}$
k_La	=	volumetric mass transfer coefficient, s^{-1}
l	=	width of the channel, m
L	=	length, m
M	=	Henry's constant
P_0	=	distribution parameter
Q	=	flow rate, $m^3 \cdot s^{-1}$
R	=	reaction rate constant, $m^3 \cdot mol^{-1} \cdot s^{-1}$
r	=	radial distance, m
t	=	time, s
u	=	flow velocity inside the micromixer, $m \cdot s^{-1}$
U	=	velocity, $m \cdot s^{-1}$
u'	=	flow velocity inside the capillary, $m\ s^{-1}$
V	=	volume, m^3
X	=	axial position, m

y = distance from interface in the liquid phase, m
Z = height of gas-liquid contactor, m

Greek letters

v = stoichiometry coefficient (-)
v_L = kinematic viscosity, $m \cdot s^{-2}$
β = volumetric quality of gas (-)
η = reaction extent, %
μ_L = dynamic viscosity of the dye solution, Pa·s
μ_L' = dynamic viscosity of the deionized water, Pa·s
ρ_L = density of the dye solution, $kg \cdot m^{-3}$
ρ_L' = density of the deionized water, $kg \cdot m^{-3}$
σ_L = surface tension of the dye solution, $N \cdot m^{-1}$
σ_L' = surface tension of the deionized water, $N \cdot m^{-1}$
ϕ = mass transfer amount fraction of O_2 during the bubble formation, (-)
ε = gas hold-up, (-)
φ = volumetric mass flux of the transferred O_2 per unit of bubble surface, $kg \cdot m^2 \cdot s^{-1}$

Dimensionless numbers

E = enhancement factor
Ca = Capillary number, $Ca = \mu_L \times U_B / \sigma_L$
Ce = Centrifugal number, $Ce = \rho_L \times U_B^2 \times l^2 / \sigma_L \times r_c$
E_M = Murphree efficiency
Gz = Graetz number, $Gz = l/X \times Re \times Sc$
Ha = Hatta number, $Ha^2 = D_{O2} \times k_2 \times C_{Bb} / k_L^2$
NTU = Number of Transfer Units
p = absorption ratio
Pe = Péclet number, $Pe = Re \times Sc$
Re = Reynold number, $Re = \rho_L \times d_h \times U_B / \mu_L$
Re_B = Reynold number, $Re_B = \rho_L \times U_B \times L_B / \mu_L$
Sh = Sherwood number, $Sh = \varphi_{O2} \times L_B / (D_{O2} \times C_{O2}^*)$
We = Weber number, $We = \rho_L \times U_B^2 \times l / \sigma_L$

Subscripts

0	=	background
B	=	bubble
Bb	=	dihydroresorufin in the bulk
Bf	=	bubble formation
bt	=	before turning point
react_ch	=	characteristic time of the reaction
ct	=	critical time
d	=	drift velocity
G	=	gas phase
i	=	Limit enhancement factor for instantaneous reaction
L	=	liquid phase
m	=	mixing time
max	=	maximum value
min	=	minimum value
R	=	dye solution
r	=	residence time
s	=	liquid slug
UC	=	unit cell
w	=	deionized water

CHAPTER 1

Introduction

Résumé: Ce chapitre introductif est structuré en quatre parties. Le contexte de l'étude (intensification des procédés, réacteurs-échangeurs à plaques) est d'abord présenté (section 1.1). Un court état de l'art (section 1.2) est ensuite dressé dans le but de mettre en avant les éléments clé contrôlant l'hydrodynamique et le transfert de matière gaz-liquide en écoulement de Taylor dans des canaux micro- et millimétriques ; un accent particulier est porté sur l'influence de la géométrie du canal et sur les méthodes d'investigation locale du transfert de matière gaz-liquide. Dans un troisième temps, le principe général de la méthode colorimétrique développée par Dietrich et al., (2013a) est donné (section 1.3). Enfin, les objectifs de la thèse sont définis et le plan de ce manuscrit explicité (section 1.4).

Un résumé de ce chapitre est présenté ci-dessous.

Impulsée par la recherche académique et encouragée par le monde industriel, l'intensification des procédés est née de la nécessité de produire de manière plus propre, plus sûre tout en consommant moins d'énergie. Depuis quelques années, la communauté du génie des procédés contribue à l'émergence de nouveaux équipements (technologies) et/ou méthodes (modes d'activation chimique, nouveaux milieux réactionnels, multifonctionnalité ou hybridation), permettant soit d'optimiser les procédés existants soit de les remplacer par des innovations de rupture.

Parmi les différents types de technologies intensifiées, dont le dénominateur commun est la miniaturisation, les réacteurs-échangeurs à plaques (HEX) jouent un rôle clé. Cependant, la plupart des recherches existantes portant sur ce type d'équipement ont été réalisées dans le cas d'écoulements monophasiques. Pour les réactions gaz-liquide (hydrogénations, photo-oxygénations, fluorations), peu d'études ont été conduites, laissant ainsi de nombreuses questions

fondamentales non résolues, notamment en ce qui concerne la compréhension du couplage entre les phénomènes de transport et la cinétique des réactions.

S'inscrivant dans ce contexte, cette thèse a pour objectif global d'étudier localement le transfert de matière gaz-liquide autour de bulles de Taylor en écoulement dans des canaux millimétriques droits et ondulés. Ceci constitue une étape préliminaire indispensable avant la mise en œuvre de systèmes réactifs diphasiques. Pour cela, une méthode dite colorimétrique a été mise en œuvre. Basée sur l'utilisation d'un colorant sensible à l'oxygène (la résazurine), elle permet de mesurer les champs de concentration équivalente en oxygène dissous autour des bulles, et cela sans aucune excitation laser ou l'insertion d'un capteur physique.

De manière plus spécifique, ces travaux de recherche visent:

- à vérifier la faisabilité d'utilisation de la méthode colorimétrique à micro-échelle;
- à quantifier la contribution de l'étape de formation de bulles dans le transfert de matière global, l'état de l'art faisant défaut sur cette question;
- à étudier localement le transfert de matière gaz-liquide autour de bulles de Taylor en écoulement dans un canal de géométrie ondulé;
- à mieux comprendre comment et pourquoi une telle géométrie de canal permet d'intensifier le transfert de matière gaz-liquide.

A cet effet, ces travaux, et donc le présent mémoire, seront présentés autour de 5 chapitres, en complément de ce chapitre introductif.

Dans le chapitre 2, l'existence d'une possible accélération du transfert de matière gaz-liquide en présence de la réaction chimique utilisée sera étudiée. Pour cela, le temps caractéristique de la réaction sera quantifié grâce à des expériences dans un micro-canal équipé d'un micro-mélangeur. Les coefficients de diffusion du colorant et de l'oxygène seront ensuite déterminés en couplant des techniques optiques originales dans un dispositif microstructuré spécifique de type co-flow, avec une modélisation théorique. La connaissance de ces paramètres permettra in fine de calculer le nombre de Hatta et le facteur d'accélération, et définir des préconisations sur les conditions d'application de la technique colorimétrique pour caractériser le transfert de matière gaz-liquide en milli/micro systèmes (Yang et al., 2017a).

Le chapitre 3 se focalisera sur l'étape de formation des bulles de Taylor dans un microréacteur de type flow-focusing. Les résultats obtenus mettront notamment en évidence que la contribution de l'étape de formation de bulles est prépondérante dans le mécanisme global transfert de matière gaz-liquide (Yang et al., 2016).

Dans le chapitre 4, la technique colorimétrique sera mise en œuvre dans un canal carré millimétrique ondulé. Les paramètres caractéristiques de l'hydrodynamique gaz-liquide seront préalablement caractérisés (taille et vitesse des bulles, rétention de gaz, aire interfaciale). L'évolution des champs de concentration en oxygène dissous dans les bouchons liquides le long du canal ondulé sera ensuite décrite. Un intérêt sera porté sur la manière avec laquelle la structure de l'écoulement (zones de recirculation) à l'intérieur des bouchons liquide est modifiée par la présence des coudes (effet centrifuge). L'influence sur le transfert de matière du large coude liant entre les deux sections rectilignes du canal ondulé sera également mesurée (Yang et al., 2017b).

Le chapitre 5 a pour objectif de rigoureusement comparer des géométries ondulée et droite de canaux. Pour cela, la méthode colorimétrique sera d'abord mise en œuvre dans un canal droit de même diamètre et compacité. Comme pour le canal ondulé, les paramètres hydrodynamiques gaz-liquide seront déterminés ainsi que les coefficients de transfert de matière.

L'ensemble de ces résultats donneront accès à la formulation d'un loi d'échelle unique, reliant le nombre de Sherwood aux nombres de Graetz et de Péclet, et capable de décrire l'évolution du transfert de matière gaz-liquide en fonction de la position axiale dans le canal et des conditions opératoires mises en œuvre.

1.1 Context for the presented work

The past few decades have witnessed the important new developments that go beyond "traditional" chemical engineering and share a common focus on "Process Intensification" (PI). The concept of Process Intensification was firstly defined by Stankiewicz and Moulijn (2000) as: "Any chemical engineering development that leads to a substantially smaller, cleaner, and more energy-efficient technology is process intensification". PI opens up interesting perspectives for the fine chemical and pharmaceutical industries (Stankiewicz and Moulijn, 2000; Tochon et al., 2010; Commenge and Falk, 2014; Gourdon et al., 2015). In particular, the implementation of continuous-flow reactors leads, in a wide range of chemistries, to important improvements with regards to reaction yield and selectivity, safety, competitiveness and eco-impact (Pelleter and Renaud, 2009; Nieves-Remacha et al., 2013; Darvas et al., 2014; Elgue et al., 2015). In this way, various equipment has been developed, benefiting from miniaturization techniques and micro (or milli) fluidics. Most of them consist in devices where chemical reactions have been performed in narrow channels involving a very high surface area to volume ratio and thus providing very efficient rates of mass and heat transfer.

Among all the PI technologies (i.e., spinning disk reactors, static mixer reactors, monolithic reactors), Heat-EXchanger reactors (HEX reactors), combining a milli/micrometric channel reactor and a heat-exchanger in only one unit, are particularly performing in terms of versatility and modularity features, but also of heat and mass transfer capabilities (Anxionnaz et al., 2008; Anxionnaz, 2009; Théron et al., 2014). For illustrative purposes, some examples of HEX reactors are displayed in **Fig. 1-1**.

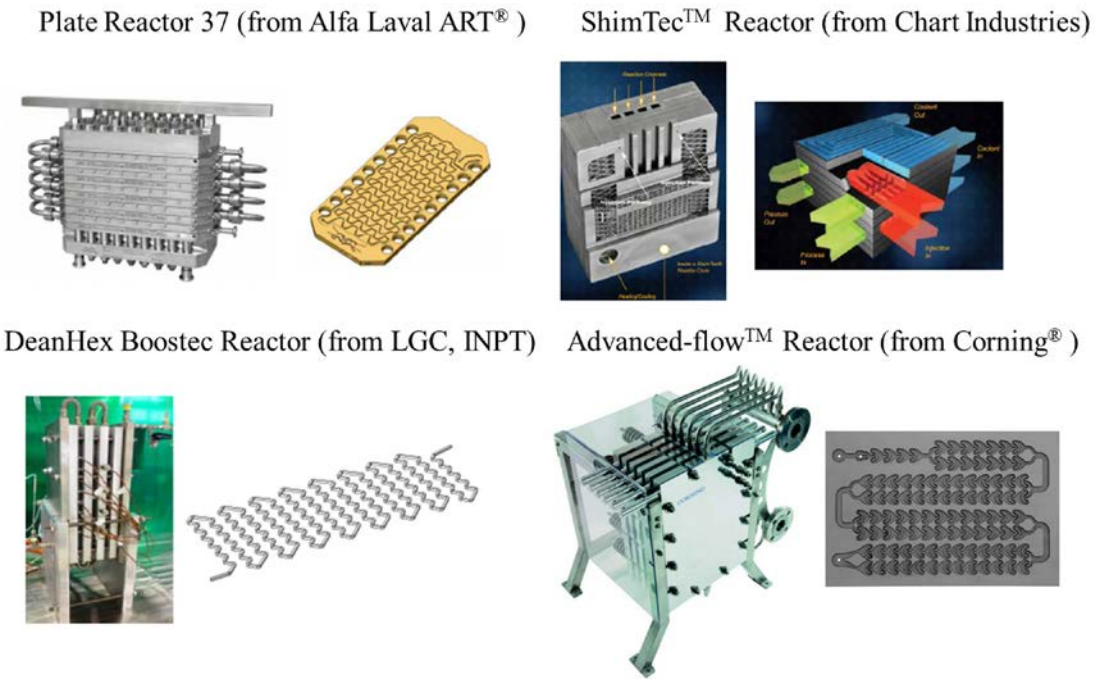

Fig. 1-1 Examples of Heat-EXchanger Reactors (HEX).

They now become standard tools for process development and continuous production, as regrouping many benefits (Anxionnaz et al., 2008; J.E. Hesselgreaves et al., 2016):

- Diminution of waste of energy and raw materials;
- High selectivity and yields due to efficient mixing and enhanced heat and mass transfer;
- Minimized risk of runaway reaction due to enhanced heat transfer, smaller sizes and specific materials;
- Smaller and cheaper plant.

In order to combine both intensified transfers and high residence times in such HEX reactors, the use of meandering (or tortuous or serpentine or wavy) channel structures constitutes a promising way. Based on this background, Anxionnaz (2009) investigated the effect of geometric parameters (channel aspect ratio, bend angle, bend curvature radius, bend straight length) on thermo-hydraulic performances (pressure drop, residence time distribution, mixing, heat transfer coefficient) of a plate HEX reactor involving meandering millimetric channels. In particular, they

converged towards optimal geometries as a function of application constraints in the case of one-phase reactive flows. In fact, most of the existing literature dealing with such type of meandering channels focus on the study of single liquid phase flows, reactive or not (Xiong and Chung, 2007; Anxionnaz-Minvielle et al, 2013; Karale et al., 2013; Dai et al., 2015). Little attention has been surprisingly paid on the implementation of gas-liquid systems in meandering channels, whereas:

(i) the gas-liquid systems occupy a key place in scientific research and industrial application fields (hydrogenations, sensitized photo-oxygenations, fluorinations, biochemical reactions);

(ii) such multiphasic systems still raise many fundamental questions, in particular with respect to the understanding of the coupling between transport phenomena and reaction kinetics;

(iii) studies in straight micro- or millimetric channels are the object of an abundant literature (van Baten and Krishna, 2004; Roudet et al., 2011; Yao et al., 2014; Haghnegahdar et al., 2016; Haase et al., 2016; Butler et al., 2016).

The following section will present a brief overview of the main features of gas-liquid hydrodynamics and mass transfer in milli/micrometric channels. Special attention has been paid to Taylor or slug flows, as this kind of flow enables to achieve the best gas-liquid mass transfer rates required for implementing gas-liquid reactions.

1.2 Brief state-of-art

1.2.1 Gas-liquid hydrodynamics

1.2.1.1 Flow regimes

The gas-liquid flow regime describes the spatial distribution of the two-phase flow in the milli/micro channels, and is of great importance because it controls gas hold-up, interfacial areas, mixing and pressure drop, which remarkably affect mass transfer, and consequently chemical performances. Different types of flow regimes can occur, depending on factors such as the gas and liquid flow rates, the fluid properties (e.g., surface tension, viscosity, density), the wettability of the channel wall by the liquid (i.e., contact angle) or the channel size and geometry (i.e.,

channel cross section and inlet geometry). An extensive review on this topic has been reported by Shao et al. (2009). Five predominant flow regimes are typically identified: bubbly flow, Taylor (or slug) flow, slug-annular flow, annular flow, and churn flow. Stratified flow, commonly observed in macroscale tube, appears rarely in milli/micro channel. For illustrative purposes, **Fig. 1-2** presents the flow regimes identified for air-water flow at different superficial gas and liquid velocities (j_G, j_L) in a 1 mm diameter circular channel (Triplett et al., 1999).

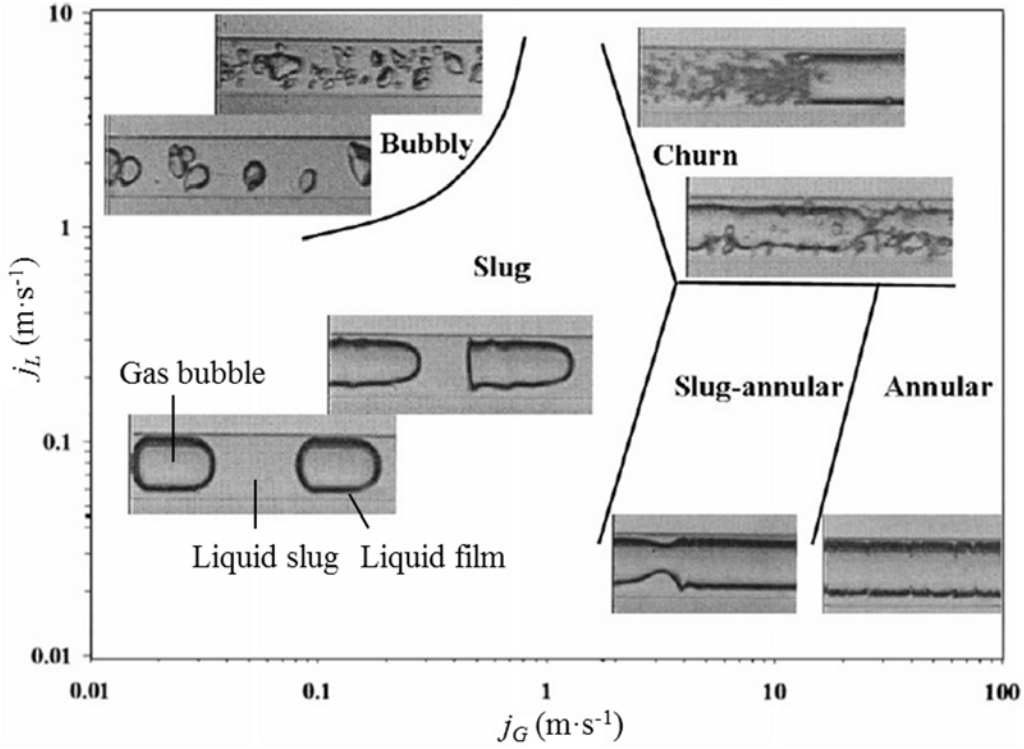

Fig. 1-2 Example of a flow regime map for gas-liquid flow in microchannels. Adapted from Triplett et al. (1999).

1.2.1.2 Taylor flow

Among all the flow regimes, Taylor flows, involving segmented flows of elongated gas bubbles and liquid slugs, is one of the most often-used flow regimes in milli/micro reactors. In fact, they offer many advantages such as being obtainable under a large range of operating conditions, generating regular bubbles and liquid slugs that facilitate the control and the

monitoring of chemical reactions and induce high gas-liquid interfacial areas. In addition, the recirculation loops existing in the liquid slug between consecutive bubbles allow heat and mass transfer enhancement, as well as low axial dispersion, thus making this flow regime highly adapted to applications that are limited by these phenomena (Hessel et al., 2005; Leung et al., 2010). Important parameters influencing the gas-liquid mass transfer are the bubble and liquid slug lengths, as well as the thickness of the liquid film at the wall. A detailed review of the hydrodynamic properties and mass transfer characteristic of Taylor flow has been recently provided by Haase et al. (2016). In the following sub-sections, only some key points will be highlighted.

1.2.1.2.1 Bubble and liquid slug lengths

The length of bubbles and liquid slugs in Taylor flow has a direct impact on the gas-liquid mass transfer since the size of the liquid slug partly controls the rate of liquid recirculation (contact time) and the gas and liquid volume fractions (see **Fig. 1-3**). The dependency of the bubble and slug lengths on the operating conditions in milli/micro channels have been investigated experimentally and numerically (for example in Roudet et al., 2011; Yao et al., 2015; Dong et al., 2015), and various (semi-)empirical correlations, often based on dimensionless numbers (i.e., Reynolds number *Re*, Capillary number *Ca*, Weber number *We*), have been proposed. However, a discrepancy between these correlations is observed; unified relationships remain difficult to establish. This can be mostly attributed to the fact that different inlet geometries, with/without premixing, were employed by the authors; even if they have a strong impact on the gas-liquid flow generated, this contribution is not fully taken into account in the scaling laws currently proposed. Herein, there is still an obvious need to better understand the bubble formation mechanism and the role of inlet geometry on the bubble and liquid slug lengths, and most of all on the overall gas-liquid mass transfer.

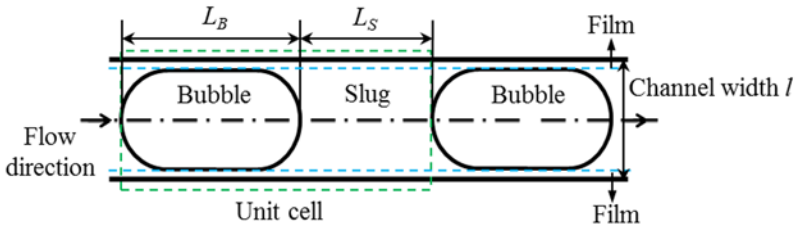

Fig. 1-3 Schematic representation of unit cell, bubble, liquid slug and film in Taylor flow regime.

In HEX reactors, various types of injection geometries are encountered: T-junctions are the most used (mainly for technical reasons) even if co-flow configurations are more efficient for dispersing two phases. In the case of T-junctions, the model proposed by Garstecki et al. (2006) is now commonly admitted to be the most relevant to describe the Taylor bubble formation when Ca<0.02. It is based on a squeezing mechanism in which the interfacial forces dominate the shearing forces. Then bubble generation is controlled by the pressure drop across the forming bubble and is composed of three stages: (a) filling of the gas bubble until it reaches the channel walls; (b) squeezing of the still expanding bubble; (c) the pinch-off of the bubble. Based on the characteristic times for the filling and squeezing stages, a simple model was proposed to predict the bubble length, as follows:

$$\frac{L_B}{l} = 1 + \alpha \cdot \frac{j_G}{j_L} \qquad \text{(Eq.1-1)}$$

where the value of α depends on the geometry of the T-junction. Note that this scaling law is independent of the fluid properties (i.e., viscosities, interfacial tension).

1.2.1.2.2 Bubble velocity

The superficial phase velocities (noted j_G and j_L for gas and liquid phase, respectively) are defined as the ratio between the phase flow rate and the cross-sectional area of the channel. The sum of both velocities is referred to superficial two-phase velocity and noted j. Due to the occurrence of a slipping phenomenon, bubbles are expected to travel slightly faster than predicted by the superficial two-phase velocity. The model of Zuber and Findlay (1965), also named the drift-flux model, is commonly used to correlate the bubble velocity U_B and j, as below:

$$U_B = P_0 \cdot j + U_d \quad \text{(Eq.1-2)}$$

where P_0 represents the distribution parameter, which takes into account the effect of non-uniform flow and concentration profiles; U_d the drift velocity, which considers the effect of the local relative velocity. Tsoligkas et al. (2007) reported that P_0 ranges from 0.85 to 1.38.

1.2.1.2.3 Liquid mixing

The enhanced heat and mass transfer in Taylor flows originate mainly from recirculation motions inside the liquid slug created by the velocity difference between bubble and liquid. In the frame of reference of bubble, this is described by stagnation points at the bubble nose and tail, which cause flow reversal and the creation of a recirculation motion along the length of the liquid slug, as illustrated in **Fig. 1-4**. This behavior was first postulated by Taylor (1961) and later confirmed experimentally, using particle image velocimetry (PIV) (Thulasidas et al., 1997; Günther et al., 2005; Waelchli and Rudolf von Rohr, 2006; Dietrich et al., 2008; Dietrich et al., 2013b), as well as numerically (Kreutzer et al., 2005; Fries and von Rohr, 2009; Abadie et al., 2013).

In the straight channel, the recirculation loops are symmetrical with respect to the channel centerline, and the radial position of the loop center varies as a function of the Capillary number *Ca*, which compares viscosity effects with interfacial effects. As *Ca* increases, the center of recirculation loops moves towards the channel centerline, thereby reducing the effective volume of the recirculating liquid until the recirculation motion vanishes and a full bypass flow occurs (Kolb and Cerro, 1991; Thulasidas et al., 1997; Taha and Cui, 2004). The rate of recirculation in the liquid slug has also shown to be highly dependent on the liquid slug length and the two-phase superficial velocities (Thulasidas et al., 1997; Zaloha et al., 2012). These researchers have demonstrated that the recirculation rate increases with decreasing slug length and increasing two-phase velocities. These results suggest that short and fast-moving liquid slugs have to be favored to intensify the transport processes. Abadie et al. (2013) investigated, using 3-dimensional VOF simulations, the effects of operating parameters (*Ca* and *Re*) and the aspect ratio of the microchannel on the recirculation characteristics of the liquid slug in gas-liquid Taylor flow.

They showed that increasing *Ca* from 0.04 to 0.5 led to a decrease in the recirculation volume in the slug and an increase in recirculation time and that increasing the aspect ratio of the channel from 1 to 4 led to a slight decrease in recirculating volumes but also a significant increase in recirculation times.

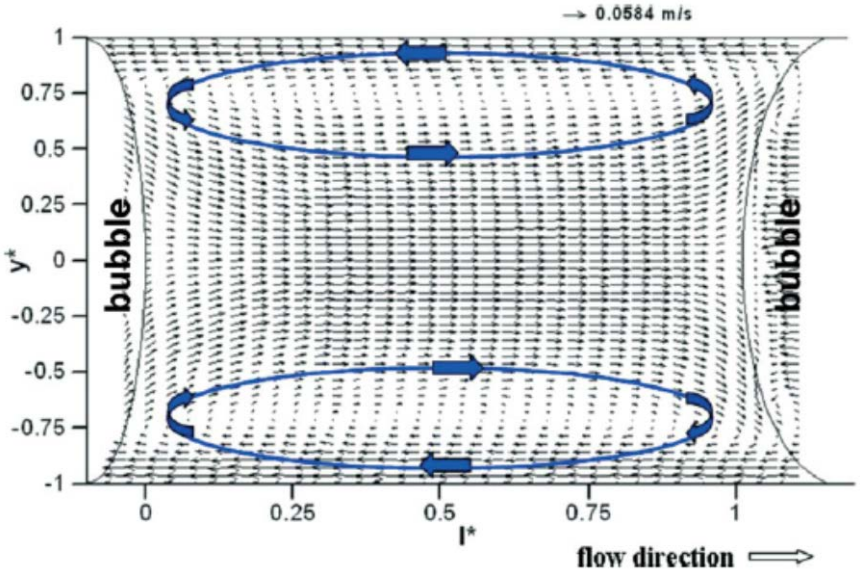

Fig. 1-4 Recirculation flow patterns in a liquid slug of gas-liquid Taylor flow measured by µ-PIV. Adapted from (Völkel, 2009).

When the gas-liquid Taylor flow passes through some bends, the hydrodynamics in the liquid slug is significantly modified when compared to a straight geometry (Günther et al., 2004; Fries et al., 2008; Fries and von Rohr, 2009). **Fig. 1-5** illustrates this point by showing how the recirculating flow is no longer symmetrical about the channel centerline and the loops vary in size. This is due to the fact that transverse flows (normal to the streamwise direction) are generated in the bend due to centrifugal forces (W.R. Dean, 1928). The combination of this traverse flow with the recirculation loops produces a highly complex flow, which enables to intensify significantly the mixing efficiency in the liquid slug (Günther et al., 2004) and provides narrow residence time distributions (Trachsel et al., 2005). Fries et al. (2008) and Fries and von Rohr (2009) have also reported that the asymmetry of the recirculation loops and the strength of recirculation depend on the microchannel geometry (dimensions, aspect ratio, radius of curvature)

and on the two-phase superficial velocity. Although these studies have pointed out the development of complex flow behavior inside the liquid slugs in the milli/micro channel bends, a complete description and analysis of the flow in 3D is still required.

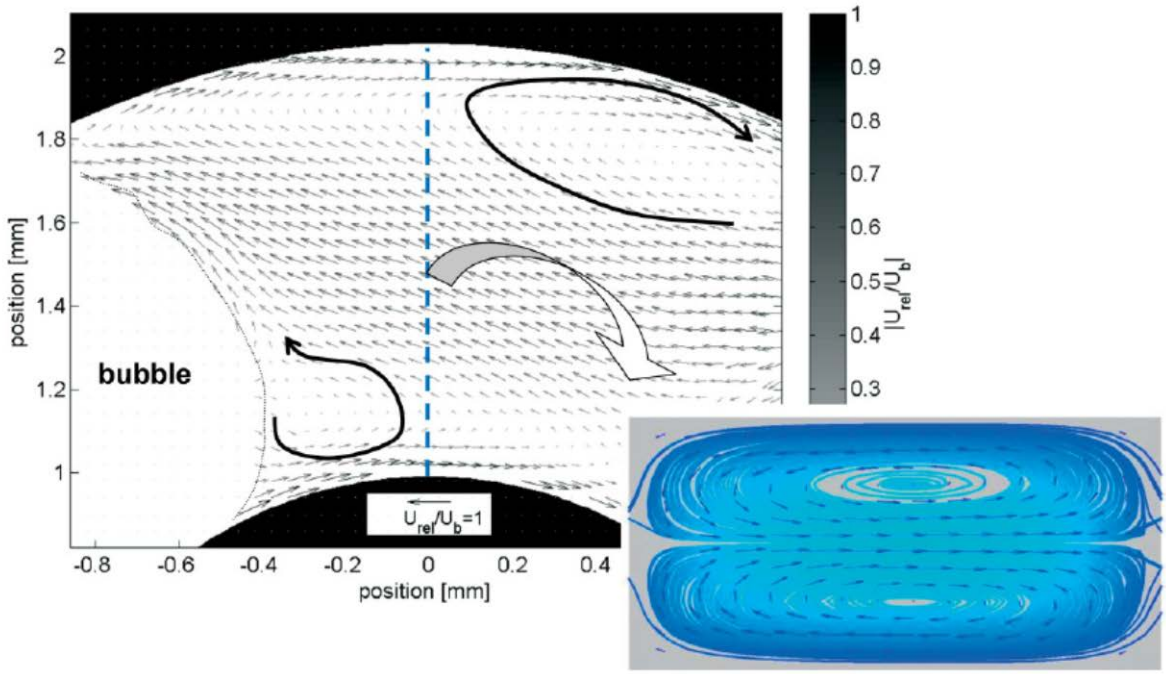

Fig. 1-5 Recirculation in the liquid slug between two Taylor bubbles in a microchannel bend. Inset: transverse flow patterns in single-phase flow induced by the channel bend. Adapted from Sobieszuk et al. (2012).

1.2.2 Gas-liquid mass transfer

In Taylor flow, several mechanisms of mass transfer can be distinguished, as illustrated in **Fig. 1-6**: (1) bubble to the channel wall through the liquid film; (1a) bubble to film; (1b) film to wall; (2) bubble to the liquid slug; (3) slug to wall; (3a) slug to film; (3b) film to wall. If the channel wall takes part in the mass transfer process (the channel wall is active, i.e. coated with a catalyst), then all the above-mentioned contributions may occur simultaneously (Haase and Bauer, 2011). On the other hand, if the channel wall is a passive, only steps (1a) and (2) will occur (Tan et al., 2012a).

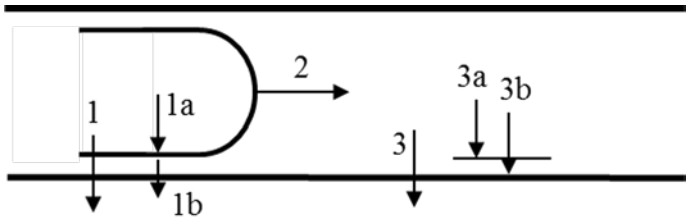

Fig. 1-6 Mass transfer processes in Taylor flow. Adapted from Sobieszuk et al. (2012).

For Taylor flow, as the liquid phase consists in a series of mixed slugs, the plug-flow model was often used when modeling liquid mass transfer. Uniform velocity and concentration over the channel cross section was then considered at a given axial location, without taking into account the real structure of the flow in the liquid slug, in particular the recirculation loops (Berčič and Pintar, 1997; Shao et al., 2010). In this case, it is assumed that both phases flowing through the channel exchange mass between the same compartments (for example, between same gas and liquid slugs in Taylor flow), and therefore, one driving force is required to define the mass transfer rate. For a solute transferring from gas phase (phase 1) to liquid phase (phase 2), and assuming that the resistance lies in the liquid phase, the change of its concentration in liquid phase with respect to the residence time t_r can be expressed as:

$$\frac{dC}{dt_r} = k_L a \cdot (C^* - C) \qquad \text{(Eq.1-3)}$$

where C^* is the equilibrium concentration in liquid phase, $k_L a$ the overall volumetric gas-liquid mass transfer coefficient, a the specific interfacial area.

For $k_L a$ measurement, different experimental methods are encountered in the literature (Yue et al., 2009; Yao et al., 2014; Haghnegahdar et al., 2016). These methods are based on the offline or online measures of the concentration of solute in the continuous system. The so-called offline measurement techniques are global methods, where the concentration at the exit of the microreactor is determined, after phase separation, by chromatographic or spectrometric analysis (Berčič and Pintar, 1997; Yue et al., 2007; Vandu et al., 2005; Sobieszuk et al., 2012; Wang et al.,

2014), or using probe (Roudet et al., 2011). However, these offline techniques are rather time-consuming and lead to an inaccurate characterization, as the sample collection and phase separation times are not usually taken into account. Therefore, some online methods have been used more intensively in the past years: they are mostly based on (i) the following of the time-dependent variations of the bubble sizes (Tan et al., 2012b; Yao et al., 2014; Pan et al., 2014; Yang et al., 2014), or (ii) the use of fluorescence (Kuhn and Jensen, 2012), where the changes in laser-induced fluorescence (LIF) origin from dissolved carbon dioxide affecting the laser light emission of a pH-sensitive dye. However, the quality of the concentration fields was not well described by this method. Thus, there still exists no direct and convenient online method to access the local mass transfer information.

In the literature, there exist various correlations for $k_L a$ estimation: basing on dimensionless numbers ones or not, they were established by using either the offline methods or the online ones. The major ones (i.e. the most often cited) are listed in **Table 1-1**.

Table 1-1 Correlations for prediction the values of $k_L a$ in Taylor flows in the literature. Adapted from Butler et al. (2016).

Reference	Correlation	Conditions
Berčič and Pintar (1997)	$k_L a = \frac{0.111 \cdot j^{1.19}}{[(1-\beta_G)\cdot(L_B+L_S)]^{0.57}}$	Offline. Circular straight channel: d_h=1.5/2.0/3.1 mm j = 0.092-0.56 m·s^{-1} L_{UC} = 6-99 mm
van Baten and Krishna (2004)	$k_L a = 2\cdot\sqrt{\frac{\pi\cdot(L_B-l)}{L_{UC}\cdot l}}\cdot\sqrt{\frac{D\cdot U_B}{L_B-l}}+2\cdot\sqrt{\frac{2}{L_{UC}}}\cdot\sqrt{\frac{D\cdot U_B}{l}}$	CFD simulations. One unit cell: d_h=1.5/2.0/3.0 mm (circular) U_B = 0.15-0.55 m·s^{-1} L_{UC} = 15-50 mm

Vandu et al. (2005)	$k_L a = 4.5 \cdot \sqrt{\frac{D \cdot U_B}{L_{UC}}} \cdot \frac{1}{d_h}$	Offline. Circular straight channel: d_h=1.0/2.0/3.0 mm U_B = 0.09-0.65 m·s^{-1} L_{UC} = 5-60 mm
Yue et al. (2007a)	$k_L a = \frac{Sh \cdot a \cdot D}{d_h}$ $Sh = \frac{a}{d_h} \cdot (0.084 \cdot Re_G^{0.213} \cdot Re_L^{0.937} \cdot Sc^{0.5})$	Offline. Rectangular straight channel: d_h=0.67 mm (0.5 mm×1.0 mm) U_B = 0.05-0.35 m·s^{-1} L_{UC} = 1.1-1.3 mm
Yue et al. (2009a)	$k_L a = \frac{2}{d_h} \cdot (\frac{D \cdot U_B}{d_h})^{0.5} \cdot (\frac{L_B}{L_B + L_S})^{0.3}$	Offline. Square straight channel: d_h=0.2/0.4 mm U_B = 0.4-2.0 m·s^{-1} L_{UC} = 0.5-3.8 mm
Sobieszuk et al. (2011)	$k_L a = \frac{Sh \cdot a \cdot D}{d_h} = 0.1 \cdot Re_G^{1.12} \cdot Sc^{0.05} \cdot \frac{a \cdot D}{d_h}$	Offline. Circular straight channel: d_h=0.4 mm j = 0.6-1.2 m·s^{-1} a = 6580-9550 m^{-1}
Kuhn and Jensen (2012)	$k_L a = \frac{Sh \cdot a \cdot D}{d_h} = (20.8 + 0.078 \cdot Re_G^{1.779} \cdot Re_L^{-0.112} \cdot Sc^{0.5}) \cdot \frac{a \cdot D}{d_h}$	Online. Square meandering channel: d_h=0.4 mm U_B = 0.08-0.23 m·s^{-1} ε_G = 0.35-0.80
Yao et al. (2014)	$k_L a = \frac{Sh \cdot a \cdot D}{d_h} = (1.367 \cdot Re_G^{0.421} \cdot Re_L^{0.717} \cdot Sc^{0.64} \cdot Ca^{0.5}) \cdot \frac{a \cdot D}{d_h}$	Online. Rectangular meandering channel: d_h=0.4 mm (0.3 mm×0.6 mm) j_G = 0.07-0.55 m·s^{-1} j_L = 0.09-0.19 m·s^{-1}

It can be known from the above table that, among all the existing correlations for predicting $k_L a$, there is no model taking into account the impact on the gas-liquid mass transfer of the channel geometry or of the axial position along the channel.

To conclude, this brief state-of-art highlights that there is a need to propose an online, direct and easy-to-implement method to overcome the limitations of offline methods, to isolate the contribution of the different stages (the bubble formation, the bubble flowing and the phase separation ones) and to access to a local description of the gas-liquid mass transfer. The colorimetric technique proposed by Dietrich et al. (2013) is a promising way to answer these challenges. The following section will describe its principle.

1.3 General principle of the colorimetric method

The so-called colorimetric technique is based on the use of an oxygen-sensitive dye, namely resazurin. Resazurin is a phenoxazin-3-one dye which has been widely employed for testing bacterial or yeast contamination in biological fluids and milk, and also identifying the semen quality by colorimetry since 1950s (Erb and Ehlers, 1950; O'Brien et al., 2000). As shown in **Fig. 1-7**, resazurin (blue and not fluorescent) is reduced into resorufin (pink and highly fluorescent), which is itself reduced to dihydroresorufin (colourless and not fluorescent). Note that the complete chemical molecular formula of resazurin is 7-Hydroxy-3H-phenoxazin-3-one-10-oxide, which the molar mass equals to 229.19 $g \cdot mol^{-1}$, and the solubility in water equals to $1g \cdot L^{-1}$ (Sigma-Aldrich®).

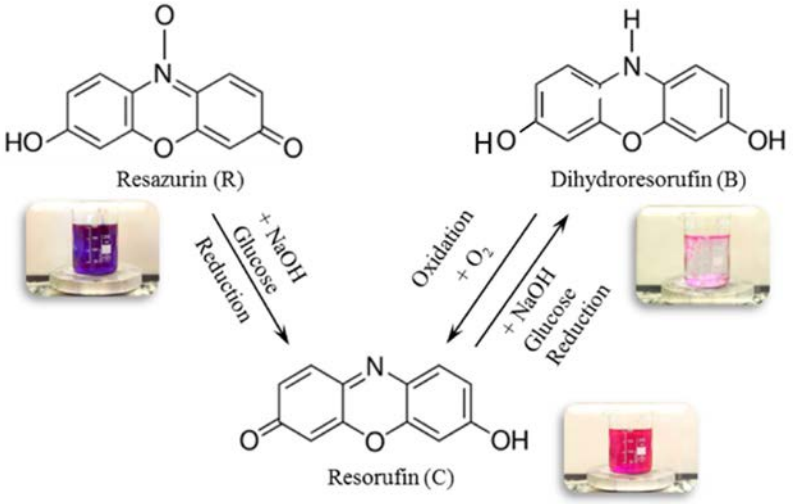

Fig. 1-7 Reaction scheme for the reversible oxidation-reduction colorimetric reactions between resorufin and dihydroresorufin. The oxidation reaction (B→C) is quasi-instantaneous, and the reduction reaction (C→ B) is slow (few minutes).

The colorimetric reaction occurs in presence of glucose and sodium hydroxide. In alkaline solutions, glucose is oxidized to D-gluconic acid or alpha-D-gluconolactone:

$$HOCH_2(CHOH)_4CHO + 3\cdot OH^- \rightarrow HOCH_2(CHOH)_4CO_2 + 2\cdot H_2O + 2\cdot e^- \qquad \text{(Eq.1-4)}$$

(Dextrose) (Gluconic acid)

The change of colour results from the reversible oxidation-reduction reactions between resorufin (pink) and dihydroresorufin (colourless):

$$O_2 + 2\cdot \text{Dihydroresorufin} \rightarrow 2\cdot \text{Resorufin} + 2\cdot H_2O \text{ (Fast reaction)} \qquad \text{(Eq.1-5)}$$

$$\text{Resorufin} + \text{Dextrose} \rightarrow \text{Dihydroresorufin} + \text{Gluconic acid (Slow reaction)} \qquad \text{(Eq.1-6)}$$

In terms of reactional mechanism, it is interesting to observe that these reactions present some similitudes with the so-called Fehling's reaction (Fehling, 1849) used as a test for reducing sugars, in which the resazurin would play the role of the copper (II) ions.

For mass transfer experiments, the composition of the dye solution should be optimized so as to fill the following conditions:

- (quasi)-instantaneous kinetics for the oxidation of dihydroresorufin (colourless) into resorufin (pink), and faster reaction than the gas-liquid mass transfer;
- sufficiently slow kinetics (few minutes) for the reduction of resorufin (pink) into dihydroresorufin (colourless);
- high colorimetric yield, namely the concentration of resazurin needed to be adapted for each operating condition to meet the color intensity requirement.

1.4 Research aim and thesis outline

The present thesis aims at studying gas-liquid mass transfer in straight and meandering millimetric channels constituting HEX reactors. This is a preliminary step essential before implementing gas-liquid reactive systems. Mass transfer between both phases plays then a key role, and, depending on chemical kinetics, can become the limiting step controlling the reaction conversion. In this case, the knowledge of gas-liquid hydrodynamics (i.e. flow regime, mixing, interfacial area), which is affected by the geometry of the millimetric channel (straight or meandering), is crucial for predicting mass transfer properties and in return chemical conversion/selectivity.

For that, the colorimetric method developed by Dietrich et al. (2013) will be implemented with the objectives:

1) To verify the feasibility of the colorimetric technique at microscale;
2) To investigate the contribution of gas-liquid mass transfer during the bubble formation stage to the overall mass transfer, the state-of-art showing a lack of works in this field;
3) To locally investigate gas-liquid mass transfer around Taylor bubbles flowing in a meandering channel;
4) To better understand how and why such geometry of channel enables to intensify gas-liquid mass transfer.

The thesis outline is described per chapter below.

In **Chapter 2,** the occurrence of a possible enhancement of the gas-liquid mass transfer by the chemical reaction involved will be investigated. For that, as data on the associated kinetic are seldom in the literature, the reaction characteristic time and kinetic constant will be firstly estimated by carrying out experiments in a microchannel equipped with a micromixer. The diffusion coefficients of dihydroresorufin and O_2 will be then determined by implementing two original optical methods in a specific co-flow microchannel device, coupled with theoretical modelling. The knowledge of these parameters will enable to calculate the Hatta number and the enhancement factor, and then to give complementary information about the reliability of the colorimetric technique to characterize the gas-liquid mass transfer in milli/micro systems (Yang et al., 2017a).

In **Chapter 3**, a special microscale focus will be made on the study of the gas-liquid mass transfer occurring in Taylor flows right after the bubble formation stage in a flow-focusing microreactor. The objective here will be to quantify the contribution of mass transfer right after the bubble formation stage to the overall gas-liquid mass transfer (Yang et al., 2016).

In **Chapter 4**, the colorimetric technique will be implemented in a meandering millimetric square channel. The gas-liquid hydrodynamics will be beforehand characterized in terms of bubble length and velocity, gas hold-up, interfacial area. The evolution of equivalent oxygen concentration fields in the liquid slugs passing through one and several bends will be then described as well as the influence of the “turning point” joining two “straight” sections of the meandering channel (Yang et al., 2017b).

Chapter 5 aims at rigorously comparing the performances in terms of gas-liquid hydrodynamics and mass transfer between a straight and a meandering channel. The underlying scientific question is to know if the meandering geometry, such as designed, enables or not to intensify the gas-liquid mass transfer. For comparison purpose, the colorimetric method will be first implemented in a straight channel of identical diameter and compactness. As in the meandering channel, the gas-liquid hydrodynamics will be characterized and mass transfer coefficients estimated. At last, a scaling law will be established to describe the evolution of gas-liquid mass transfer as a function of axial position and operating conditions.

An overview of the main results of the thesis will be presented in **Chapter 6**, as well as the outlook of this work.

CHAPTER 2

Enhancement factor of the oxygen-sensitive colorimetric reaction

Résumé: Des travaux antérieurs ont montré que la méthode colorimétrique, basée sur l'utilisation d'un colorant (résazurine) sensible à la présence d'oxygène, est particulièrement adaptée à la visualisation et à la caractérisation locale du transfert de matière gaz-liquide, et cela à différentes échelles (Kherbeche et al., 2013; Dietrich et al., 2013; Yang et al., 2016). Cependant, la non-existence d'une accélération du transfert de matière gaz-liquide en présence de cette réaction chimique n'a pas été démontrée jusqu'à présent. L'objectif de ce chapitre est de combler ce manque, en évaluant le nombre de Hatta (*Ha*) et le facteur d'accélération (*E*) associés à la réaction d'oxydo-réduction de la résazurine.

Pour cela, étant donné que les données cinétiques sur cette réaction sont quasi-inexistantes dans la littérature, le temps caractéristique de la réaction a été quantifié grâce à des expériences dans un micro-canal équipé d'un micro-mélangeur. Les coefficients de diffusion du colorant et de l'oxygène ont été ensuite déterminés en couplant des techniques optiques originales dans un dispositif microstructuré spécifique de type *co-flow*, avec une modélisation théorique. La connaissance de ces paramètres a permis in fine de calculer le nombre de Hatta et le facteur d'accélération, et définir des préconisations sur les conditions d'application de la technique colorimétrique pour caractériser le transfert de matière gaz-liquide en milli/micro systèmes (Yang et al., 2017a).

Ce chapitre a été publié dans l'article suivant : Yang L., Dietrich N., Loubière K., Gourdon C., Hébrard G. (2017a), *Optical methods to investigate the enhancement factor of an oxygen-sensitive colorimetric reaction using microreactors*, ***AIChE Journal.*** 63, 2272–2284. Doi:10.1002/aic.15547.

Il est à noter que certaines parties de la conclusion ont été modifiées. En outre, une nouvelle partie a été introduite à la fin du chapitre : des résultats, non publiés, sont présentés, permettant de déterminer de manière exacte la constante cinétique de la réaction.

Abstract: Previous works have shown that the colorimetric technique, based on the use of an oxygen-sensitive dye is relevant for locally visualizing and characterizing gas-liquid mass transfer at different scales (Kherbeche et al., 2013; Dietrich et al., 2013; Yang et al., 2016). Until now, the occurrence of a possible enhancement of the gas-liquid mass transfer by this reaction has not been demonstrated. This chapter aims at filling this gap by evaluating the Hatta number *Ha* and the enhancement factor *E* associated with the oxygen colorimetric reaction presented in Chapter 1 when implementing in milli/micro channels.

For that, as data on the kinetic of the colorimetric reaction are seldom in the literature, the reaction characteristic time was firstly estimated by carrying out experiments in a microchannel equipped with a micromixer. The diffusion coefficients of dihydroresorufin and O_2 were determined by implementing two original optical methods in a specific co-flow microchannel device, coupled with theoretical modelling. The knowledge of these parameters enabled at last to demonstrate that no enhancement of the gas-liquid mass transfer by this colorimetric reaction existed. Complementary information about the reliability of the colorimetric technique to characterize the gas-liquid mass transfer in milli/micro systems was also given.

This chapter has been published as Yang L., Dietrich N., Loubière K., Gourdon C., Hébrard G. (2017a), *Optical methods to investigate the enhancement factor of an oxygen-sensitive colorimetric reaction using microreactors*, ***AIChE Journal.*** 63, 2272–2284. Note that some parts of the conclusion has been modified.

A new section is also added at the end of the chapter: some results, not yet published, are presented, enabling to determine the exact reaction characteristic time.

Introduction

The objective of the present study is to rigorously determine the enhancement factor *E* associated with the oxygen-sensitive colorimetric reaction when implementing in micro/millichannels. For that, the knowledge of the kinetics of the reaction and of the diffusion coefficients of both oxygen and dihydroresorufin into the liquid under test, is a prerequisite. As these parameters are unknown, original methods will be proposed to determine them: they will be based on specific experiments in microfluidic devices, coupled with modeling approaches. The chapter will be composed of four main sections.

Section 2.1 will remind the knowledge available on the kinetics of the colorimetric reaction and the theoretical background associated with the enhancement factor concept.

Section 2.2 will be mainly devoted to the description of the three experimental set-up designed for measuring on the one hand the characteristic time of the reaction (experiments in a microchannel equipped by a micromixer) and on the other hand, the diffusivity coefficients of dihydroresorufin and O_2 (optical methods in a specific co-flow microchannel device).

Section 2.3 will focus on the modelling methods used to analyze the experimental data so as to access the diffusion coefficients of dihydroresorufin and O_2.

The results will be presented and discussed in section 2.4 and section 2.5: they will concern the characteristic time of the reaction, the diffusion coefficients and the calculation of the Hatta number and the enhancement factor. Such findings will at last enable to determine the enhancement factor *E* associated with the colorimetric reaction, as well as providing the guidelines to evaluate the conditions required to implement the colorimetric method at other scales or in other gas-liquid systems.

2.1 Background

This section will describe firstly the data at present available on the kinetics of the colorimetric reaction and secondly the theoretical background associated to the enhancement factor concept, especially in the case of fast gas-liquid reactions. In a last time, the basic

conditions required to experimentally acquire the characteristic time of gas-liquid reactions will be reminded as well as a brief state-of-art about the various optical methods existing to measure diffusion coefficients.

2.1.1 Theoretical considerations on Hatta number and enhancement factor

In the present study, one focuses on the colorimetric reaction between dihydroresorufin (B) and oxygen (O_2):

$$O_2 + 2\times \text{Dihydroresorufin} \rightarrow 2\times \text{Resorufin} + 2\times H_2O \qquad \text{(Eq. 2-1)}$$

(colorless) (pink)

Based on the literature background (Anderson et al., 2012; Zhang et al., 2014), one can assume that this colorimetric reaction is of a global order of 2, with respect to the oxygen and to the dihydroresorufin. The rate of consumption of dihydroresorufin, R_B (or the rate of consumption of oxygen R_{O_2}) is then expressed as:

$$R_B = -\nu \cdot k_2 \cdot C_{O_2} \cdot C_B = \nu \cdot R_{O_2} \qquad \text{(Eq. 2-2)}$$

where k_2 is the reaction rate constant ($m^3 \cdot mol^{-1} \cdot s^{-1}$) and ν the stoichiometric coefficient equal to 2.

In presence of a chemical reaction, the mass flux of oxygen φ_{O_2} transferred from the gas phase to the liquid phase is expressed, as below:

$$\varphi_{O_2} = k_L \cdot a \cdot E \cdot (C^*_{O_2} - C_{O_2}) \qquad \text{(Eq. 2-3)}$$

where k_L is the liquid-side mass transfer coefficient ($m \cdot s^{-1}$), a the interfacial area (m^{-1}); $C^*_{O_2}$ the dissolved oxygen concentration at saturation ($kg \cdot m^{-3}$), and E the enhancement factor (-). The latter is defined by the ratio between the average fluxes of absorption with reaction and without reaction, thus it represents in a way the effect of “pumping” by the chemical reaction.

To determine E, the mass balances in the liquid film for both oxygen and dihydroresorufin (B) should be written (van Krevelen and Hoftijzer, 1948), using the expression of the second-order reaction kinetics (Eq. 2-2). It leads to:

$$-R_{O_2} = D_{O_2} \cdot \frac{d^2 C_{O_2}}{dy^2} = \frac{dC_{O_2}}{dt} = k_2 \cdot C_{O_2} \cdot C_B \qquad \text{(Eq. 2-4)}$$

$$-R_B = D_B \cdot \frac{d^2 C_B}{dy^2} = \frac{dC_B}{dt} = \nu \cdot k_2 \cdot C_{O_2} \cdot C_B \qquad \text{(Eq. 2-5)}$$

where D_{O_2} and D_B are the diffusion coefficient of O_2 and B respectively ($m^2 \cdot s^{-1}$), C_{O_2} and C_B the concentrations of O_2 and B at a given location y in the film respectively ($mol \cdot m^{-3}$); y the distance from the gas-liquid interface to the bulk liquid phase (m), where none convection and accumulation is assumed to occur.

The associated boundary conditions are:

- at the interface ($y = 0$): $C_{O_2} = C_{O_2}^*$ and $\frac{dC_B}{dy} = 0$ (B: non-volatile) (Eq. 2-6)

- at the limit of the film ($y = \delta$), δ being the film thickness, the concentrations of both O_2 and B are the ones in the liquid bulk, which depend on the hydrodynamics of the reactor and on the transport phenomena through the liquid film. By assuming that the liquid bulk can be considered as perfectly mixed and that the liquid does not contain any dissolved oxygen, the boundary conditions are given by the mass balances in the liquid bulk when considering the chemical reaction and the fluxes transferred from the film by diffusion only towards the liquid bulk:

$$-D_{O_2} \cdot S \cdot \left(\frac{dC_{O_2}}{dy}\right)_{y=\delta} = Q \cdot C_{O_2 b} + V_L \cdot R_{O_2} \qquad \text{(Eq. 2-7)}$$

$$-D_B \cdot S \cdot \left(\frac{dC_B}{dy}\right)_{y=\delta} = Q \cdot (C_{Bb} - C_{Bi}) + V_L \cdot R_B \qquad \text{(Eq. 2-8)}$$

where S is the gas-liquid interfacial area (m^2) , Q the volumetric flow rate of the liquid dye solution ($m^3 \cdot s^{-1}$), V_L the liquid volume (m^3), $C_{O_2 b}$ the concentration of O_2 in the liquid bulk, C_{Bi} and C_{Bb} the concentrations of B at the inlet of the reactor and in the liquid bulk respectively ($mol \cdot m^{-3}$).

By making these equations dimensionless, one can demonstrate that the concentration profiles, the absorption flux of oxygen and thus the enhancement factor depend on the following dimensionless numbers: the Hatta number *Ha*, the parameter *Z*, the Damköhler number *Da* and the parameter *H*, defined as below:

$$Ha^2 = \frac{k_2 \cdot C_{O_2}^* \cdot C_{Bb} \cdot \delta}{D_{O_2} \cdot \frac{C_{O_2}^* - 0}{\delta}} = \frac{k_2 \cdot C_{Bb} \cdot \delta^2}{D_{O_2}} = \frac{k_2 \cdot C_{Bb} \cdot D_{O_2}}{k_L^{\ 2}} \qquad \text{(Eq. 2-9)}$$

$$Z = \frac{D_B \cdot C_{Bb}}{\nu \cdot D_{O_2} \cdot C_{O_2}^*} \qquad \text{(Eq. 2-10)}$$

$$Da = k_L \cdot a \cdot \tau = k_L \cdot a \cdot \frac{V_R}{Q} \qquad \text{(Eq. 2-11)}$$

$$H = \frac{k_2 \cdot C_{O_2}^* \cdot C_{Bb} \cdot \varepsilon_L}{k_L \cdot a \cdot C_{O_2}^*} = \frac{k_2 \cdot C_{Bb} \cdot \varepsilon_L}{k_L \cdot a} \qquad \text{(Eq. 2-12)}$$

The Hatta number Ha represents the ratio between the maximal rate of reaction in the liquid film and the mass flux crossing the film by diffusion; the parameter *Z* contains the ratio between the diffusion coefficients; the Damköhler number *Da* (also called the Number of Transfer Units) represents the ratio between the residence time and the characteristic time of gas-liquid mass transfer; *H* compares the maximum reaction rate of O_2 that can be achieved within the liquid with the maximum O_2 physical absorption rate, and ε_L the liquid hold-up.

In the case of a fast reaction regime in the diffusional film, for which Ha is higher than 3, Van Krevelen and Hoftijzer (van Krevelen and Hoftijzer, 1948) have shown that the

enhancement factor becomes only a function of *Ha* and of the enhancement factor for instantaneous regime (also called the limit enhancement factor), noted E_i and defined as:

$$E_i = 1 + Z = 1 + \frac{D_B \cdot C_{Bb}}{\nu \cdot D_{O_2} \cdot C^*_{O_2}} \qquad \text{(Eq. 2-13)}$$

In this case, these authors proposed the following approximated solution for the enhancement factor E:

$$E = \frac{Ha \cdot \sqrt{\frac{E_i - E}{E_i - 1}}}{\tanh(Ha \cdot \sqrt{\frac{E_i - E}{E_i - 1}})} \qquad \text{(Eq. 2-14)}$$

The latter developments reveal that the calculation of the enhancement factor requires the knowledge of the kinetics constant k_2, and of both diffusion coefficients, D_{O_2} and D_B. As these parameters are unknown in the present case, the following two subsections will present some theoretical considerations that need to be taken into account for determining a reaction characteristic time and a brief state-of-art about the methods for measuring diffusion coefficients respectively.

2.1.2 Conditions required to determine the characteristic time of gas-liquid reactions

When carrying out a gas-liquid reaction, two distinct phenomena simultaneously exist in a given experimental device: the transfer of the reactant from the gas phase to the liquid phase and the reaction itself that can occur in the liquid film, in the liquid bulk or in both locations. For experimentally determining the associated reaction characteristic time, it is essential to eliminate the influence of the gas-liquid mass transfer. For that, one of the most commonly used method consists in previously dissolving the reactant contained in the gas phase in the solvent present in the other phase (Hikita et al., 1977; Astaria et al., 1983).

To use it as a method to characterize gas-liquid mass transfer, the colorimetric reaction between dihydroresorufin (B) and oxygen must be fast (Dietrich et al., 2013; Yang et al., 2016), thus making quite difficult the acquisition of the associated kinetic parameters, in particular in conventional batch reactors. Indeed, such technologies do not often guarantee that the time required by the reagents to be perfectly mixed (mixing time, t_m) is sufficiently shorter than the characteristic time of the reaction (t_{react_ch}), here typically below 1s. Recently, the use of micromixers in microfluidic devices has been proven to be an interesting solution for kinetic data acquisition, as overcoming the conventional mixing limitations (Yoshida, 2015; Hecht et al., 2007).

Consequently, in the present study, it has been thus chosen to carry out the fast colorimetric reaction between oxygen and dihydroresorufin solution in a microchannel equipped with a micromixer. In addition, the experiments will be performed by using deionized water previously saturated with O_2 to avoid any gas-liquid mass transfer limitations. The associated experimental set-up will be described in the subsection 2.2.2.

2.1.3 Brief state- of- art about the optical methods for measuring diffusion coefficients

Due to their advantages, such as quick response, real-time analysis of regions, non-invasive and high-resolution, the optical methods have been widely developed to study the diffusion process since the pioneering work of Hauf and Grigull (1970). Qualitative and quantitative data could be acquired by optical methods, and then compared with analytical or numerical investigations in order to develop more complete phenomenological models for the diffusive mechanisms (Ambrosini et al., 2008). Traditional optical approaches such as Taylor's method (Taylor, 1953) have been commonly developed and employed to measure diffusion coefficients in liquids. The principle of Taylor's method is to inject a sharp pulse of solute into a slow and steady laminar flow of solvent in a tube of circular section and suitable length; the solute then flows with the mean velocity of the solvent flow and shows much pronounced axial dispersion by the combined action of the parabolic velocity profile and the radial molecular diffusion. The main limitation of this method is to require relatively long capillary and so long time experiments (several hours). In the last decade, the development of lasers and electronic cameras has enabled

to make a considerable progress in the development of new optical measurement techniques, for example holographic interferometry (Ruiz-Bevia et al., 1985), speckle technique (Mohan and Rastogi, 2003) and planar laser-induced fluorescence (PLIF) system (Jimenez et al., 2013). Such laser-based methods have the same common limitations, such as requirement of specific light source, and not easy to conduct.

In the present study, an original optical technique will be proposed to measure the diffusion coefficients. It is based on the laminar diffusion of molecules in a co-flow microfluidic device and on the visualization of the change of colors occurring when the diffusion and the colorimetric reaction take place. The main advantages of this method are to avoid the use of laser and to be less time-consuming compared with conventional optical approaches. The experimental set-up for implementing the technique will be described in the section 2.2.

2.2 Material and methods

As highlighted in section 2.1, three parameters have to be determined to calculate the Hatta number *Ha* and the enhancement factor *E* associated with the O_2 colorimetric reaction: the kinetics constant k_2, and both diffusion coefficients of dihydroresorufin and O_2, D_B and D_{O_2}. In this section, the three experimental set-ups used to determine these parameters will be described as well as the operating conditions and the image acquisition and post-treatment methods implemented.

2.2.1 Fluid properties

All the experiments were performed at 293.15 K and atmospheric pressure. The dye solution consisted of D-glucose anhydrous (Fischer Scientific®, CAS 50-99-7), sodium hydroxide (VWR®, CAS 1310-73-2), both diluted at 20 $g \cdot L^{-1}$ in deionized water (conductivity: 51.2 $\mu S \cdot m^{-1}$), and resazurin (Sigma Aldrich®, CAS 62758-13-8, molecular mass: 229.19 $g \cdot mol^{-1}$) which concentration was fixed at 0.117 g L^{-1} (5.10×10^{-4} $mol \cdot L^{-1}$). The concentration of resazurin was chosen with respect to the reaction stoichiometry and to the oxygen concentration at saturation $C_{O_2}^*$ in the reactional medium, namely, $C_{Bb} = 2 \cdot C_{O_2}^*$. The density ρ_L, dynamic viscosity μ_L and

static surface tension σ_L were measured by means of a pycnometer ($\rho_L \pm 0.2$ kg·m^{-3}), a RM180 Rheomat Rheometric Scientific® viscometer ($\mu_L \pm 10^{-3}$ mPa·s), and a Digidrop GBX® or Krüss tensiometer ($\sigma_L \pm 0.5$ mN·m^{-1}) respectively. The oxygen saturation concentration $C^*_{O_2}$, was measured by implementing the Winkler technique (Winkler, 1888) and by means of optical oxygen probes (Hach-Lange®). All the physicochemical properties are reported in **Table 2-1**.

Table 2-1 Physicochemical properties of the liquid phases at 293.15K.

Liquid phase	C (kg·m^{-3})	σ_L (mN·m^{-1})	μ_L (mPa·s)	ρ_L (kg·m^{-3})	C^* (mg·L^{-1})
Deionized water	0	71.4	1.003	996.8	9.05
Aqueous solution of glucose anhydrous and sodium hydroxide	20 20	76	1.118	1004.5	8.15 (Dietrich et al., 2013)
Aqueous solution of glucose anhydrous sodium hydroxide and resazurin	20 20 0.1	75	1.118	1004.5	-

2.2.2 Experimental set-up for measuring the reaction characteristic time

The experimental set-up implemented to measure the reaction characteristic time is illustrated in **Fig. 2-1**. It consisted of a microfluidic device composed by a transparent PTFE tube (inner diameter d = 1 mm) fixed at the outlet of a micromixer. The SIMM-V2 micromixer (Slit Interdigital Micromixer, IMM Germany) was chosen to efficiently mix the two liquid phases. The cross-sectional area of its standard mixing channel A_m was 45×200 µm^2 and its inner volume V_m was 8 µL. Two high pressure syringe pumps (neMESYS high pressure syringe pump module, highest pressure up to 510 bar, Cetoni© GmbH, Germany) were used to deliver the deionized water saturated with O_2 and the dye solution from two 20 mL syringes, each connected to the micromixer by a transparent PTFE tube (inner diameter d = 1 mm). The dye solution (B) was previously flushed with nitrogen and was thus colorless when entering in the micromixer. The volumetric flow rates of these two liquid phases (Q_W : deionized water saturated with O_2; Q_R :

dye solution) were identical in all the experiments, which both ranged from 80 to 2000 $mL \cdot h^{-1}$. The associated liquid velocities inside the micromixer were defined by:

$$u = (Q_W + Q_R) / A_m \qquad \text{(Eq. 2-15)}$$

They varied from 4.94 to 123.46 $m \cdot s^{-1}$, and the corresponding Reynolds number *Re* ($= \rho_L \cdot d_h \cdot u / \mu_L$, d_h: hydraulic diameter of the micromixer, m) from 326 to 8152. A LED light source (Rosco®, LitePad HO90) and a camera (dnt®, DigiMicro 2.0 Scale) were set at the outlet of the micromixer to acquire images of the solution leaving the micromixer.

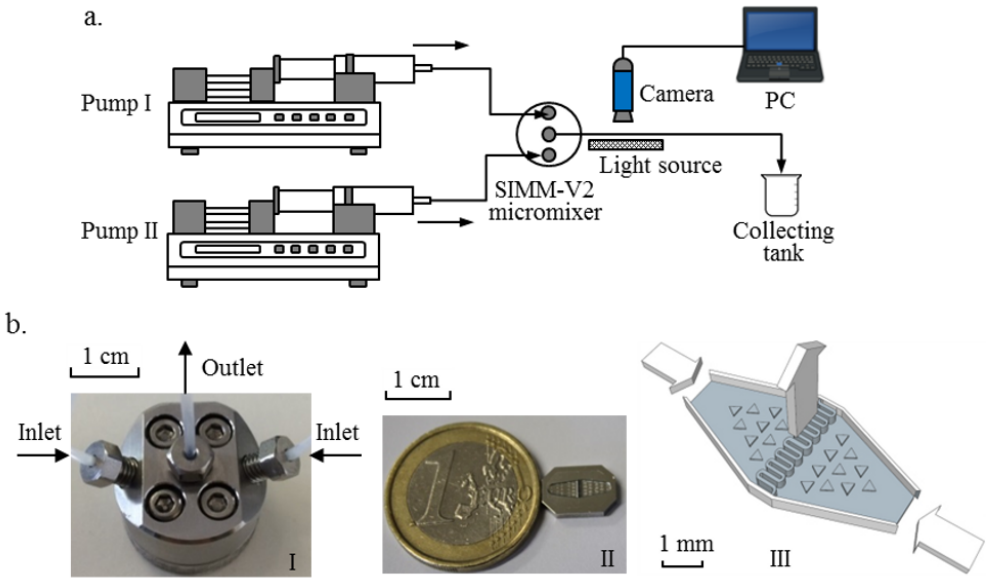

Fig. 2-1 (a) Schematic diagram of micromixer experiment. Pump I: neMESYS high pressure syringe pump for deionized water saturated with O_2; pump II: neMESYS high pressure syringe pump for dye solution (nitrogen flushed). (b) Picture (I); inner structure (II); illustration of the mixing channel (45×200μm) (III) of SIMM-V2 micromixer.

2.2.3 Experimental set-up for the measuring the diffusion coefficient of dihydroresorufin D_B

Since dihydroresorufin (noted as B) is colorless, it is impossible to visualize it experimentally, whereas for the pink resorufin (noted as C), it is possible. Note that the molecular formula of dihydroresorufin being quite similar to that of resorufin apart from the hydrogen ion

(see in **Fig. 1-7**), it can hereafter be assumed that the diffusion coefficient of dihydroresorufin D_B is equal to the one of resorufin.

The experimental set-up for measuring D_B was based on the concept of the two-liquid phase quasi-steady laminar co-flow dispersion (Galambos and Forster, 1998; Kamholz et al., 2001). A T-junction 3 way connector was used to generate the laminar co-flow. The experimental set-up is illustrated in **Fig. 2-2** (a) and (b). The dye solution (previously saturated with O_2 to make sure that all the dihydroresorufin was converted to pink resorufin) and deionized water saturated with O_2 were delivered from a 60 mL syringe by syringe pumps III and IV (Harvard Apparatus, PHD 22/2000, USA) respectively. The connections to the two inlets of the T-junction connector were different for each solution: a capillary (inner diameter $d_{c,in}$ = 250 µm, outer diameter $d_{c,out}$ = 365 µm, cross-sectional area $A' = \pi \cdot d^2_{c,in} / 4 = 4.91 \times 10^{-8}$ m^2), and a transparent PTFE tube (inner diameter $d_{t,in}$ = 1 mm, outer diameter $d_{t,out}$ = 3 mm). At the outlet of the connector, the capillary was carefully inserted and aligned to the central axis of the tube. Such experimental set-up made possible to generate two-liquid phase laminar co-flows under appropriate operating conditions. The dye solution was injected from the capillary and the deionized water saturated with O_2 from the PTFE tube, which meant that the flow of the dye solution was surrounded symmetrically and annularly by the deionized water at the outlet tube of the connector (see **Fig. 2-2**. b). The same camera as in the micromixer experiments was set at the outlet of the connector to record the radial profiles of pink color intensity and their evolution along the axial position in the PTFE tube.

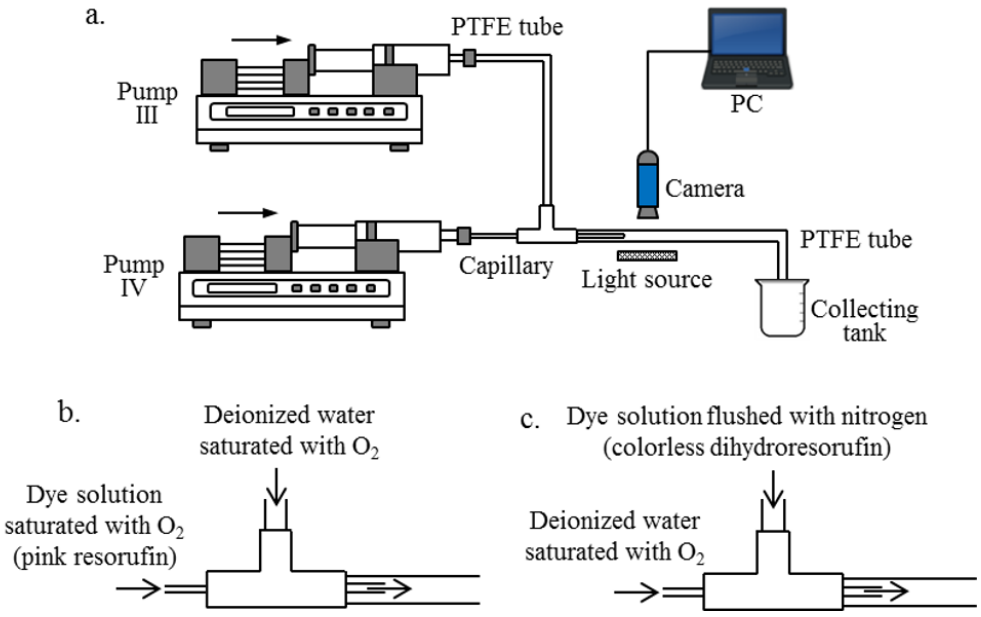

Fig. 2-2 (a) Experimental set-up for the measurement of diffusion coefficients: general overview. Schematic diagram at the connector for measuring D_B (b) and D_{O_2} (c).

The volumetric flow rates of these two liquid phases (Q_W' for deionized water saturated in oxygen; Q_R' for dye solution) were both ranged from 3 to 12 mL·h^{-1}. The associated liquid velocities u' $(= Q_R'/A')$ inside the capillary were ranged between 0.017 m·s^{-1} and 0.068 m·s^{-1}, the capillary numbers Ca' $(= \mu_L \cdot u'/\sigma_L)$ from 2.53×10^{-4} to 1.01×10^{-3}, and the Reynolds numbers Re' $(= \rho_L \cdot d_h' \cdot u'/\mu_L, d_h'$: hydraulic diameter of the capillary, m) from 4.2 to 16.9.

2.2.4 Experimental set-up for measuring the diffusion coefficient of oxygen D_{O_2}

The experimental set-up to measure D_{O_2} was identical to the one described to measure D_B, except that the deionized water saturated with O_2 was injected from the capillary and the dye solution (previously flushed by nitrogen, colorless dihydroresorufin) from the tube. As a consequence, in this case, the flow of deionized water was surrounded symmetrically and annularly by the dye solution at the outlet tube of the connector. Both volumetric flow rates ranged from 3 to 12 mL·h^{-1}. The associated liquid velocities u'' inside the capillary were defined

as 0.017 m·s^{-1} $\leq u'' = Q_W'' / A' \leq$ 0.068 m·s^{-1}, and the Reynolds numbers Re'' $(= \rho_{L,W} \cdot d_h' \cdot u'' / \mu_L)$ ranged from 4.2 to 16.9.

2.2.5 Image acquisition and post-treatment

For all the experiments, the digital micro camera (dnt®, DigiMicro 2.0 Scale) was used to record the images after the establishment of the steady state (around 15 min). The acquired images were colorful. In a first step, a background image was subtracted from the raw images to eliminate the eventual effect of a non- uniform distribution of backlight. The images were then converted to greyscale images using Matlab (R2011b) software, thus enabling to extract a grey value (noted as GV) for each pixel of the image. Due to the established linear relationship between GV and the extent of the colorimetric reaction for a given concentration of resazurin (i.e. the amount of the reacted oxygen) (Dietrich et al., 2013; Yang et al., 2016b), these grey values GV measured were directly proportional to the concentrations of dihydroresorufin or to the equivalent concentration of dissolved oxygen. Note that in this study, as being not necessary, the calibration curve enabling to transform GV to the corresponding equivalent concentration of O_2 (i.e. calculation of the linear proportionality coefficient) was not determined.

For the micromixer experiment, an average grey value, noted as $\overline{GV}$, was calculated by averaging the grey values GV at each pixel of the image taken at the outlet of the micromixer under each operating condition. Almost ten images were used to calculate $\overline{GV}$.

For the experiments related to the measurement of the diffusion coefficient of D_B, a typical image is displayed in **Fig. 2-3** (a). It was decided to choose the origin of the radial *r*-axis at the midline of the capillary and the origin of the axial *z* axis at the outlet of the capillary. By image treatment, the grey value of each pixel along the *r*-direction at a given axial position *z*, noted as $GV(r,z)$, could be extracted. From this, the maximum grey value, noted as $GV_{\max}(r,z)$, associated to a given radial profile could be obtained. The value of $GV_{\max}(r,z)$ was found to be unchanged at various *z*, and was then noted $GV_{\max}$. The grey value of the background image was

noted $GV_0(r,z)$. At last, $GV(r,z)$ was normalized using $GV_{\max}$ and $GV_0(r,z)$, leading to define GV^* such as:

$$GV^* = \frac{GV(r,z) - GV_0(r,z)}{GV_{\max} - GV_0(r,z)} \quad \text{(Eq. 2-16)}$$

The radial location *r* was also normalized by the diameter of the tube, noted as *r**.

The evolution of the normalized grey value GV^* (which are proportional to the normalized concentration of resorufin) as a function of the normalized radial position *r** is shown in **Fig. 2-3** (b) for various axial positions *z*. It can be observed that:

- (i) in the central zone of the colored flow corresponding to radial positions *r** below 0.3, the normalized grey value remains almost unchanged (approximately to be 1) whatever the axial position. This value of 0.3 does not exactly correspond to the diameter of the inner capillary, 0.25 mm; this can be explained by the fact that for the high concentration zone, the color intensity is more sensitive to the concentration of the resorufin. Thus it is reasonable to have a higher $GV(r,z)$ (close to $GV_{\max}$) at the position near the outlet of the capillary.
- (ii) a high gradient area exists close to the edge of the colored flow, thus illustrating the occurrence of the diffusion process. It is precisely this high gradient area that will be used in the modelling section afterwards (see section 2.4.2).

For the experiments related to the measurement of the diffusion coefficient of D_{O_2}, the same method was employed to obtain the evolution of the normalized grey value GV^* versus the normalized radial position *r**.

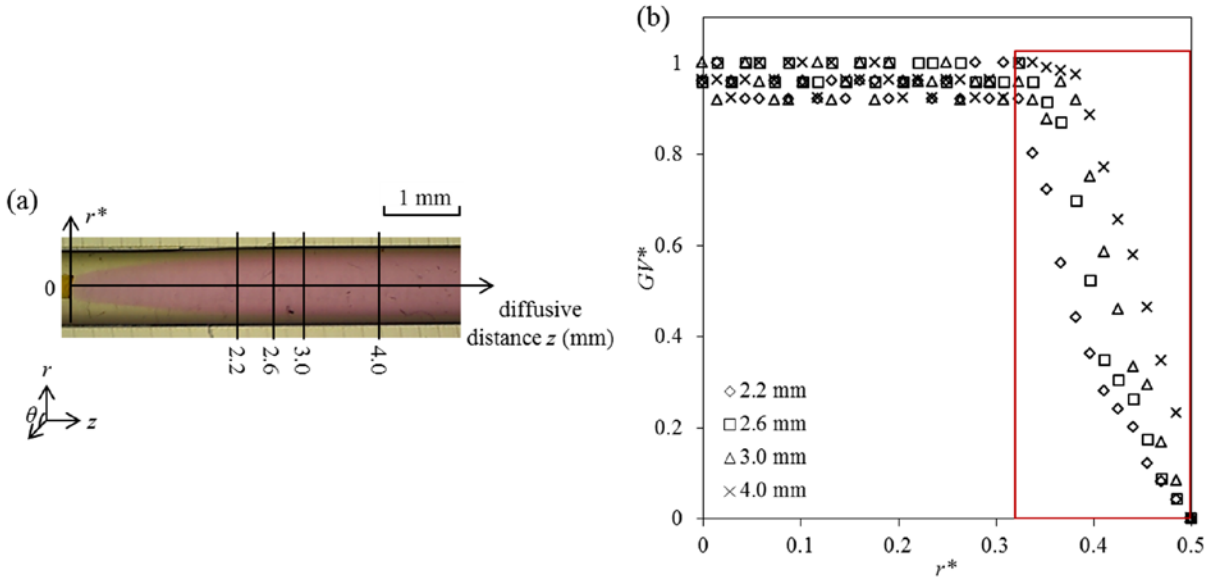

Fig. 2-3 Experiments related to the measurement of the diffusion coefficient of dihydroresorufin D_B. (a) Typical image representing the evolution of color intensity distribution inside the tube. (b) Normalized radial profile of grey values (proportional to the normalized concentration of resorufin) for various axial positions *z*. (Q_R'=3 mL·h^{-1}, Q_W'=3 mL·h^{-1}; *Re'* = 3.82). The experimental data in the red rectangular are the ones that will be used afterwards for the comparison with the theoretical profiles.

2.3 Modeling methods

The diffusion coefficients of both dihydroresorufin and oxygen will be determined by identification of the experimental radial profiles of concentrations (grey values) with the theoretical ones.

To predict the concentration fields resulting from a purely diffusion mechanism, the classical diffusion equation based on a material balance should be considered. In cylindrical coordinates, it is written as (Fick, 1855):

$$\frac{\partial C}{\partial t} = D \cdot [\frac{1}{r} \cdot \frac{\partial}{\partial r}(r \cdot \frac{\partial C}{\partial r}) + \frac{1}{r^2} \cdot \frac{\partial^2 C}{\partial \theta^2} + \frac{\partial^2 C}{\partial z^2}] \qquad \text{(Eq. 2-17)}$$

where r, θ, z are the radial, angular and axial positions in the tube (m) depicted as in **Fig. 2-3** (a); t the diffusion time (s) which is, using the equivalence time-space in the tube, equal to:

$$t = z / u' \qquad \text{(Eq. 2-18)}$$

where u' is the mean velocity of the dye solution in the tube, $m \cdot s^{-1}$.

From **Fig. 2-3** (a), it could be known that the pink zone after the outlet of the capillary presents the colored flow of resorufin by the pressure-driven flow at the capillary outlet. Due to the operations at low Reynolds numbers and low concentrations (convective mass transfer negligible), the two flows were considered as pure laminar, and the transport between them should be diffusive: along the r direction, there should exist only molecular diffusion. As a consequence, for the modelling, it was assumed that (i) the color intensity gradient only appears along the r-direction, (ii) the diffusion along r-direction was axisymmetric (independent of θ), and (iii) the diffusion along the z-direction is negligible. (Eq. 2-17) was then reduced to:

$$\frac{\partial C}{\partial t} = D \cdot [\frac{1}{r} \cdot \frac{\partial}{\partial r}(r \cdot \frac{\partial C}{\partial r})] = \frac{D}{r} \cdot \frac{\partial C}{\partial r} + D \cdot \frac{\partial^2 C}{\partial r^2} \qquad \text{(Eq. 2-19)}$$

In the conditions implemented, it can be shown that the first term $\frac{D}{r} \cdot \frac{\partial C}{\partial r}$ could be neglected. (Eq. 2-19) was further reduced to:

$$\frac{\partial C}{\partial t} = D \cdot \frac{\partial^2 C}{\partial r^2} \qquad \text{(Eq. 2-20)}$$

Two methods were investigated to solve this equation, as presented below.

2.3.1 Markov Chain Monte Carlo (MCMC) method

(Eq. 2-20) admits an analytical solution in the cases where the following of boundary and initial conditions are verified:

Boundary condition 1:	$C(r, t) = C_{max}(r, t)$	at $r = d_{c,in}/2$ and $t \geq 0$
Boundary condition 2:	$C(r, t) = C_0(r, t)$	at $r = d_{t, in}/2$ and $t \geq 0$
Initial condition :	$C(r, t) = 0$	at $t = 0$ and $0 \leq r \leq d_{t, in}/2$

where $C_{max}(r, t)$ is the highest concentration (corresponding to the highest grey value, $GV_{\max}(r,t)$), $C_0(r, t)$ is the initial concentration (corresponding to the grey value of the background image $GV_0(r,t)$).

Under these conditions, (Eq. 2-20) admits the following analytical solution (Culbertson, 2002):

For $r > d_{c,in}/2$ *:*

$$\frac{C(r,t) - C_0(r,t)}{C_{\max}(r,t) - C_0(r,t)} = GV^* = 1 - erf\left[\frac{r}{2\sqrt{Dt}}\right] \qquad \text{(Eq. 2-21)}$$

where the error function $erf(\cdot)$ is defined as:

$$erf(u) = \frac{2}{\sqrt{\pi}} \cdot \int_0^u \exp(-\eta^2) \cdot d\eta \qquad \text{(Eq. 2-22)}$$

In a first step, a Markov Chain Monte Carlo (MCMC) method was implemented on Matlab® software in order to solve (Eq. 2-20) (Jimenez et al., 2014) under the relevant initial and boundary conditions. The associated objective was to compare the experimental and theoretical concentration profiles at different times (i.e. *z* axial positions) and to efficiently optimize the different parameters in order to find the best fit between experimental and theoretical data.

For the measurement of the diffusion coefficient of dihydroresorufin D_B (see **Fig. 2-2**. b and **Fig. 2-3**. a), the calculation was firstly done by considering the radial profile of grey value obtained at an axial position close to the outlet of the capillary (*z* = 0.2 mm). It was then observed that the MCMC method provided a highly accurate estimation of the diffusive front (i.e. grey value displacement) with a very good agreement with experimental results (deviation less than 3%, results not shown here). However, the predicted diffusion coefficient D_B, was found to be

equal to 3×10^{-6} $m^2 \cdot s^{-1}$, which is not at all the order of magnitude of the expected diffusion coefficient of macromolecules into liquids (10^{-11} to 10^{-10} $m^2 \cdot s^{-1}$) (Hauf and Grigull, 1970; Leaist, 1988; Quinn et al., 1986). This result suggested that at the outlet of the capillary, (i.e. during the first stages of the diffusion process), some convective effects existed and were dominating over the diffusion process. As a consequence, (Eq. 2-21) and the associated initial and boundary conditions could not be applied with the experimental conditions imposed. For these reasons, another method was implemented to solve (Eq. 2-20) and fit accurately D_B .

2.3.2 Finite difference element scheme

In order to escape from the convective effects occurring at the outlet of the capillary, an alternative calculation method, the explicit FTCS (Forward-Time Central-Space) finite difference element scheme (Kuzmin, 2010), was employed: it enabled to directly solve (Eq. 2-20) without imposed initial conditions, but with using an experimental normalized concentration profile.

As the diffusion process could be considered with an instantaneous plane source (round) and in a semi-infinite medium, (Eq. 2-20) was then reduced to(Crank, 1975):

$$\frac{\partial C}{\partial t} = D \cdot [\frac{\partial^2 C}{\partial x^2} + \frac{\partial^2 C}{\partial y^2}] \qquad \text{(Eq. 2-23)}$$

where $x = r \cdot \cos\theta$ and $y = r \cdot \sin\theta, 0 \le \theta \le 2\pi$.

The diffusion process was simulated in Matlab® (R2011b) software starting from an experimental concentration field associated with a time t_0 after a time t_1 under a given D. This time t_0 corresponded to the axial position z for which the edge of the colored flow began to be parallel to the wall of the tube. The resulted simulated profile was then compared to the corresponding experimental profile when diffusion time equal to ($t_0 + t_1$).

It is important to note that for both the diffusions of dihydroresorufin and oxygen, the experimental profiles of grey values were in reality the result of the superposition of all the diffused amount of the molecule at each slice along r axis. As a consequence, it was necessary to

sum up and then average all the concentration profiles predicted by the simulation (i.e. integration over all the radial positions) before comparison with the experimental profiles. Thus by changing the value of *D*, the simulated diffused results varied, and then the numerical results were compared with the experimental ones in order to determine the optimal *D*.

2.4 Results and discussion

2.4.1 Characteristic time of the reaction

Fig. 2-4 represents the variation of the average grey value $\overline{GV}$ as a function of the residence time t_r inside the micromixer, the latter being calculated according to

$$t_r = \frac{V_m}{Q_t} = \frac{V_m}{Q_w + Q_R} \qquad \text{(Eq. 2-24)}$$

It can be observed that when t_r >130.9 ms (at very small flow rates), a segregation phenomenon occurs, characterized by two distinct parallel flows corresponding to the deionized water saturated with oxygen (colorless) and the dye solution (pink). This phenomenon is due to the fact that the flow rates related to t_r >130.9 ms are too small and below the minimum flow rate recommended by the supplier for using the micromixer. In these conditions, the micromixer is not able to mix efficiently both solutions.

When t_r <130.9 ms, a plateau is reached, which indicates that the mixing is now efficient. The mixing time t_m associated with this kind of micromixer has been determined by Falk and Commenge (2010): it is almost two orders of magnitude smaller than the residence time (0.04-0.68 ms compared to 7.2-180 ms). This shows that the ability to determine the kinetics of the colorimetric reaction by using this microfluidic device will be imposed by the time t_r spent by the solution inside the micromixer. In other words, the color intensity fields observed at the outlet of the micromixer are related to the extent of the reaction at a time equal to t_r inside the micromixer, even if the fluids are in reality mixed with a significantly smaller time. For technical reasons (too high pressure drop), the minimum t_r that could achieve in the present device is 7.2 ms, this value

can be thus associated to a maximum value of the characteristic time of the reaction, noted $(t_{react\_ch})_{\max}$, that is here experimentally accessible. Here, according to Commenge and Falk (2014), the characteristic time of the reaction under the stoichiometric initial condition of the reactant concentrations ($C_{Bb} = 2 \cdot C_{O_2}^{\ *}$), noted t_{react_ch}, is defined as follow:

$$t_{react\_ch} = \frac{\text{reactant concentration}}{(\text{reaction rate})_{\max}} = \frac{C_{O_2}^{\ *}}{k_2 \cdot C_{O_2}^{\ *} \cdot C_{Bb}} = \frac{C_{B,b}}{2 \cdot k_2 \cdot C_{O_2}^{\ *} \cdot C_{Bb}} \qquad \text{(Eq. 2-25)}$$

This value of $(t_{react\_ch})_{\max}$ identified by default, will be used later for the calculation of the Hatta number (see section 2.4.4).

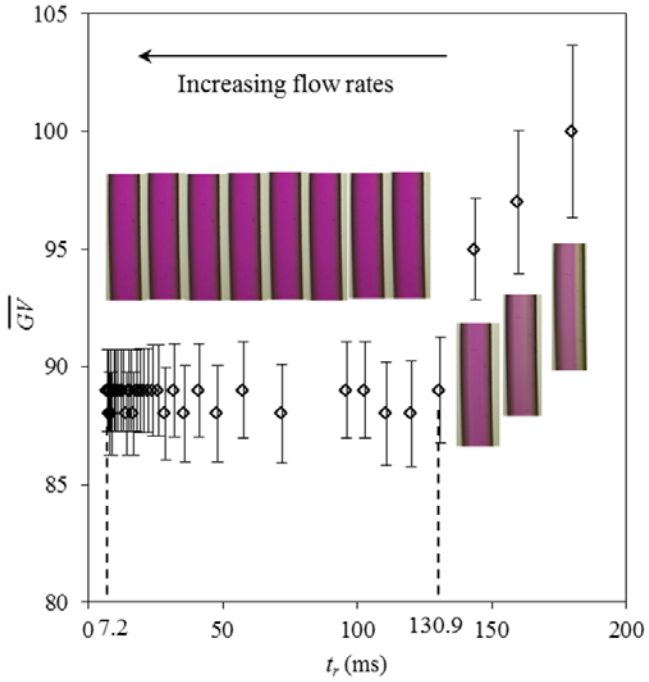

Fig. 2-4 Variation of the average grey value $\overline{GV}$ at the outlet of the micromixer as a function of the residence time in the micromixer t_r. The bars represent the experimental deviations associated to $\overline{GV}$.

2.4.2 Diffusion coefficient of dihydroresorufin D_B in deionized water

As depicted in **Fig. 2-3** (a), the edge of the colored flow is not parallel to the wall of the tube close to the outlet of the capillary due to the axial dispersion generated by some convective mechanisms along the *r* axis direction. Afterwards (i.e. at higher axial locations), the edge of the colored flow becomes parallel to the walls of the tube, thus meaning that the diffusion mechanism of resorufin from the inner flow to the surrounding one is purely radial. For this reason, the radial profile of normalized grey value (proportional to normalized concentration of resorufin) at z = 2.2 mm has been used as an initial condition in the explicit FTCS finite difference element scheme (corresponding to t_0) to simulate the dye concentration profile at z = 2.6 mm (corresponding to t_1). The best fitting between experimental and theoretical profiles has been obtained for $D_B = 2.25\times10^{-9}$ $m^2\cdot s^{-1}$. The comparison between the predicted and experimental profiles at this axial position, is reported in **Fig. 2-5** for $Q_R' = 3$ $mL\cdot h^{-1}$, $Q_W' = 6$ $mL\cdot h^{-1}$; a very good agreement is observed between these profiles. It can be noted that the optimization process has been performed considering the higher gradient area depicted in **Fig. 2-3**. (b), which corresponds to a purely radial diffusive mechanism.

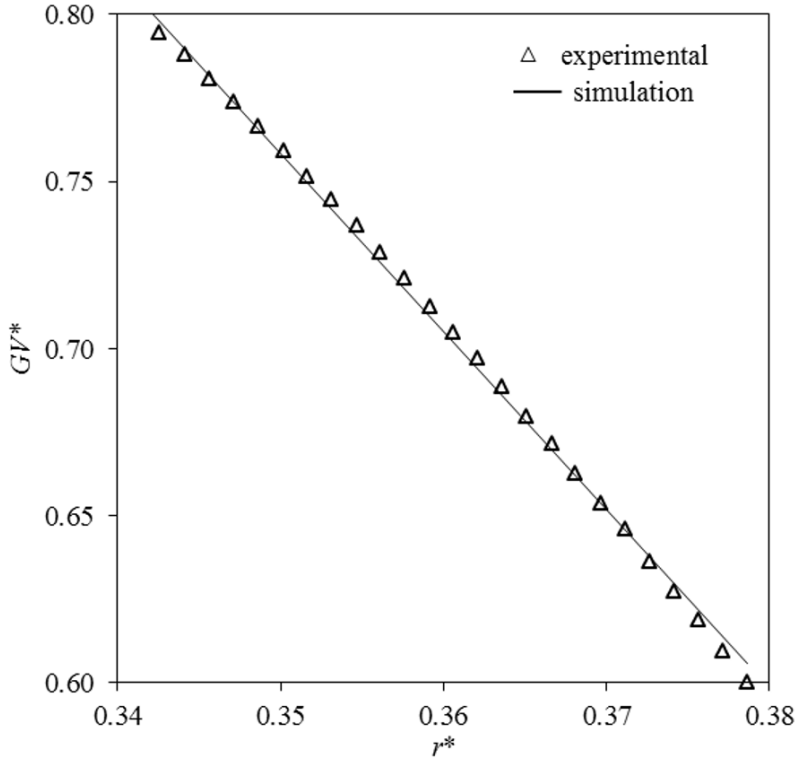

Fig. 2-5 Determination of the diffusion coefficient of dihydroresorufin: comparison of the experimental radial profiles of normalized grey values with the predicted ones at an axial location z = 2.6 mm, and for Q_R' = 3 mL·h^{-1}, Q_W' = 6 mL·h^{-1}. The associated predicted diffusion coefficient is equal to D_B = 2.25×10^{-9} m²·s^{-1}.

To validate this value of D_B, this procedure has been repeated for several positions z (higher than 2.6 mm), using the experimental profile at the previous axial position for each one, and under two operating conditions (Q_R' = 9 mL·h^{-1}, Q_W' = 9 mL·h^{-1}) and (Q_R' = 3 mL·h^{-1}, Q_W' = 6 mL·h^{-1}). In **Fig. 2-6**, the variation of the predicted diffusion coefficients D_B is reported as a function of the axial position z. It can be observed that, for both conditions, the value of D_B decreases as z increases, and then converges towards a plateau for z greater than 4 mm. This indicates that the fitting between the experimental and theoretical concentration profiles must be done relatively far from the outlet of the capillary, namely only for axial positions z for which the edge of the colored flow starts to be parallel to the wall of the tube. Note that, this plateau is reached at smaller axial positions for (Q_R' = 3 mL·h^{-1}, Q_W' = 6 mL·h^{-1}) than for Q_R' = 9 mL·h^{-1}/

Q_W' = 9 mL·h^{-1}; this could be explained by the conic structure of the flow which is more stable/horizontal in the latter operating condition. For both conditions, after the z = 4 mm position, the optimization procedure gives a value of the diffusion coefficient of dihydroresorufin D_B = (8.65 ± 0.21)×10^{-11} m²·s^{-1}. This value is in agreement with the orders of magnitude of the diffusion coefficients of dye classically reported in the literature: for example, the diffusion coefficient of "meta" benzopurpurine in 0.002 M NaOH solution (Robinson, 1935) is 3.15 ×10^{-10} m²·s^{-1}, and the one of methylene blue in 0.01 M NaCl solution (Leaist, 1988) being 1.2 ×10^{-10} m²·s^{-1}.

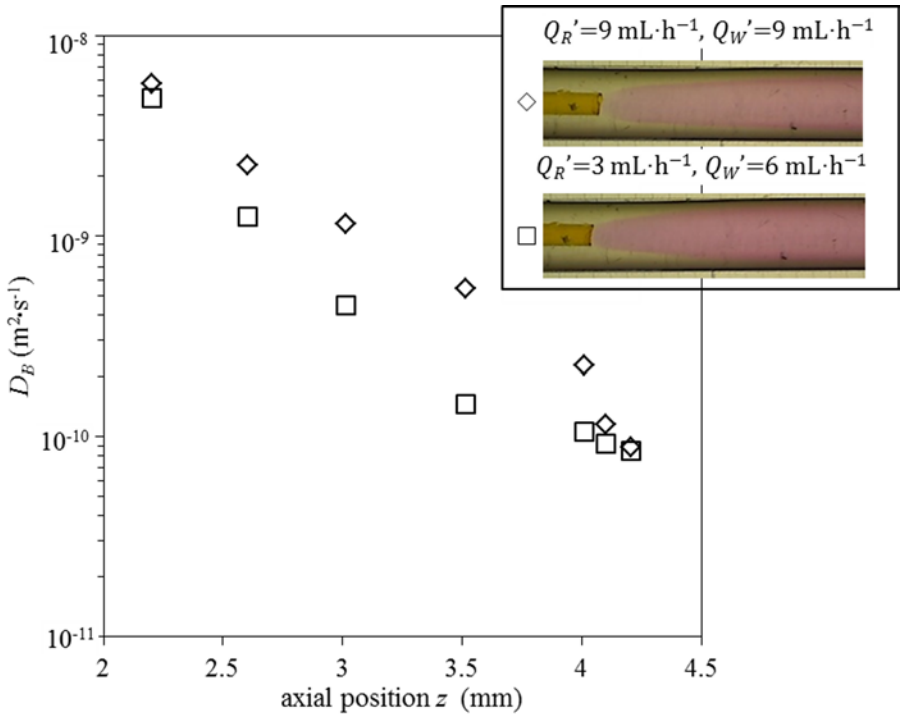

Fig. 2-6 Determination of the diffusion coefficient of dihydroresorufin: variation of the predicted D_B as a function of the axial position z.

2.4.3 Diffusion coefficient of oxygen D_{O_2} in the dye solution

Fig. 2-7 (a) shows a typical image illustrating the diffusion of O_2 in the dye solution (Q_R'' = 9 mL·h^{-1}, Q_W'' = 9 mL·h^{-1}): the pink color represents the areas where the two solutions (deionized water saturated with O_2 and dihydroresorufin solution) enter into contact and react. As observed

previously, for the measurement of D_B, the edge of the colored flow is not parallel to the wall of the tube at the initial stage (i.e. close the outlet of the capillary), due to the occurrence of some convective effects; afterwards, the profile becomes parallel, indicating a pure diffusion of oxygen from the inner flow to the surrounding. As a consequence, here also, in order to determine an appropriate value of D_{O_2}, adequate axial positions should be chosen as initial moment for simulation (t = 0 s). An axial position of z = 2.30 mm has been selected.

As shown in **Fig. 2-7** (b), the radial profile of grey values presents a more complicated shape for the diffusion of oxygen in the dye solution than for the one of dihydroresorufin in deionized water. Indeed, it consists of three parts: two peaks and one central plateau between the two peaks. The peaks correspond to the highest gradients of the concentration of O_2, and thus represent the main contribution to the overall diffusion process. The predicted value of D_{O_2} corresponding to the profiles reported in **Fig. 2-7** (b) equals to 5×10^{-7} m^2 s^{-1}; it is two orders of magnitude larger than the one in literature (Galambos and Forster, 1998), this indicating that, at this axial location (z = 2.30 mm), the mechanism is not purely diffusive.

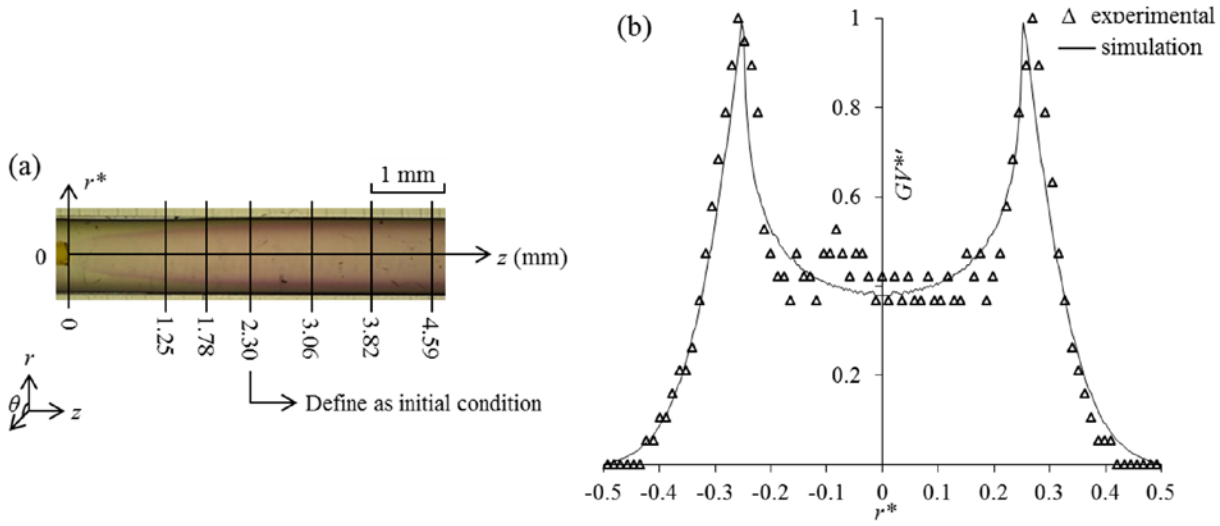

Fig. 2-7 Determination of the diffusion coefficient of oxygen: (a) Typical experimental image representing the diffusion of O_2 in the dye solution; (b) Comparison between the experimental radial profile of the normalized grey values $GV^{*'}$ with the predicted one at an axial location z = 2.3 mm and for $Q_R'' = 9$ mL·h^{-1}, $Q_W'' = 9$ mL·h^{-1}. The associated predicted value of diffusion coefficient is $D_{O_2} = 5\times10^{-7}$ m^2·s^{-1}.

Fig. 2-8 compares the experimental radial profiles of grey values (proportional to equivalent concentrations of O_2) at an axial position z of 4.59 mm with the simulated ones for different values of diffusion coefficients D_{O_2}. It can be observed that the impact of these latter is not the same, depending on that whether the peak areas or the plateau area is considered. Given that the peaks represent the main contribution to the diffusion process, a compromise amongst the fitting qualities of the three parts has to be found. For that, the peak thickness, noted as $\delta_{0.9}$, corresponding to a normalized grey value $GV^{*\prime} = 0.9$, has been chosen for a comparison purpose. Their experimental and predicted values are reported in **Table 2-2** (a) at an axial position z of 4.59 mm. It can be seen that the deviation between the experimental $\delta_{0.9}$ and the simulated one is minimal when $D_{O_2} = 3.2\times10^{-9}$ m^2·s^{-1}.

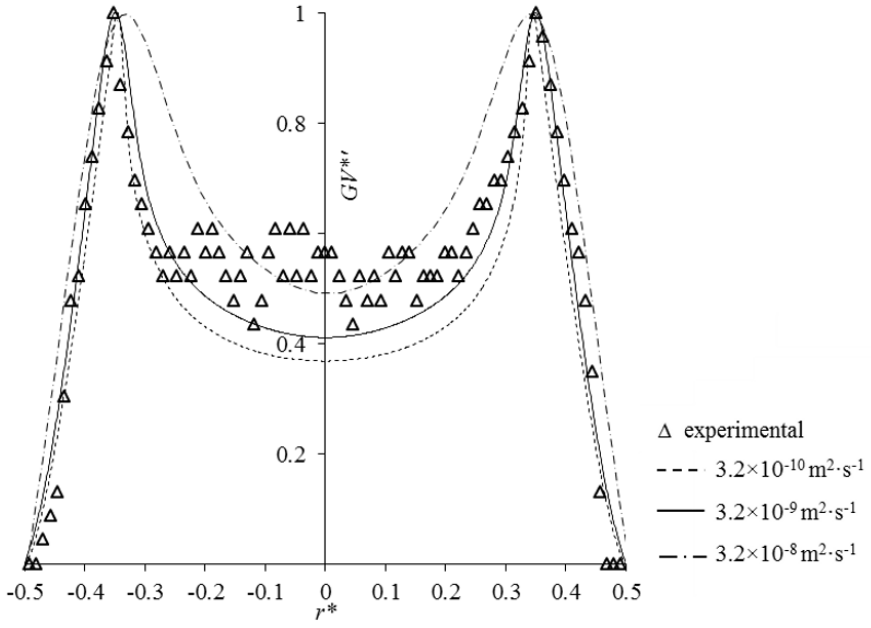

Fig. 2-8 Determination of the diffusion coefficient of oxygen: comparison between the experimental radial profiles of the normalized grey values with the predicted ones at an axial location z = 4.59 mm for different values of D_{O_2} ($Q_R{}'' = 9$ mL·h^{-1}, $Q_W{}'' = 9$ mL·h^{-1}).

Table 2-2 Diffusion peak thickness at normalized concentration of O_2 equal to 0.9, $\delta_{0.9}$: comparison between simulation and experimental values (axial distance z = 4.59 mm). Experimental operating conditions: a. Q_R'' = 9 mL·h^{-1}, Q_W'' = 9 mL·h^{-1}; b. Q_R'' = 4.5 mL·h^{-1}, Q_W'' = 9 mL·h^{-1}; c. Q_R'' = 3 mL·h^{-1}, Q_W'' = 6 mL·h^{-1}.

a

D_{O_2} (m^2·s^{-1})	3.2×10^{-10}	3.2×10^{-9}	3.2×10^{-8}	$\delta_{0.9,exp}$ (mm)
$\delta_{0.9}$ (mm)	0.020	0.032	0.058	0.030
Deviation	33.33%	6.67%	93.33%	

b

D_{O_2} (m^2·s^{-1})	3.2×10^{-10}	3.2×10^{-9}	3.2×10^{-8}	$\delta_{0.9,exp}$ (mm)
$\delta_{0.9}$ (mm)	0.024	0.028	0.057	0.029
Deviation	17.24%	3.45%	96.55%	

c

D_{O_2} (m^2·s^{-1})	3.2×10^{-10}	3.2×10^{-9}	3.2×10^{-8}	$\delta_{0.9,exp}$ (mm)
$\delta_{0.9}$ (mm)	0.022	0.030	0.059	0.031
Deviation	29.03%	3.23%	90.32%	

To further verify the reliability of this value of D_{O_2}, two other axial locations, z = 3.06 mm and z = 3.82 mm, were tested for the operation condition corresponding to Q_R'' = 9 mL·h^{-1}, Q_W'' = 9 mL·h^{-1}. As depicted in **Fig. 2-9**, the best fitting quality between experimental and predicted profiles is obtained for the highest axial location (z = 4.59 mm). This confirms that the procedure should be applied relatively far from the outlet of the capillary, to avoid any distortion due to convective effects.

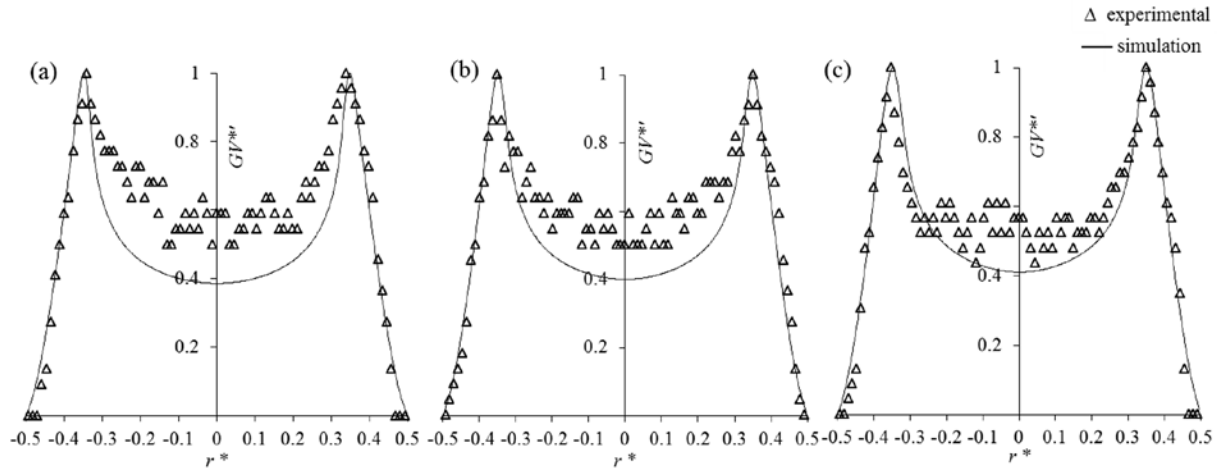

Fig. 2-9 Determination of the diffusion coefficient of oxygen: comparison between the experimental radial profiles of the normalized grey values with the predicted ones for a predicted value of D_{O_2} equal to 3.2×10^{-9} $m^2\cdot s^{-1}$ and for different axial positions z. (a) z = 3.06 mm. (b) z = 3.82 mm. (c) z = 4.59 mm. (Q_R'' = 9 $mL\cdot h^{-1}$, Q_W'' = 9 $mL\cdot h^{-1}$).

For this optimal axial location z of 4.59 mm, the same fitting procedure has been applied for two other operating conditions, (Q_R'' = 4.5 $mL\cdot h^{-1}$, Q_W'' = 9 $mL\cdot h^{-1}$) and (Q_R'' = 3 $mL\cdot h^{-1}$, Q_W'' = 6 $mL\cdot h^{-1}$); the results are presented in terms of peak thickness $\delta_{0.9}$ in **Table 2-2** (b) and (c). For both conditions, the best fitting is obtained for D_{O_2} equal to 3.2×10^{-9} $m^2\cdot s^{-1}$. The variations of the predicted diffusion coefficients D_{O_2} as a function of the axial location z are plotted in **Fig. 2-10** for different operating conditions. As previously observed for the diffusion coefficient of dihydroresorufin D_B, for both conditions, D_{O_2} decreases strongly as z increases, and converges towards a plateau for z larger than 4 mm. At last, by optimizing both the conditions, one finds D_{O_2} = $(3.2 \pm 0.1)\times10^{-9}$ $m^2\cdot s^{-1}$. This value D_{O_2} has the same order of magnitude D_{O_2} than the one in pure water, 1.75×10^{-9} $m^2\cdot s^{-1}$, reported in the literature (Wilke and Chang, 1955; Galambos and Forster, 1998). A more advanced comparison with literature data remains difficult as the present liquid phase composition is specific (sodium hydroxide, glucose and resazurin). One can yet mention the value of 3.5×10^{-9} $m^2\cdot s^{-1}$, reported by Yano (1998) for the diffusion of oxygen in 0.1 M KOH solution.

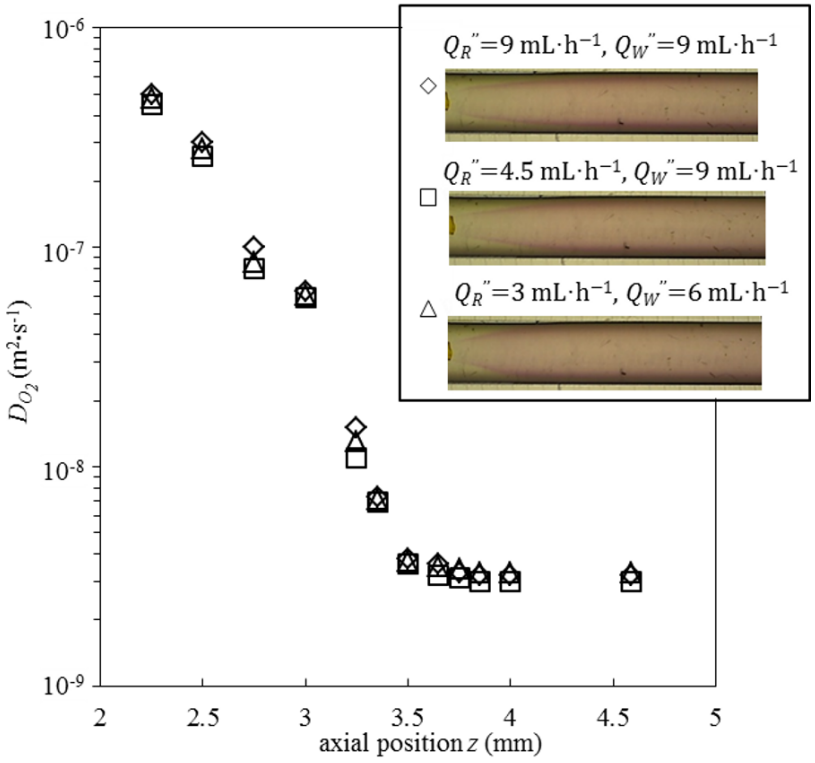

Fig. 2-10 Variation of the diffusion coefficient of oxygen D_{O_2} as a function of axial position *z* for different operating conditions.

2.4.4 Hatta number Ha and enhancement factor E

With the knowledge of the diffusion coefficients of O_2 (D_{O_2} = (3.2 ± 0.1)×10^{-9} m^2·s^{-1}) and of dihydroresorufin (D_B = (8.65 ± 0.21)×10^{-11} m^2·s^{-1}), the enhancement factor associated with the colorimetric reaction can be calculated using (Eq. 2-13). Considering a concentration of dihydroresorufin in the liquid bulk C_{Bb} equals to 5.1×10^{-4} mol·L^{-1} and a concentration of oxygen at saturation $C_{O_2}^*$ to 2.55×10^{-4} mol·L^{-1}, it leads to:

$$E_i = 1 + \frac{C_{Bb} \cdot D_B}{\nu \cdot C_{O_2}^* \cdot D_{O_2}} = 1.03 \pm 0.01 \qquad \text{(Eq. 2-26)}$$

To verify that the approximated solution proposed by Van Krevelen and Hoftijzer (Eq. 2-14) for fast reaction in the diffusional film can be applied in the present conditions, the Hatta number should be calculated. The use of (Eq. 2-14) requires the knowledge of the reaction kinetics constant, k_2 and the liquid-side mass transfer coefficient, k_L. The constant k_2 can be deduced from the "estimated" characteristic time t_{react_ch}.

As only its maximum value has been determined ($t_{char} \leq 7.2$ ms, see section 2.4.1), only the minimum value of the reaction constant k_2 can be calculated according to (Eq. 2-25), as follows:

$$(k_2)_{\min} = \frac{1}{\nu \cdot (t_{react\_ch})_{\max} \cdot C^*_{O_2}} = 2.72 \times 10^5 \ \text{L}\cdot(\text{mol}\cdot\text{s})^{-1} \qquad \text{(Eq. 2-27)}$$

The liquid side mass transfer coefficient k_L depends on the system scale under study. For micro/milli reactors, an order of magnitude of 10^{-4} m·s^{-1} can be reasonably considered (Shvydkiv et al., 2012; Su et al., 2015). At last, one finds a minimal value of the Hatta number equals to:

$$(Ha)_{\min} = \frac{\sqrt{(k_2)_{\min} \cdot C_{Bb} \cdot D_{O_2}}}{k_L} = 6.66 \qquad \text{(Eq. 2-28)}$$

The value being higher than 3, $Ha > 3$, the approximated solution proposed by Van Krevelen and Hoftijzer (1948) (see Eq. 2-14) can be rigorously applied. It leads to a value of the enhancement factor close to the unity, $E = 1.03$.This demonstrates that even if the colorimetric reaction is fast, and even quasi-instantaneous, there is no enhancement of the gas-liquid mass transfer by the reaction in the conditions (C_{Bb}, milli/microreactors) for which it has been implemented. Such a result is opposite to the general knowledge that high Ha lead to high E; it is the consequence of the fact that the diffusion of the dye (dihydroresorufin) in the liquid film is too slow ($D_B = 8.65\times10^{-11}$ m^2·s^{-1}) compared to the diffusion of oxygen ($D_{O_2} = 3.2\times10^{-9}$ m^2·s^{-1}), and thus prevents the reaction to occur in the liquid film.

2.5 Extended study

The results presented in this section is an extended study following the previous work, aiming to access to an exact characteristic time of the colorimetric reaction. These results have not been published yet

As shown in section 2.4.1, only the maximum value of the characteristic time of the colorimetric reaction (7.2 ms) could be determined. To reach the exact characteristic time of the reaction, one simple way was to decrease the concentration of resazurin. As a consequence, attempts have been made by quartering the previous concentration of resazurin, namely, decreasing C_{Bb} from 5.10×10^{-4} mol·L^{-1} to 1.28×10^{-4} mol·L^{-1}. The implementation of the experiments was the same as described in section 2.3.2 for measuring the reaction characteristic time.

As shown in **Fig. 2-11**, under $C_{Bb}=1.28\times10^{-4}$ mol·L^{-1}, a decrease of color intensity field (i.e. an increase on the average Grey Value, $\overline{GV}$), was observed at the outlet of the micromixer for residence times t_r inside the micromixer smaller than 8.5 ms. Such trend, that could not be observed for the higher concentration (see **Fig. 2-4**), is very interesting because it indicates that, below this critical value an uncomplete reaction occurs. This part of the curve (below 8.5 ms) can be thus analyzed to determine the kinetic constant, as in a classical kinetic study.

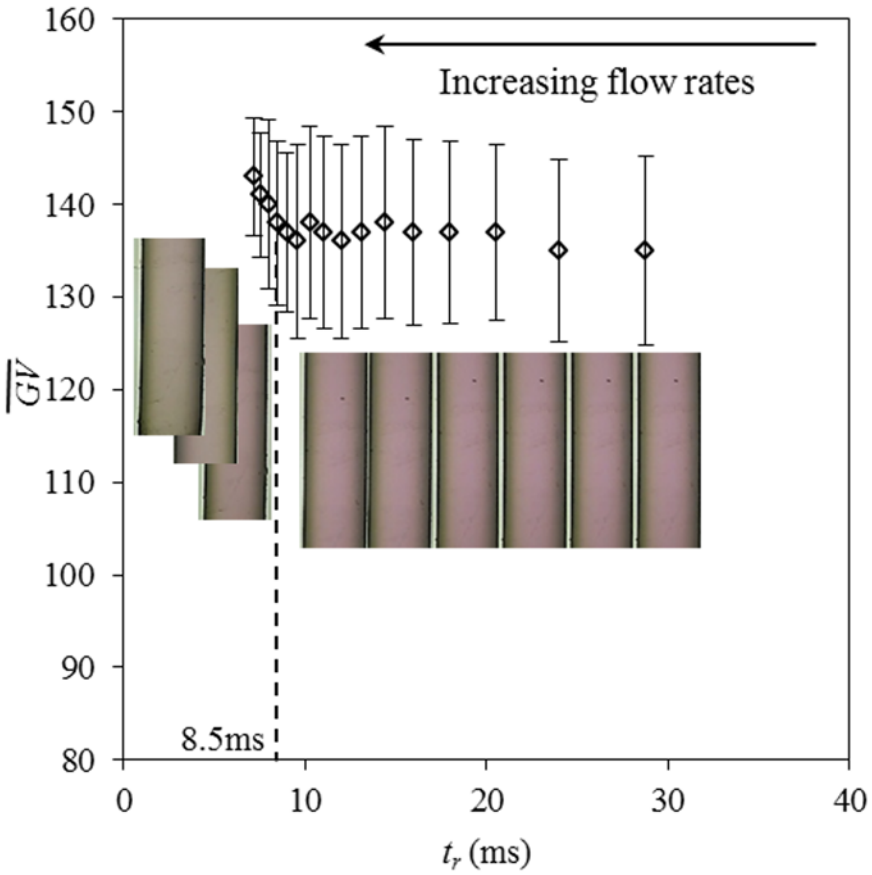

Fig. 2-11 Variation of the average grey value $\overline{GV}$ at the outlet of the micromixer as a function of the residence time in the micromixer t_r under the concentration of resazurin equal to 1.28×10^{-4} mol·L^{-1}. The bars represent the experimental deviations associated to $\overline{GV}$.

For that, let remind that the mass balance equation in the case of a plug-flow reactor in which a second-order reaction (see section 2.1.1) takes place is expressed as following:

$$-\frac{dC_{O_2}}{dt_{react}} = k_2 \cdot C_{O_2} \cdot C_B \qquad \text{(Eq. 2-29)}$$

The concentrations of O_2 and dihydroresorufin at different times are displayed as follow.

Table 2-3 Concentrations of O_2 and dihydroresorufin at different times.

time	Concentration of O_2	Concentration of dihydroresorufin
0	$C_{O_2,0}$	$C_{Bb,0}$
t_{react}	C_{O_2}	$C_{Bb,0}$-2·($C_{O_2,0}$-C_{O_2})

Integrating (Eq. 2-29) from 0 to t_{react} gives the integrated reaction rate law:

$$k_2 \cdot t_{react} = \frac{1}{(2 \cdot C_{O_2,0} - C_{Bb,0})} \ln(\frac{C_{O_2} \cdot C_{Bb,0}}{C_{O_2,0} \cdot C_B}) \qquad \text{(Eq. 2-30)}$$

where the reaction time t_{react} is equal to the residence time t_r; the initial oxygen concentration $C_{O_2,0} = C_{O_2}^*$ is equal to 2.55×10^{-4} mol·L^{-1}, and the initial concentration of dihydroresorufin $C_{Bb,0} = C_{Bb}$ to 1.28×10^{-4} mol·L^{-1}.

Assuming that the conversion of dihydroresorufin η, where $\eta = C_{Bb} / C_{Bb,0}$, equals to 99% at the reaction time $t_{react} = t_r$=8.5 ms and according to the stoichiometric relationship of the reaction (see Eq. 2-1), (Eq. 2-30) turns to:

$$k_2 \cdot t_r = \frac{1}{(2 \cdot C_{O_2,0} - C_{Bb,0})} \ln[\frac{(C_{O_2,0} - 0.5 \cdot \eta \cdot C_{Bb,0}) \cdot C_{Bb,0}}{C_{O_2,0} \cdot C_{Bb}}] \qquad \text{(Eq. 2-31)}$$

Therefore, the reaction constant k_2 can be calculated from (Eq. 2-31), leading to $k_2 = 1.28 \times 10^6$ L·mol^{-1}·s^{-1}. From this, the characteristic time of the reaction can be deduced from (Eq. 2-25), as:

$$t_{react\_ch} = \frac{1}{\nu \cdot k_2 \cdot C_{O_2}^*} = 1.5 \text{ ms} \qquad \text{(Eq. 2-32)}$$

The exact characteristic time of the reaction t_{react_ch} is thus far less than the maximal value obtained previously (7.2 ms)

In this case, the Hatta number becomes equal to (the order of magnitude of 10^{-4} m·s^{-1} of the liquid side mass transfer coefficient k_L is reasonably considered for micro/milli reactors):

$$Ha = \frac{\sqrt{k_2 \cdot C_{Bb} \cdot D_{O_2}}}{k_L} = 14.4 > (Ha)_{\min} = 6.66 > 3 \qquad \text{(Eq. 2-33)}$$

For this value, the enhancement factor remains almost unchanged, close to the unity, E =1.03. This definitively confirms there is no enhancement of the gas-liquid mass transfer by the reaction exists under the classical conditions of the colorimetric method implementation, namely, a resazurin concentration of C_{Bb} = 0.1 g·L^{-1}, and a liquid side mass transfer coefficient k_L close to 10^{-4} m·s^{-1}.

At last, it could be interesting to define some guidelines enabling to evaluate the conditions required to implement the colorimetric method at other scales or in other gas-liquid systems. For that, one should guarantee that the colorimetric reaction is instantaneous (see Chapter 1, section 1.3), and that the enhancement factor E by the reaction could be exactly calculated. Then, depending on the value of E, one can decide whether the experimental result should be corrected (i.e. E is not equal to 1) (or not) by E to obtain the intrinsic k_L. According to Roizard et al. (1997), there mainly exists three regimes for a second order chemical reaction, depending on the value of Hatta number Ha:

(1) $Ha > 3$, the reaction is faster than the mass transfer;

(2) $0.3 < Ha < 3$, the reaction is moderately rapid;

(3) $Ha < 0.3$, the reaction is slower than the mass transfer.

For $Ha > 3$, Ha can be determined from (Eq. 2-9), knowing the initial concentration of resazurin C_{Bb} to be chosen and the mass transfer coefficient k_L of the system under study. $Ha > 3$ guarantees that the colorimetric reaction is faster than the gas-liquid mass transfer, this condition being a prerequisite for the visualization. To fill this condition, the magnitude of k_L

should be approximately below 1.41×10^{-3} m·s^{-1} when the initial concentration of resazurin equals to its solubility (C_{Bb} =1 g·L^{-1}). A maximum value of 1.23 is then found for E using (Eq. 2-13) and (Eq. 2-14). In this case, an enhancement of the mass transfer by the reactor existed, and thus the experimental value of mass transfer coefficient should be corrected by E to obtain the intrinsic k_L.

For the $0.3 < Ha < 3$ zone, E cannot be directly calculated: there exists no simple analytical solution, numerical simulations are required instead according to Benbelkacem (2002). In addition, in this case, it is not excluded that the reaction becomes slower than the gas-liquid mass transfer for the visualization and characterization purpose. Therefore, one recommends not to operate at this zone. For the same reason, $Ha < 3$ should be also avoided.

2.6 Conclusion

This chapter presented original optical methods to determine the Hatta number *Ha* and the enhancement factor *E* associated with the colorimetric reaction proposed by Dietrich et al. (2013) to visualize and locally characterize the gas-liquid mass transfer. It was based on the combination of specific experiments in microstructured devices with modelling approaches. They enabled the characteristic time of the fast reaction to be determined and as well as the diffusion coefficients of the dye (dihydroresorufin) and O_2. It was demonstrated that the oxygen colorimetric reaction was instantaneous and no enhancement of the gas-liquid mass transfer by this extremely fast reaction occurred as *E* was found equal to 1.03 ± 0.01. This result, opposite to the general knowledge, can be explained by the fact that the relative large molecular structure of dihydroresorufin limits its diffusion into the film, and thus prevents the reaction to occur in the liquid film. Some guidelines enabling to evaluate the conditions required to implement the colorimetric method at other scales or in other gas-liquid systems were also given, namely it is recommended to implement this technique when $Ha > 3$, leading to a maximum value of k_L of the system under study for implementing this colorimetric technique should be approximately below 1.41×10^{-3} m·s^{-1} when the concentration of resazurin is maximum as 1 g·L^{-1}. A maximum value of 1.23 is then found for E. In this case, an enhancement of the mass transfer by the

reactor existed, and thus the experimental value of mass transfer coefficient should be corrected by E to obtain the intrinsic k_L.

CHAPTER 3

Gas-liquid mass transfer around a Taylor bubble right after the formation stage in microreactors

Résumé: Dans ce chapitre, la faisabilité de la technique colorimétrique à l'échelle microscopique ainsi que la contribution au transfert de l'étape de formation de la bulle ont été étudiées. Pour cela, le transfert de matière gaz-liquide a été quantifié, dans des écoulements de Taylor, immédiatement après la formation de la bulle, dans un microréacteur de type "*flow-focusing*" de section carrée de 500 × 500 μm^2. Les expériences ont été effectuées dans plusieurs conditions d'écoulement et de tailles des bulles ($2.34 < L_b/l < 5.59$).

Grâce à la technique colorimétrique et un traitement d'image adapté, l'ordre de grandeur des coefficients de transfert de matière côté liquide k_L a pu être obtenu juste après que la bulle se détache du film gazeux près de la zone de formation du microréacteur. Le rapport entre la quantité d'oxygène transférée juste après la formation et celle obtenue à une distance de 14 fois la largeur du canal, a été quantifiée. Les résultats ont montré que la contribution du transfert de matière juste après la phase de formation de bulle est raisonnablement plus grande que celle obtenue au stade d'écoulement des bulles.

Ce chapitre a été publié dans l'article: Yang L., Dietrich N., Loubière K., Gourdon C., Hébrard G. (2016), *Visualization and characterization of gas–liquid mass transfer around a Taylor bubble right after the formation stage in microreactors*. ***Chem. Eng. Sci.*** 143, 364–368. doi:10.1016/j.ces.2016.01.013.

Abstract: In this chapter, the feasibility of the colorimetric technique at microscale was demonstrated and the contribution of bubble formation stage to the overall gas-liquid mass transfer highlighted. For that, a special focus was made on the gas-liquid mass transfer occurring in Taylor flows right after the bubble formation stage in a flow-focusing microreactor (with a channel cross-section equal to 500×500 μm^2). Experiments were carried out under several flow conditions: ($95.7 < Re < 226.1$; $0.0043 < Ca < 0.010$; $0.4 < We < 2.3$; $Bo = 0.044$) and bubble size ($2.34 < L_b/l < 5.59$). Thanks to colorimetric technique, the order of magnitude of the liquid-side mass transfer coefficients k_L were obtained at the moment right after the bubble is detaching from the gas film near the cross-junction of the microreactor. The mass transfer amount fraction ϕ, which was defined by the ratio between the amount of transferred O_2 in the liquid slug right after the pinch-off and for the complete unit cell flowing at a static location equal to 14 times the channel width, was quantified. The results showed that the contribution of mass transfer right after the bubble formation stage was reasonably larger to those obtained at the bubble flowing-stage.

This chapter has been published as Yang L., Dietrich N., Loubière K., Gourdon C., Hébrard G. (2016b), *Visualization and characterization of gas–liquid mass transfer around a Taylor bubble right after the formation stage in microreactors.* ***Chem. Eng. Sci.*** 143, 364–368. Doi:10.1016/j.ces.2016.01.013.

Introduction

In recent years, gas-liquid flows in micro- and milli-channels have been the subject of an extensive literature (Garstecki et al., 2006; Dietrich et al., 2008; Pohorecki et al., 2008; Sobieszuk and Pohorecki, 2010; Zhao et al., 2010; Kashid et al., 2011; Roudet et al., 2011; Wang et al., 2013; Pan et al., 2014; Zhu et al., 2014; Kastens et al., 2015). Most of these works are devoted to the understanding and modelling of the hydrodynamics associated with the Taylor flows, as this kind of flow enables to achieve the best gas-liquid mass transfer rates required for implementing gas-liquid reactions. When investigated, the gas-liquid mass transfer characteristics are globally measured, namely by analyzing the solute concentration of samples collected at the outlet of microreactors. Such a method might lead to an inaccurate characterization, the sample collection and phase separation times being not usually taken into account. Few studies have also studied the separate contribution to mass transfer of the three characteristic stages, which are the bubble formation, the bubble flowing and the phase separation ones. Herein, it is necessary to propose online direct and local approach to overcome these limitations and to isolate the contribution of the different stages. In this perspective, Tan et al. (2012) and Yang et al. (2014) have recently developed in situ methods, based on the time-dependent variations of the bubble sizes, to investigate the mass transfer of bubbly flows in T-junction and/or co-flowing microchannels. These authors have demonstrated that the mass transfer during the formation stage contributes significantly to the overall transferred solute, in particular with respect to the associated short residence times. At present, there exists no report dealing with the direct visualization of mass transfer at microscale and just after the bubble pinch-off. The present study aims at applying the colorimetric technique to visualize and quantify the gas-liquid mass transfer occurring right after the bubble formation stage in a flow-focusing microchannel.

Section 3.1 will present the material and methods used.

Section 3.2 will be devoted to the investigation of the contribution of bubble formation stage to the overall gas-liquid mass transfer. The mass transfer process in the liquid slug right after the pinch-off will be first described. The mass transfer amount fraction ϕ, defined by the ratio

between the amount of transferred O_2 in the liquid slug right after the pinch-off and for the complete unit cell flowing at a static location equal to 14 times the channel width, will be introduced to quantify the contribution of the formation stage to the overall mass transfer.

An extended study (not published yet) will be presented in section 3.3, which proposes a critical time for the gas-liquid mass transfer after the bubble formation stage.

3.1 Materials and methods

3.1.1 Compositions of the dye solution

To make possible the visualization of the colored field, an optimal composition of the catalyzer was determined, taking into account the balance between the oxidation and reduction kinetics, and also the requirements in terms of adequate color intensity levels. This led to potassium hydroxide and glucose solutions both diluted at $30 g \cdot L^{-1}$ in deionized water (the conductivity of the deionized water is $51.2\ \mu S \cdot m^{-1}$), and to a concentration of resazurin C_{Bb} fixed at $1 g \cdot L^{-1}$ (σ_L = 55.6 $mN \cdot m^{-1}$, μ_L = 1.12 mPa·s, ρ_L = 1004.5 $kg \cdot m^{-3}$). The latter concentration was 10 times larger than the one used by Dietrich et al. (2013) in order to conserve the same quality of images.

3.1.2 Description of the experimental set-up

The experimental set-up consisted of a straight horizontal channel of square cross section $A = l^2$ where l = 500µm (4 times smaller than Dietrich et al. (2013)). The channel was carved in a polymethyl methacrylate (PMMA) plate (5mm thick) and roofed over in a watertight manner by another plate (5mm thick). The geometry of the channel is presented in **Fig. 3-1**.

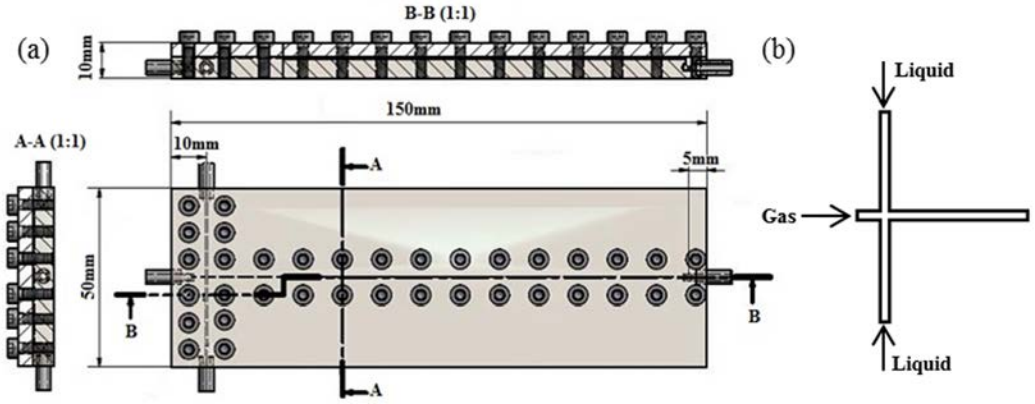

Fig. 3-1 (a) Geometry of the microchannel (Cross section: $A = l^2$, where l = 500μm).

(b) Schematic representation of the cross-junction.

Gas (air) and liquid phases (solution with dye, glucose and potassium hydroxide, flushed by nitrogen before the inlet of the channel) were both delivered from a 60 mL syringe in a syringe pump (Harvard Apparatus, PHD 22/2000, USA). Gas flow rates ranged from 0.6 to 1.2 mL min^{-1} and liquid flow rates from 2.4 to 4.0 mL min^{-1} in order to obtain a Taylor flow regime. The associated superficial gas j_G and liquid velocities j_L were: 0.040 m $s^{-1} \leq j_G = Q_G / l^2 \leq$ 0.080 m s^{-1} and 0.160 m $s^{-1} \leq j_L = Q_L / l^2 \leq$ 0.267 m s^{-1}. All of the experiments were conducted at a room temperature of 293K and atmospheric pressure.

3.1.3 Characterization of gas-liquid hydrodynamics and mass transfer

The shadowgraph method was applied to investigate the gas-liquid hydrodynamics and mass transfer inside the microchannel. The channel was lighted by a LitePad HO LED backlight (Rosco®) and the images were recorded by a monochromatic high-speed camera (Photron SA3) at 4000 frames per second. Image resolution was 10μm per pixel and the region of interest 10×1.5 mm^2. The software ImageJ (version 1.38e, National Institute of Health, USA) was used to analyze the recorded images. The following hydrodynamic characteristic parameters were measured: bubble length L_B, bubble velocity U_B, and the length of the unit cell L_{UC}.

The transfer of oxygen from air bubbles into resazurin solution was investigated over the range of gas and liquid flow rates defined in section 3.1.2, which covered only the Taylor flow regime ($95.7 < Re < 226.1, 0.0043 < Ca < 0.010, 0.4 < We < 2.3, Bo = 0.044$). As the camera was monochromatic, the different levels of pink coloration taken by the dye solution, which depended only on the quantity of oxygen transferred, were represented by 255 grey levels on the acquired images.

The gas-liquid mass transfer characteristics were determined by an image post treatment algorithm implemented on the software Matlab (R2011b), as the one used by Dietrich et al. (2013). It consisted of two steps: (i) the determination of the calibration curve, and (ii) the image processing which enabled to transform the acquired grey-level images into the equivalent oxygen concentration fields. The details of the image processing is reported in **Appendix A**. Note that the term "equivalent" is used as in reality the oxygen concentration is null as consumed by the instantaneous oxidation reaction. For the calibration process, different concentrations of resazurin solution were prepared: 0, 0.35g L^{-1}, 0.75g L^{-1} and 1g L^{-1}. The obtained calibration curve, depicted in **Fig. 3-2** (a), shows that the linearity between the grey levels and the equivalent quantities of oxygen transferred per unit of liquid volume is conserved even if the employed concentration of resazurin is significantly increased.

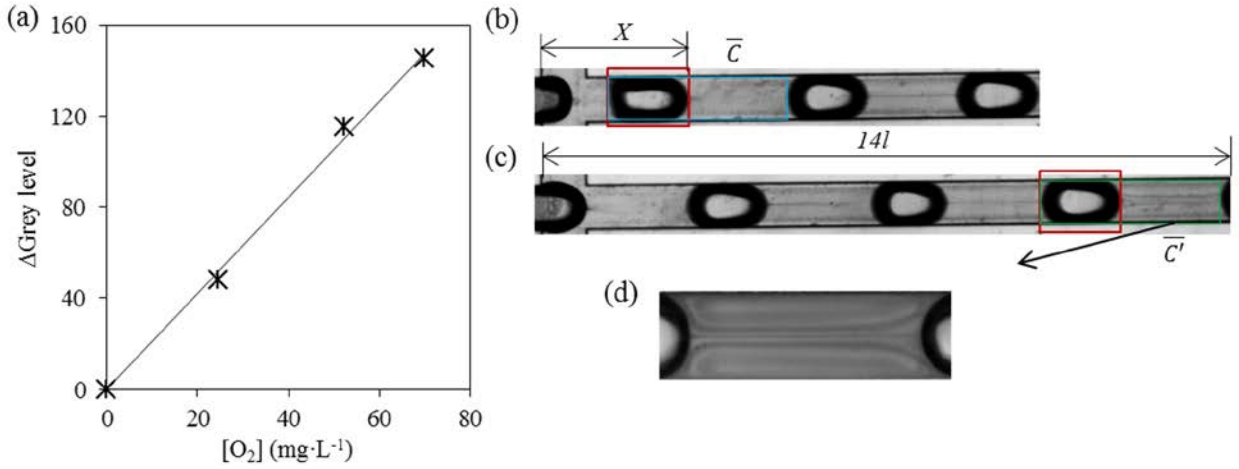

Fig. 3-2 (a) Calibration curve between grey levels and equivalent quantities of oxygen transferred per unit of liquid volume. (b) Illustration of the bubble right after pinch-off. $\overline{C}$: average equivalent oxygen concentration in the liquid slug of the unit cell at this location (the blue rectangle); *X*: axial position of the bubble, *X*=0: the two phases enter in contact. (c) Illustration of the complete unit cell bubble flowing within a distance equal to 14 times the channel width from the junction. $\overline{C}'$: average equivalent oxygen concentration in the liquid slug of the unit cell at this location (the green rectangle). The bubbles in the red rectangle represent the bubble observed. (d) Magnification observation of the mass transfer in the liquid slug.

In this study, a focus was made on the gas-liquid mass transfer occurring right after the bubble formation stage, namely at the moment right after the pinch-off stage (see **Fig. 3-2**. b). Based on an oxygen mass balance on the liquid slug and considering a plug-flow model (see Chapter 1, section 1.2.2), it can be written (Roudet et al., 2011):

$$\varphi_{O_2}(X) = j_L \cdot \frac{d\overline{C}}{dX} = k_L \cdot a \cdot [C^* - \overline{C}(X)] \qquad \text{(Eq. 3-1)}$$

In the present case, the concentration of oxygen, $\overline{C}(X)$ is null as fully consumed by the reaction in reality (Dietrich et al., 2013a), leading to:

$$k_L = \frac{\overline{C} \cdot j_L}{X \cdot a \cdot C^*} \quad \text{(Eq. 3-2)}$$

where a is the interfacial area between gas and liquid phases, C^* the dissolved oxygen concentration at saturation (8.15 mg L^{-1}), X the axial location corresponding to the bubble pinch-off (see **Fig. 3-2**. b), k_L the liquid-side mass transfer coefficient, and $\overline{C}$ the average equivalent oxygen concentration in the liquid slug of the unit cell at this location, deduced from image processing. It is important to notice that the equivalent oxygen concentration field obtained at a given location (x,y) is a mean value along the z-axis (Dietrich et al., 2013a). This is a limitation of the present method: it does not enable to discriminate the equivalent oxygen concentration fields related to each xy-plane along the channel height. Meanwhile, as visualization of the bubble areas of the nose and rear due to the hemispheric shape is also not available, this liquid volume linked to these bubble areas cannot be taken into account for the calculation, this could lead to a maximum error of 18% on the volume estimation of liquid phase in a unit cell. An identical calculation was made for the complete unit cell flowing at a static axial location equal to 14 times the channel width from the junction corresponding to a bubble-flowing condition, by using $\overline{C}'$ instead of $\overline{C}$ (see **Fig. 3-2**. c).

The interfacial area a was calculated by assuming a hemispherical shape for the bubble nose and rear, and a cylindrical shape for the bubble body, as below:

$$a = a_r + a_f = \frac{2 \cdot (\pi \cdot l^2 / 2)}{L_{UC} \cdot l^2} + \frac{\pi \cdot l \cdot (L_B - l)}{L_{UC} \cdot l^2} = \frac{\pi}{L_{UC}} + \frac{\pi \cdot (L_B - l)}{L_{UC} \cdot l} \quad \text{(Eq. 3-3)}$$

where a_r and a_f represent the specific interfacial area for the liquid film and the recirculating region, respectively. Typically, a ranged from 3734 m^{-1} to 4884 m^{-1} in the operating domain investigated.

3.2 Results and discussion

The measured values of the length of the bubble L_B, the length of the liquid slug L_{slug}, the interfacial area a are listed in **Table 3-1**. As in Roudet et al., (2011), a correlation relating L_B/l to j_G/j_L has been found to be well adapted (mean relative deviation of 12.5%), leading to:

$$\frac{L_B}{l} = 2.20 + 5.57 \cdot \left(\frac{j_G}{j_L}\right) \qquad \text{(Eq. 3-4)}$$

Fig. 3-3 (a) presents a typical image sequence obtained just after the moment where both gas and liquid phases were injected in the microchannel. It thus corresponds to the transient period during which the Taylor flow has not yet reached the steady-state regime. **Fig. 3-3** (b) reports, for the same superficial velocities, the image sequence obtained when the flow is steady. The comparison of both sequences revealed that for the first bubble entering in the microchannel, the equivalent oxygen concentration fields are clearer than when steady state was reached, and that oxygen almost accumulates in the front of the bubble. This can be explained by the fact that for the first bubble, no recirculation exists in the liquid phase.

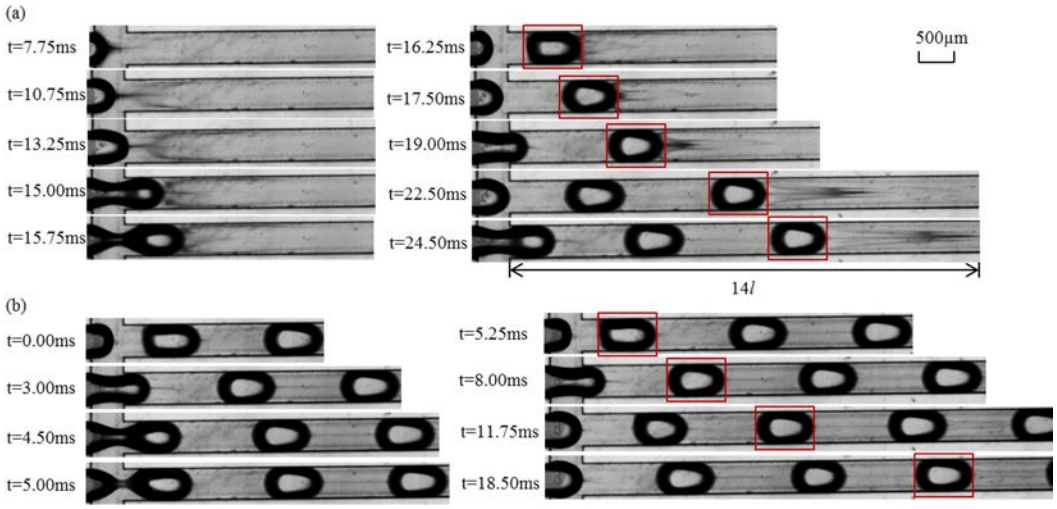

Fig. 3-3 Typical images of the mass transfer process (j_G= 0.053 m·s^{-1}, j_L= 0.27 m·s^{-1}). (a) just after the moment where both gas and liquid phases are injected in the microchannel (transient period). (b) when steady state is reached. The bubble in the red rectangle represents the bubble observed.

The variation of liquid-side mass transfer coefficient k_L, obtained right after the bubble pinch-off (Eq. 3-2 with $\overline{C}$) is plotted as a function of the two-phase superficial velocity j at different gas superficial velocities j_G in **Fig. 3-4**. It can be observed that: (1) j has a positive effect on k_L, and at a fixed j, namely, k_L increases as j_L increases; (2) as the gas superficial increases, k_L increases. In addition, from **Table 3-1**, it demonstrates that for a fixed j_L, k_L increases as j_G increases. This phenomena is contrary to what observed by Dietrich et al. (2013), during the bubble flowing-stage, but agrees with the results of Tan et al. (2012) and Yang et al. (2014) obtained during the bubble formation stage. It could be explained by the fact that, due to the dynamic process of the bubble formation, the liquid films around the bubble is quickly renewed. In this case, the liquid-side mass transfer resistance becomes negligible when compared to the gas side resistance. Consequently, an increase of the gas flow rate improves the mixing (circulating flow) inside the forming bubble and thus the surface renewal in the bubble and the mass transfer.

It is important to note that, considering the latter values of k_L, the concentration C_{Bb} equals to 1 $g \cdot L^{-1}$, and the reaction constant k_2 determined in Chapter 2, the Hatta number Ha can be calculated by (Eq. 2-9). One obtains Ha ranging from 1.05 to 3.08. According to Chapter 2, section 2.5, it can be known that the colorimetric reaction is in this case moderately rapid ($0.3 < Ha < 3$), and that the enhancement factor E needs numerical simulations to be calculated. Thus, the measured mass transfer coefficients k_L correspond in reality to values that are uncorrected by E: they are not the intrinsic ones, but thus just give the order of magnitude of the liquid side mass transfer coefficient right after the bubble pinch-off.

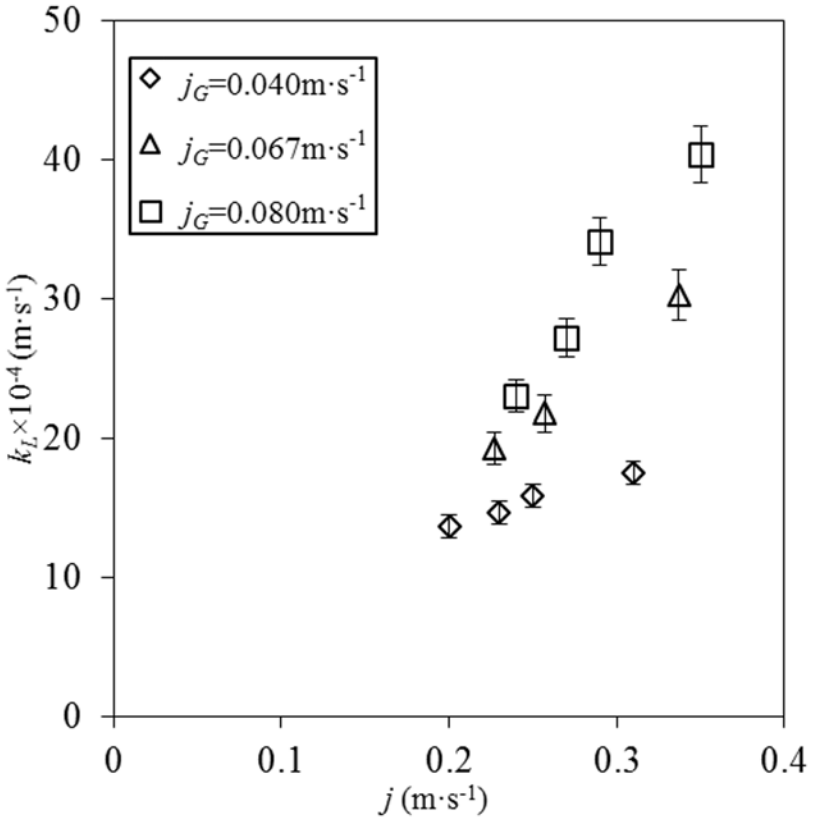

Fig. 3-4 Liquid side mass transfer coefficient k_L versus the two-phase superficial velocity ($j = j_G + j_L$) at different gas superficial velocities.

In order to quantify the contribution of bubble formation stage to the overall mass transfer, the mass amount fraction, ϕ, defined by Tan et al (2012), is used.

From image processing, the mass amount of transferred oxygen in the liquid slug can be calculated by pixel-by-pixel accumulation in the liquid slug right after the bubble pinch-off (m_{O_2}) and for the complete unit cell flowing at a static location equal to 14 times the channel width from the junction where the two phases began to contact (m_{O_2}') (see **Fig. 3-2**). From these two values, the mass transfer amount fraction, ϕ, can be defined according to:

$$\phi = m_{O_2} / m_{O_2}' \qquad \text{(Eq. 3-5)}$$

Fig. 3-5 reports the variation of this fraction as a function of the gas superficial velocity j_G for different liquid superficial velocities. It can be seen that, at a given j_G, ϕ slightly increases when rising j_L, and for a given j_L, ϕ seems to globally increase as j_G increases. ϕ is in a range of 45% to 90% under the experimental conditions, which is larger than that (30-40%) in Tan et al., (2012). The explanation could be that both the gas-liquid flow rates are greater in this case, which can intensify the mass transfer during the formation stage, and thus the contribution of the formation stage to the total mass transfer.

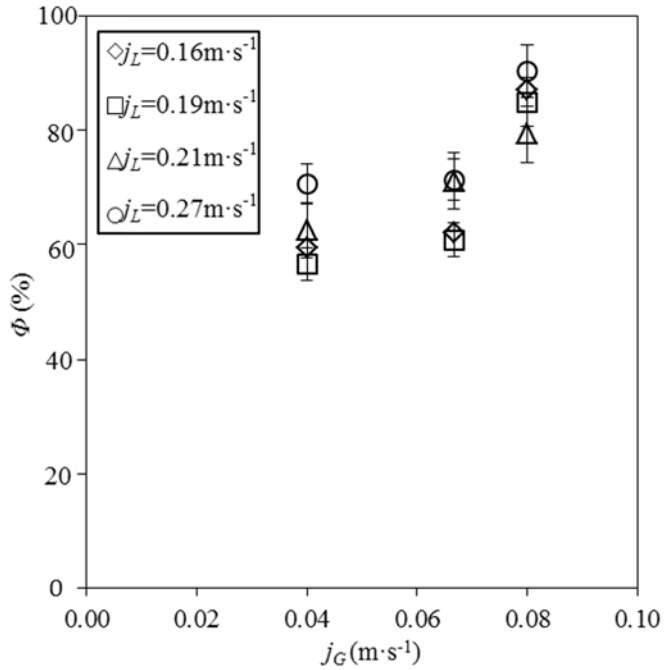

Fig. 3-5 Variation of the mass transfer amount fraction Φ as a function of the gas superficial velocity at different liquid superficial velocities.

To quantify the enhancement induced by the recirculation in the gas bubble, the so-called "enhancement factor" E_{Bf} defined by Tan et al. (2012) was calculated according to:

$$E_{Bf} = \frac{k_L}{k_{L,diff}} \qquad \text{(Eq. 3-6)}$$

$$k_{L,diff} = 2 \cdot \sqrt{\frac{D_{O_2}}{\pi \cdot t}} \qquad \text{(Eq. 3-7)}$$

where $k_{L,diff}$ is the liquid-side mass transfer coefficient right after the bubble pinch-off defined considering the Higbie penetration model (Higbie, 1935), D_{O_2} the oxygen diffusion coefficient (equal here to 3.2×10^{-9} m^2 s^{-1}), t the bubble formation time (ranged from 4.75 to 10.50 ms). The obtained E_{Bf} varies from 2 to 8 and is smaller than that the values of Tan et al. (2012) varying between 5 and 15. Such a difference is linked due to the fact that diffusion coefficient of CO_2 in NaOH solution in their case is greater than the one here involved, and also that the bubble formation times are larger (200-400 ms against 4.75-10.50 ms).

At last, **Table 3-1** displays a comparison of experimental volumetric mass transfer coefficients (uncorrected by E) and liquid-side mass transfer coefficients at two locations, right after the pinch-off and for the complete unit cell flowing at a static location equals to 14 times the channel width from the junction. It illustrates that both the values of k_La and k_L are significantly larger right after the bubble formation (increase by 28-64% for k_La and by 28-65% for k_L). This confirms that the contribution of the mass transfer of the formation stage to the overall mass transfer is reasonably large when compared to the relatively short bubble formation times involved.

Table 3-1 Comparison of volumetric liquid-side mass transfer coefficient k_La and liquid-side mass transfer coefficient k_L at two positions, right after the pinch-off and for the complete unit cell flowing at a static location equal to 14 times the channel width from the junction. The superscript " ' " notes the value for the latter situations.

j_G ($m \cdot s^{-1}$)	j_L ($m \cdot s^{-1}$)	L_{slug} (mm)	L_B (mm)	a (m^{-1})	k_La (s^{-1})	k'_La (s^{-1})	$k_L \times 10^{-4}$ ($m \cdot s^{-1}$)	$k'_L \times 10^{-4}$ ($m \cdot s^{-1}$)
0.040	0.16	0.79	2.12	4577	6.27	4.11	13.70	8.98
	0.19	0.80	2.02	4501	6.62	4.27	14.70	9.49
	0.21	1.05	1.63	3822	6.08	3.58	15.90	9.37
	0.27	0.95	1.39	3740	6.47	3.90	17.30	10.40
0.067	0.16	0.77	2.37	4736	9.14	3.87	19.30	8.16
	0.19	0.67	2.34	4884	10.65	4.23	21.80	8.67
	0.27	1.06	1.17	3301	10.00	4.47	30.30	13.50
0.080	0.16	0.67	2.79	5073	11.67	6.51	23.00	12.80
	0.19	0.71	2.42	4864	13.23	7.02	27.20	14.40
	0.21	0.77	1.91	4480	15.28	8.27	34.10	18.50
	0.27	0.73	1.51	4233	17.10	8.87	40.40	20.90

3.3 Extended study

Thanks to the colorimetric technique, it is possible to measure the amount of transferred oxygen, m_{O_2}, in the liquid slug as a function of time right after the bubble pinch-off stage. A typical example of the evolution of m_{O_2} as a function of time t, is shown in **Fig. 3-6**. (j_G = 0.040 $m \cdot s^{-1}$, j_L = 0.16 $m \cdot s^{-1}$).

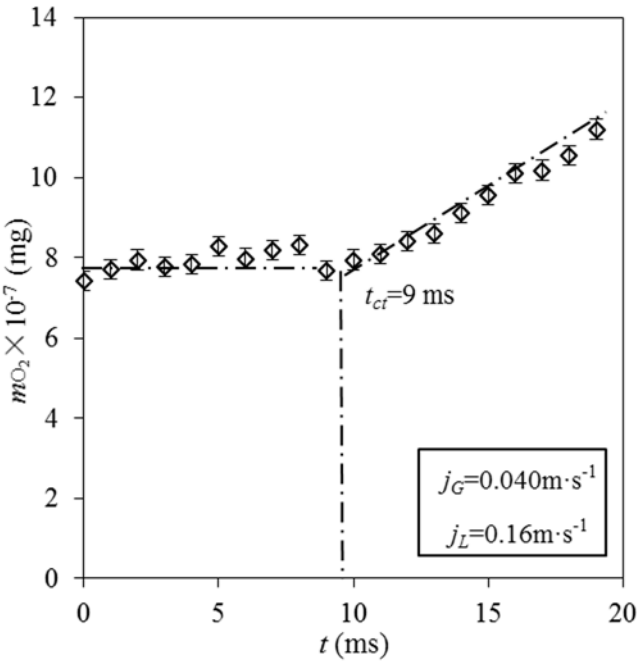

Fig. 3-6 Evolution of the mass of oxygen m_{O_2} in a unit cell as a function of time t (t=0 ms: the time of the pinch-off stage).

It can be observed that (i) m_{O_2} remains almost unchanged in the first moments right after the pinch-off, and (ii) after, there exists a turning point (named critical time t_{ct}), where m_{O_2} starts to increase with t. This phenomenon exists for all the operating conditions. **Fig. 3-7** shows the evolution of this critical time t_{ct} as a function of the ratio between gas and liquid flow rates.

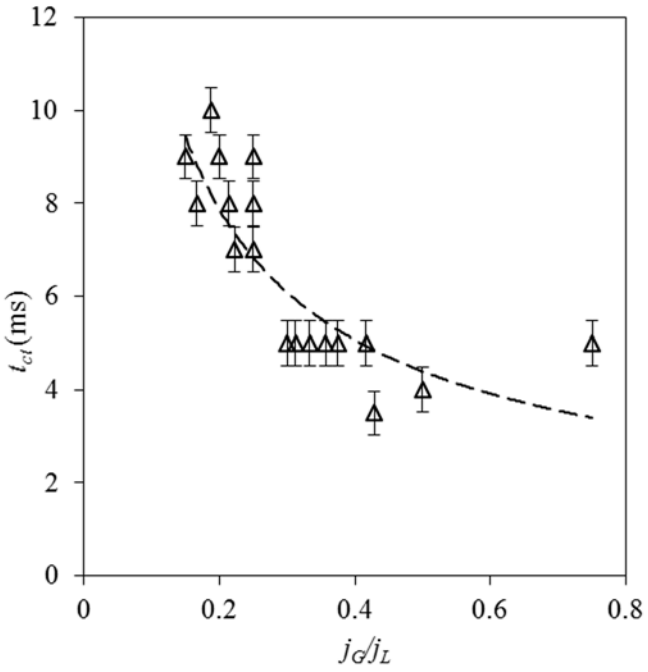

Fig. 3-7 Evolution of the critical time t_{ct} versus the ratio between the gas-liquid flow rates j_G/j_L.

From **Fig. 3-7**, one notes that, as j_G/j_L increases, t_{ct} decreases. The following empirical relationship can be proposed:

$$t_{ct} = 2.83 \cdot (\frac{j_G}{j_L})^{-0.64}, \text{mean deviation}: 14\% \qquad \text{(Eq. 3-8)}$$

Further work is required to better understand such results, in particular the mechanism of mass transfer during and right after the bubble formation stage, as well as the meaning of t_{ct} in the physical point of view.

3.4 Conclusion

The colorimetric technique was applied to visualize and characterize the gas-liquid mass transfer in a square microchannel. Compared with the previous work (Dietrich et al., 2013a), this

study demonstrated that this technique could also be applied at micro-scale. A focus was made on the local characterization of gas-liquid mass transfer at the bubble formation stage. The results obtained showed that the bubble formation stage made a reasonably large contribution (45-90% for the complete unit cell flowing at a static location equals to 14 times the channel width from the junction) to the mass transfer of overall flowing-stage when compared to the relatively short bubble formation times (4.75-10.50ms). The gas-liquid mass transfer during the formation stage was intensified by 2-8 times due to the intensification of the mixing inside the forming bubble.

All these findings give important information to understand the contributions of the bubble formation stage to the overall gas-liquid mass transfer occurring in a microchannel. In the future, these types of studies should continue because they will serve as basis for elaborating a complete model, accounting for the bubble formation stage.

CHAPTER 4

Gas-liquid mass transfer around Taylor bubbles flowing in a meandering millimetric square channel

Résumé: Dans ce chapitre, le transfert de matière gaz-liquide autour de bulles de Taylor se déplaçant dans un canal carré (2 × 2 mm^2) sinueux a été visualisé et caractérisé localement. L'évolution des champs de concentration d'oxygène équivalents entre les bulles passant par plusieurs courbures a d'abord été décrite. Il a été observé comment la structure de l'écoulement (zones de recirculation) était perturbé et divisée par les changements de direction (effet centrifuge), jusqu'à atteindre une concentration uniforme d'oxygène dans le liquide. L'influence du «virage», qui associe deux sections «droites» du canal sinueux a également été souligné: un ralentissement du transfert de masse gaz-liquide y a été clairement montré. Les coefficients de transfert de matière volumétriques ont été déterminés en ajustant les profils axiaux expérimentaux des concentrations moyennes d'oxygène (avant le virage) avec celles prédites par un modèle de type piston.

Ce chapitre a été publié dans l'article suivant : Yang L., Loubière K., Dietrich N., Le Men. C., Gourdon C., Hébrard G. (2017b), *Local investigations on the gas-liquid mass transfer around Taylor bubbles flowing in a meandering millimetric square channel*. ***Chem. Eng. Sci.*** 165, 192–203. doi:10.1016/j.ces.2017.03.007.

Abstract: In this chapter, gas-liquid mass transfer around Taylor bubbles flowing in a meandering millimetric square channel (channel cross-section equals to 2×2 mm^2) was locally visualized and characterized. The evolution of equivalent oxygen concentration fields in the liquid slugs passing through one and several bends was firstly described. In particular, it was observed how the flow structure (recirculation zones) inside the liquid slugs were twisted and split by the periodic bends (centrifugal effect), until reaching, after several bends, a uniform O_2 concentration inside the liquid slugs. The influence of the "turning point", joining two "straight" sections of meandering channel was also highlighted: a slowing down of the gas-liquid mass transfer was clearly shown. Volumetric mass transfer coefficients were determined at last by fitting the experimental axial profiles of averaged oxygen concentrations in the liquid slugs (before the turning point) with the ones predicted by a classical plug-flow model.

This chapter has been submitted as Yang L., Loubière K., Dietrich N., Le Men. C., Gourdon C., Hébrard G. (2017b), *Local investigations on the gas-liquid mass transfer around Taylor bubbles flowing in a meandering millimetric square channel*. ***Chem. Eng. Sci.*** 165, 192–203. doi:10.1016/j.ces.2017.03.007.

Introduction

In order to combine intensified heat and mass transfers, high residence time and compactness in HEX reactors, the use of 2D-structured meandering (or tortuous or serpentine or wavy) channel structures constitutes an interesting solution. Indeed, contrary to the case in a straight channel, the occurrence of curvatures (or bends) generates flow instabilities and secondary flows (Dean vortices) in fluid motion (Dean, 1928), where mixing between the core fluid and near-wall fluid can be improved; the boundary layers are also disrupted and thinned, thus affecting positively heat and mass transfer phenomena. Most of the existing literature dealing with such type of meandering channels focus on the study of single liquid phase flows, reactive or not (Xiong and Chung, 2007; Anxionnaz-Minvielle et al, 2013; Karale et al., 2013; Dai et al., 2015). Few attention has been surprisingly paid on the implementation of gas-liquid systems in meandering channels, whereas: (i) the gas-liquid systems occupy a key place in scientific research and industrial application fields (hydrogenations, sensitized photo-oxygenations, fluorinations, biochemical reactions); (ii) there still raises many fundamental questions (coupling between transport phenomena and kinetics); (iii) studies in straight micro- or millimetric channels are the object of an abundant literature (van Baten and Krishna, 2004; Roudet et al., 2011; Yao et al., 2014; Haghnegahdar et al., 2016; Haase et al., 2016; Butler et al., 2016). In such two-phase reactive systems, the knowledge of mass transfer between gas and liquid phases is then extremely important; as managing the chemical kinetics, it can become the limiting step controlling the chemical reactions in terms of conversion and selectivity.

While the influence of the occurrence of bends in millimetric channels on the gas-liquid hydrodynamics (i.e. flow regime, mixing efficiency, interfacial area) has been highlighted by several authors (Günther et al., 2004; Fries and von Rohr, 2009; Dessimoz et al., 2010), rare are at present the studies quantifying how curvatures affect the gas-liquid mass transfer (Roudet et al., 2011; Kuhn and Jensen, 2012). Roudet et al. (2011) showed that, when compared to a straight channel of identical compactness and sectional-area, the meandering channel induced: (i) a delay in the transition from Taylor to annular-slug regimes; (ii) a rise of 10-20% in bubble lengths while conserving almost identical slug lengths; (iii) higher deformations of bubble nose and rear

due to centrifugal forces (bends). They also observed that, for the Taylor flow regime, $k_L a$ increased coherently when increasing superficial gas velocity j_g , and that the meandering geometry had a small influence. On the contrary, this effect was found no more negligible for the slug-annular flow regime. At last, they demonstrated that, at identical compactness, the meandering channel was found to be the most competitive. As these authors used a global experimental method (measurements of concentrations in dissolved oxygen along the channel length by oxygen microsensors), the full understanding of the mechanism controlling the gas-liquid mass transfer in a meandering channel could not be achieved, and in particular the contribution of the curvatures. In order to fill these gaps, local measurements, such as concentration fields of the transferred gas phase around bubbles in the liquid slugs and films, are required. However, to our best knowledge, there exists no research on the local visualization and characterization of gas-liquid mass transfer in meandering channels.

With regard to this context, this chapter aims at locally studying the mass transfer around Taylor bubbles flowing in a meandering millimetric square channel, identical in elementary shape to the one used by Roudet et al. (2011) but longer. For this purpose, the colorimetric technique proposed by Dietrich et al. (2013) has been used (resazurin, see section 1.3). In comparison with PLIF technique (e.g. Butler et al., 2016), the colorimetric method is more convenient and user friendly as it does not need any laser excitation or inserting a physical sensor.

This chapter will be structured as follows.

Section 4.1 will present the material and methods used.

Results will be presented in section 4.2. The hydrodynamics of gas-liquid system (air/reactive medium) will be firstly characterized, in particular in terms of the gas-liquid flow map, overall gas hold-up, bubble length, shape and velocity. The colorimetric technique will be implemented in a second time, only in the case of the Taylor regime. The fields of equivalent oxygen concentration in the liquid slugs will be presented and discussed, as well as their changes according to the locations in the bend and all along the channel length; the influence of gas and liquid flow rates on these fields will be also outlined. From them, the evolution of averaged O_2 concentration with the axial location in the channel will be determined, enabling the overall

volumetric mass transfer coefficients to be deduced using the classical plug-flow model. At last, these data will make possible the calculation of liquid-side mass transfer coefficients, based on an accurate determination of interfacial areas.

4.1 Materials and methods

4.1.1 Compositions of the dye solution

In this chapter, sodium hydroxide and glucose solutions are both diluted at 20 $g \cdot L^{-1}$ in deionized water, and a concentration of resazurin was fixed at 0.1 $g \cdot L^{-1}$.

4.1.2 Fluid properties

All the experiments were performed at 293.15 K and atmospheric pressure. For the hydrodynamic experiments, the liquid phase was dye-free, composed only of D-glucose anhydrous (Fischer Scientific®, CAS 50-99-7) and sodium hydroxide (VWR®, CAS 1310-73-2), both diluted at 20 $g \cdot L^{-1}$ in deionized water (conductivity: 51.2 $\mu S \cdot m^{-1}$). For the mass transfer experiments, the concentration of resazurin was fixed at 0.1 $g \cdot L^{-1}$, was added to the previous solution. All the physico-chemical properties are reported in **Table 4-1**.

Table 4-1 Physio-chemical properties of the liquid phases at 293.15K.

Liquid phase	C ($g \cdot L^{-1}$)	σ_L ($mN \cdot m^{-1}$)	μ_L (mPa·s)	ρ_L ($kg \cdot m^{-3}$)
Deionized water	0	71.4	1.003	996.8
Aqueous solution of glucose anhydrous and sodium hydroxide	20 20	76	1.118	1004.5
Aqueous solution of glucose anhydrous sodium hydroxide and resazurin	20 20 0.1	75	1.118	1004.5

4.1.3 Description of the experimental set-up

The experimental set-up was depicted in **Fig. 4-1** (a). It consisted of a meandering channel composed of a series of elementary units, named bends (**Fig. 4-1**. b). The channel, horizontally placed, had a square cross section $A = l^2$ where $l = 2$ mm, and the elementary bend, which geometry was identical to the one used in Roudet et al. (2011), was characterized by a radius of curvature r_c of 1.5 mm and a straight length between two bends of 6.94 mm (see **Fig. 4-1**. c). Every about 15 bends, there was a big bend, named "turning point", enabling to connect the two "straight" channel sections, which leads to change the flow direction in 180º and in order to have a long channel (the total developed straight length of the meandering channel $L = 1.37$ m), while keeping a compact device. The channel was carved in a PolyMethyl MethAcrylate (PMMA) plate (3 cm thick), and roofed over in a watertight manner by another plate (3 cm thick). The gas phase (air) was injected via a hole of diameter 1.6 mm, pierced perpendicularly to the channel (T-junction); the gas injection was spaced from about eight bends from the liquid one to enable the liquid flow to be stable (**Fig. 4-1**. b). Gas (air) was delivered from the supply pipeline regulated by a mass flow controller (Brooks® model 5850E). Before entering in the main channel, the gas flowed through a winding of a 2 m long capillary of 750 µm internal diameter, aiming to increase the pressure drop in order to create a stable gas injection in the liquid flow. Liquid phase was pumped by a Cantoni® jet pump with the flow rate regulated by a mass flow control system (Micro motion®). The volumetric gas flow Q_G rates ranged from 0.2 to 9 L·h^{-1} and liquid flow rates Q_L from 1 to 2 L·h^{-1}. The corresponding superficial gas velocities j_G and liquid velocities j_L were: 0.014 m·s^{-1} $\leq j_G = Q_G / l^2 \leq$ 0.625 m·s^{-1} and 0.069 m·s^{-1} $\leq j_L = Q_L / l^2 \leq$ 0.139 m·s^{-1}.

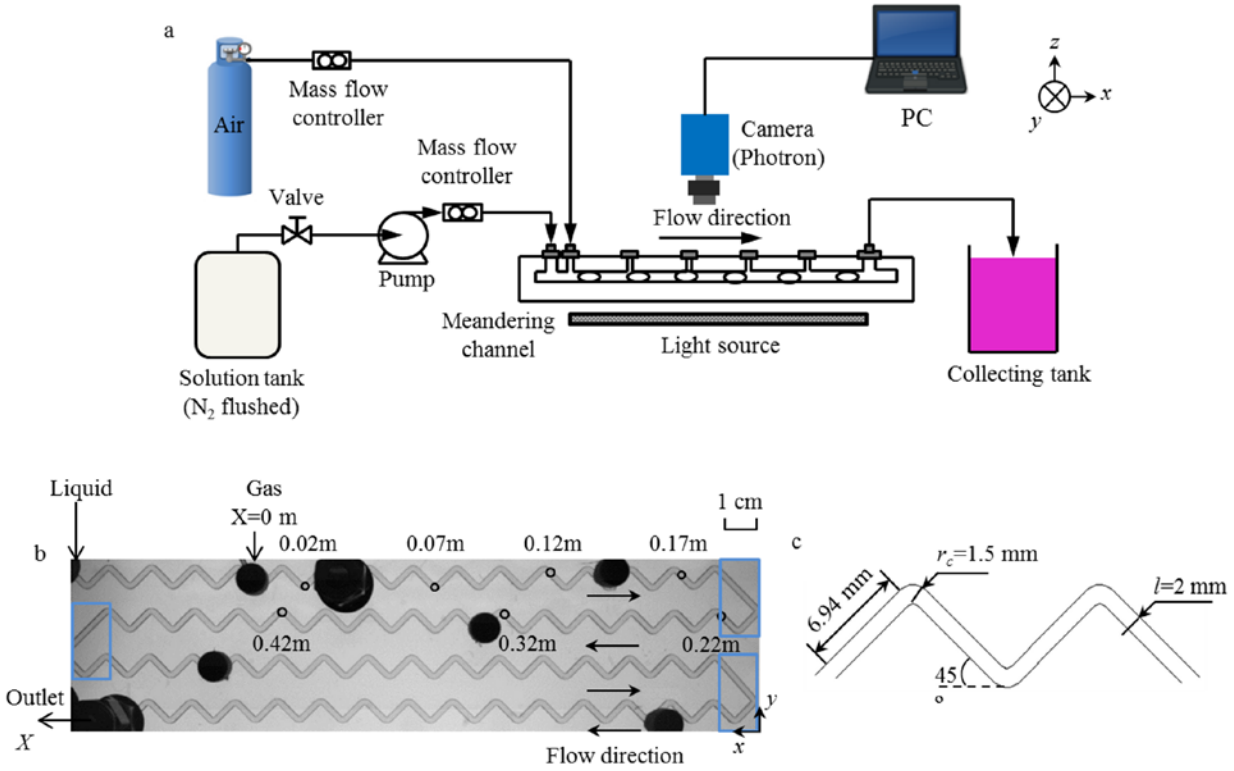

Fig. 4-1 (a) Schematic diagram of the experimental set-up. (b) Picture of the meandering channel in the horizontal *xy*-plan defined in (a). *X* corresponds to the location (curvilinear coordinate) in the channel from the gas inlet. $X = 0$ is the location where the two phases enter in contact. The channel has a cross-sectional area $A = 2\times2$ mm^2, and a total developed straight length L of 1.37 m. Black circles represent the axial positions where the equivalent oxygen concentration fields were measured. The sections of the channel corresponding to the so-called "turning points" are outlined by blue rectangles. The arrows indicate the flow direction. (c) Schematic of elementary units (bends) of the meandering channel.

4.1.4 Image acquisition system

The shadowgraph method was applied to investigate the gas-liquid hydrodynamics and mass transfer inside the meandering channel. The channel was lighted by a LitePad HO LED backlight (Rosco®) and the images of the bubbles flowing along the channel were recorded by a monochromatic high-speed CMOS (Complementary Metal Oxide Semiconductor) camera (Photron® SA3) at 2000 frames per second. Image resolutions were 164 µm per pixel and 20 µm

per pixel for the hydrodynamics and mass transfer experiments, respectively. The regions of interest were 168.1×84.2 mm^2 and 20.1×20.1 mm^2, respectively. For the mass transfer experiments, the gas-liquid flow was observed at 7 different axial distances X from the gas injection, namely: X = 0.02 m, 0.07 m, 0.12 m, 0.17 m, 0.22 m, 0.32 m and 0.42 m, as depicted in **Fig. 4-1** (b).

4.1.5 Image processing

4.1.5.1 Hydrodynamics of the gas-liquid flow

A typical raw image of the gas-liquid flow all along the channel length (1.37 m) is shown in **Fig. 4-2** (a). In order to extract the hydrodynamics parameters (gas hold-up, bubble length and velocity, liquid slug length etc.) from the raw image, a background image when the channel was filled with the liquid phase was needed, shown in **Fig. 4-2** (b). Then, an image post-treatment algorithm was implemented on the software Matlab (R2015a). In this algorithm, the background division approach was used to eliminate the effect of the background, instead of the traditional method consisting in subtracting to background image to each image; this was found to be more suitable to avoid illumination fluctuations and to diminish the confusion between background and foreground in pixels (Izquierdo-Guerra and García-Reyes, 2010). The image processing made possible the accurate detection of all the bubbles and liquid slugs inside the channel, as displayed in **Fig. 4-2** (c) and (d) respectively, as below:

- For the gas bubbles image (**Fig. 4-2** c), it was generated by the segmentation methods in image processing and analysis in Matlab. Namely, after dividing the raw image (**Fig. 4-2** a) with the background image when the channel was filled with the liquid phase (**Fig. 4-2** b), one could obtain the image where only the bubbles left (not shown in the manuscript). Then the image segmentation methods were implemented to identify all the bubbles on the image (**Fig. 4-2** c).

- For the liquid slugs image (**Fig. 4-2** d), it was generated by subtracting the image where only the channel left on the image with **Fig. 4-2** (c). The image where only the channel left on the image was obtained by dividing the background image when the channel was filled with the air phase (not shown here), with the one filled with the liquid phase (**Fig. 4-2** b).

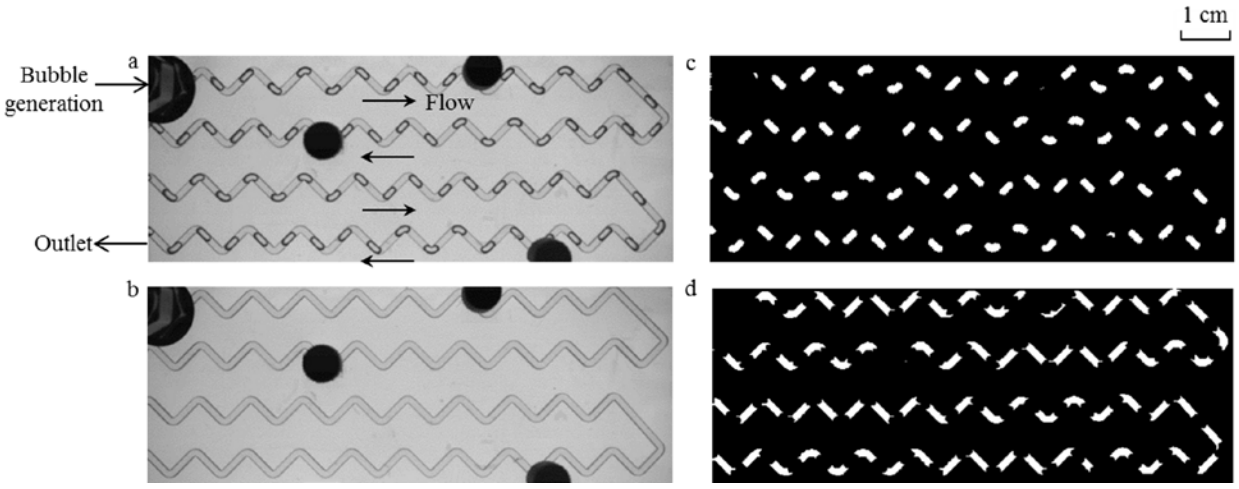

Fig. 4-2 Sequence of image processing. (a) Typical raw image of gas-liquid flows. (b) Raw image of the channel filled with liquid phase. (c) Detection of the bubbles (binary image). (d) Detection of the liquid slugs (binary image). Operating condition: j_L = 0.139 m·s^{-1}, j_G = 0.069 m·s^{-1}.

Once detected, the areas of the channel in the *xy*-plane (noted as A_C), all the 2D bubbles (A_B) and all the 2D liquid slugs (A_S) appearing along the whole length of the channel, could be obtained from the final binary images. Thus, the gas hold-up could be calculated as according to:

$$\varepsilon = \frac{A_B}{A_C} = \frac{A_B}{l \times L} = \frac{\sum A_{B,i}}{l \times L} \qquad \text{(Eq. 4-1)}$$

where i = 1…N, N is the number of bubbles/liquid slugs. It was observed that the difference between the summation of the bubble areas and liquid slug areas ($\sum A_{B,i} + \sum A_{s,i}$) and the channel area A_C is smaller than 2%, which could be attributed due to the area occupied by the liquid film.

Bubble characteristics (i.e. bubble length L_B, liquid slug length L_S, and bubble velocity U_B) were determined only in Taylor flow regime. The lengths of bubble and of liquid slug (noted L_B and L_S respectively, illustrated in **Fig. 4-3**. a) were extracted from the major axis length of the

bubbles which was an automatic procedure based on a pre-defined function. The averaged values of L_B and L_S were calculated by considering 20 bubbles on one image and 20 images were used. The bubble velocity U_B was deduced from the averaged times required by bubbles to flow along two bend periods. For a given operation condition, the standard deviations of the bubble characteristics (L_B, L_S and U_B) of all the bubbles inside the channel were smaller than 6% of the averaged value.

4.1.5.2 Gas-liquid mass transfer

The gas-liquid mass transfer characteristics were determined by using the same image post-treatment algorithm (implemented on the software Matlab R2015a) than the one used by Dietrich et al. (2013). It consisted of two main steps: (i) the determination of the calibration curve, and (ii) the image processing which enabled to transform pixel-by-pixel the acquired grey-level images into the equivalent oxygen concentration fields.

For the calibration process, different concentrations of resazurin solution were prepared: 0, 0.025 $g \cdot L^{-1}$, 0.05 $g \cdot L^{-1}$, 0.075 $g \cdot L^{-1}$ and 0.1 $g \cdot L^{-1}$. An example of calibration curve (at X = 0.02 m) is depicted in **Fig. 4-3** (b), showing the linearity between the grey levels and the equivalent amounts of oxygen transferred per unit of liquid volume. It is important to mention that the calibration process was re-implemented each time when the observation position (camera, light source, reactor) was changed. After applying the calibration curve in the image processing, the equivalent concentration field of oxygen could be obtained, and the oxygen transferred in the liquid slugs could be directly visualized, depicted in **Fig. 4-3** (c). Note that under the milli- scale conditions investigated, any oxygen concentration could not be unfortunately measured in the liquid film zone close to the walls.

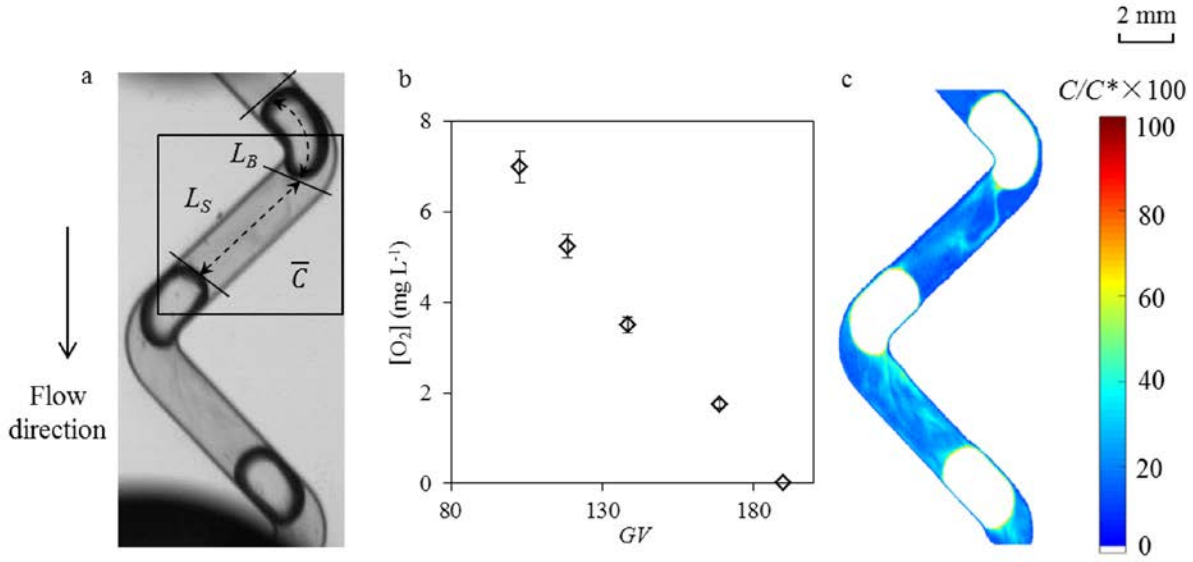

Fig. 4-3 Gas-liquid mass transfer experiments: (a) Typical raw image, where $\overline{C}$ corresponds to the averaged equivalent oxygen concentration in the liquid slug, and at this axial location in the meandering channel, $\overline{C}$ measured refers to the black rectangle. (b) Calibration curve between grey levels and equivalent amounts of oxygen transferred per unit of liquid volume. (c) Equivalent oxygen concentration field, $C(x, y)$, obtained after applying image processing and the calibration curve. Operating condition: j_L = 0.139 m·s^{-1}, j_G = 0.069 m·s^{-1}, flowing distance X = 0.02 m (close to the gas injection).

4.2 Results and discussion

4.2.1 Gas-liquid hydrodynamics

4.2.1.1 Flow regimes, overall gas hold-up and bubble velocity

Depending on the gas and liquid flow rates, different spatial distributions of the two phases were observed and various flow regimes were distinguished. The cartography of the gas-liquid flow regimes is displayed in **Fig. 4-4**. Under the present operating conditions (0.014 m·s^{-1} ≤ j_G ≤ 0.625 m·s^{-1}; 0.069 m·s^{-1} ≤ j_L ≤ 0.139 m·s^{-1}), three regimes can be identified for the meandering channel:

– The Taylor flow regime occurs at low and moderate gas flow rates, for which the lengths

of bubbles and liquid slugs are constant along the meandering channel and regularly spaced. By visualization, one can observe that (i) the bubble length L_B increases as the gas flow rate increases under a given liquid flow rate; (ii) L_B decreases as the liquid flow rate increases under a given gas flow rate; (iii) the liquid slug length (separating two consecutive bubbles) significantly decreases as gas flow rate increases, whereas it slightly varies as liquid flow rate changes under a given gas flow rate.

- The second regime, called slug-annular flow regime, occurs at relatively high gas flow rates. Unstable slug flows appear, characterized by the occurrence of long bubbles. Two consecutive bubbles can be so close to each other that gas-liquid flow exhibits significant randomness. The rupture of an extremely long bubble could be seen under some conditions.
- The last regime is the annular flow and occurs at high gas flow rates. A continuous gas core in the channel center seems to be formed.

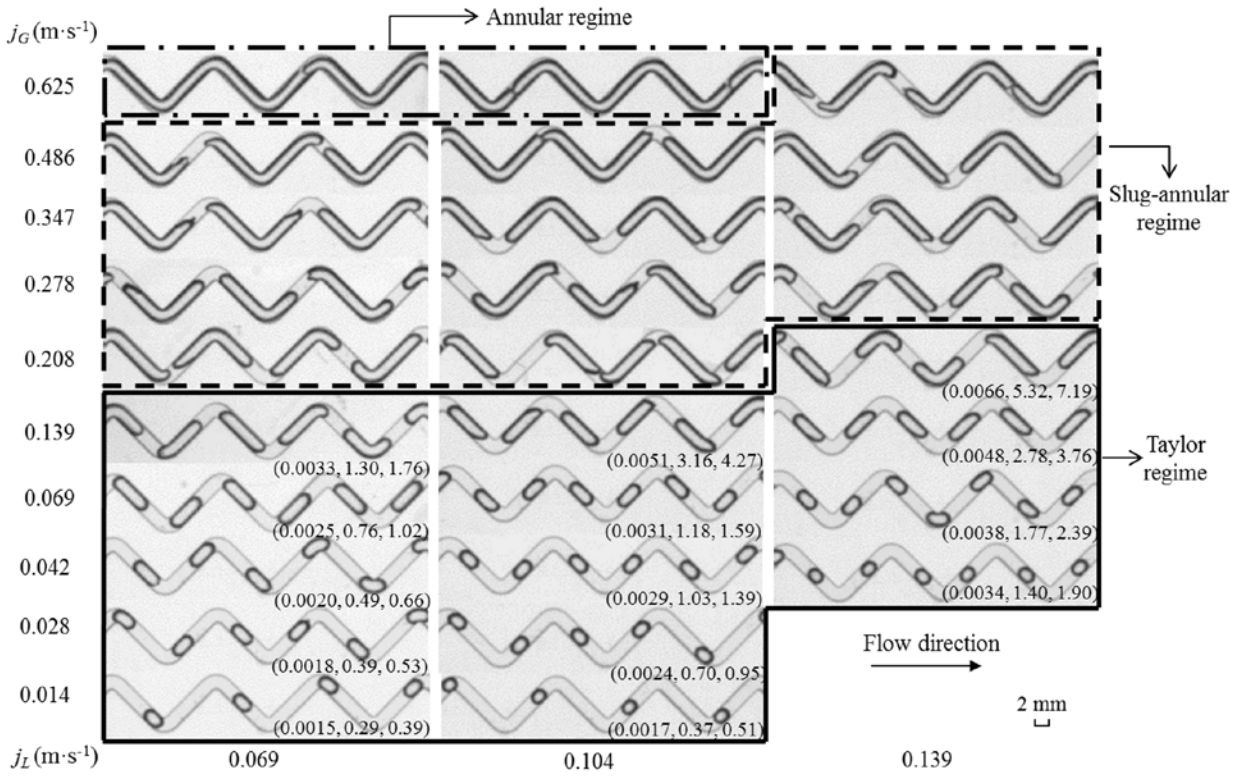

Fig. 4-4 Cartography of gas-liquid flow regimes. The flow regimes in the frame with solid lines correspond to the Taylor regime, with dashed lines the slug-annular regime, and with dash dotted lines the annular regime. The numbers in the brackets correspond to (*Ca*, *We*, *Ce*).

The evolution of gas hold-up ε (measured over the whole length of the channel, see (Eq. 4-1)) is plotted in **Fig. 4-5** (a) as a function of the volumetric quality (fraction) of gas $\beta = (Q_G / (Q_G + Q_L))$. A deviation between ε and β is observed leading to values of ε smaller than β. It can be explained by writing the mass balance of the gas phase, as:

$$A \cdot (j_G + j_L) \cdot \beta = A \cdot U_B \cdot \varepsilon \qquad \text{(Eq. 4-2)}$$

Due to the fact that the bubble travels slightly faster than predicted by the superficial two-phase velocity, ε should be logically smaller than β to verify this mass balance. The degree of deviation depends on the flow regime:

- relatively large for the Taylor flow (ranging from 1.17% to 15.95% with a mean deviation of 8.86%), confirming the occurrence of bubble slip velocity;
- moderate for the slug-annular flow, varying from 0.49% to 9.03% with a mean deviation of 4.46%;
- small for the annular flow, varying from 0.45% to 0.88% with a mean deviation of 0.67%.

Meanwhile, the Taylor flow regime is characterized by relatively low and moderate volumetric quality of gas β (between 0.17 and 0.67). Higher β lead to non-uniform bubble size distribution and irregular gas-liquid flow, like slug-annular flow, until reaching the annular flow regime for which β is up to 0.90.

The evolution of bubble velocity U_B as a function of the two-phase superficial velocity j is plotted in **Fig. 4-5** (b). It can be observed that the values of U_B are always larger than those of j, thus indicating that there exists a slip phenomenon between bubbles and liquid film. The relationship between U_B and j could be usually correlated using the drift-model (Zuber and Findlay, 1965), as following:

$$U_B = P_0 \cdot j + U_d \qquad \text{(Eq. 4-3)}$$

where, in the case of vertical two-phase-flows, P_0 represents the distribution parameter, which takes into account the effect of non-uniform flow and concentration profiles; U_d the drift velocity, which considers the effect of the local relative velocity. In our case, the distribution parameter P_0 equals to 1.27, which is consistent with the values encountered in the literature that vary between 0.85 to 1.38 (Tsoligkas et al., 2007); the drift velocity U_d equals to -0.0043 $m \cdot s^{-1}$.

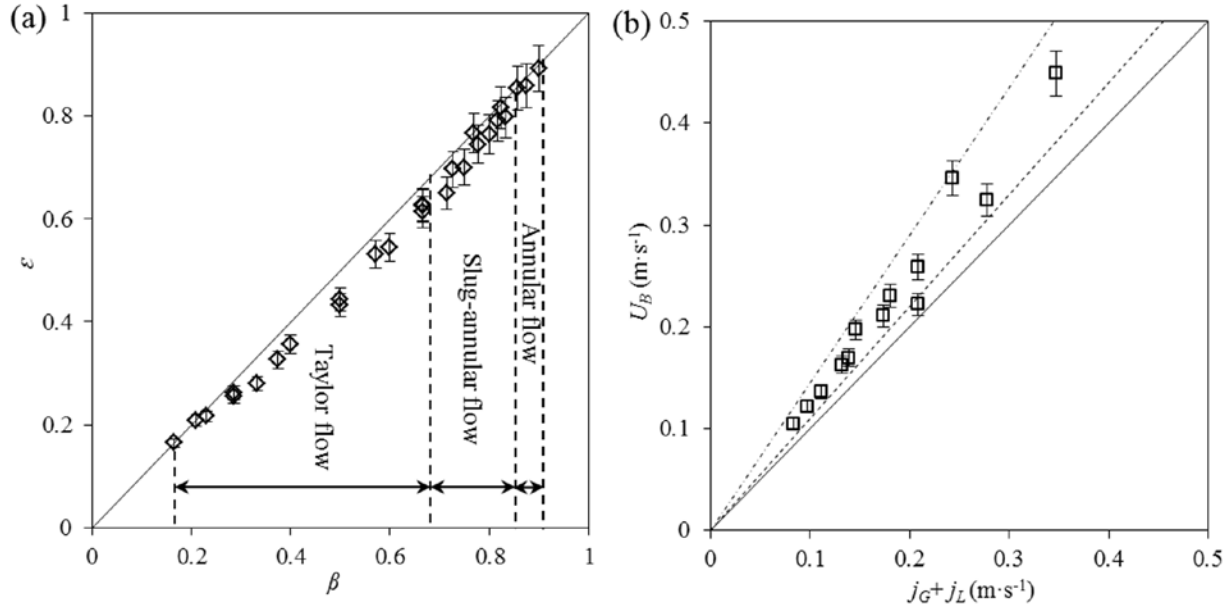

Fig. 4-5 (a) Evolution of gas hold-up as a function of the volumetric quality of gas in the meandering channel. (b) Bubble velocity versus two-phase superficial velocity. The solid line represents $U_B = j_G + j_L$, the dashed line $U_B = 1.1(j_G + j_L)$, the dash dotted line $U_B = 1.45(j_G + j_L)$.

4.2.1.2 Bubble length and slug length

For the operating conditions corresponding to the Taylor regime (0.014 m·s^{-1} ≤ j_G ≤ 0.208 m·s^{-1} and 0.069 m·s^{-1} ≤ j_L ≤ 0.139 m·s^{-1}), the dimensionless Bond number $Bo = \rho_L \cdot g \cdot l_2 / \sigma$ equals to 0.52, the Weber numbers $We = \rho_L \cdot U_B{}^2 \cdot l / \sigma_L$ range from 0.29 to 5.32, the capillary numbers $Ca = \mu_L \cdot U_B / \sigma_L$ from 0.0015 to 0.0066 and the Reynolds numbers $Re = \rho_L \cdot U_B \cdot l / \mu_L$ from 188 to 806. For meandering channels, one should also consider the dimensionless number comparing the centrifugal forces and capillary effects, defined as $Ce = \rho_L \cdot U_B{}^2 \cdot l^2 / \sigma_L \cdot r_c$: it ranges from 0.39 to 7.19.

The relationship between the normalized bubble length L_B / l and the ratio of gas superficial velocity and liquid superficial velocity, $\alpha = j_G / j_L$, is plotted in **Fig. 4-6** (a). Typically, the smallest and largest bubble lengths are 2.53 mm and 8.22 mm respectively, corresponding to

normalized bubble lengths by the width of channel L_B / l ranging from 1.27 to 4.11. It is important to precise that no obvious decrease of L_B was observed along the axial distance X (not shown here), indicating that the compressibility effects of the gas phase are negligible in the channel. Garstecki et al. (2006) observed that for T-junctions with aspect ratio greater than or equal to 1, the squeezing mechanism was expected to dominate the bubble formation for $Ca < 0.01$. Therefore, a simple scaling law was proposed to predict the bubble length, as below:

$$\frac{L_B}{l} = 1 + \alpha \cdot \frac{j_G}{j_L} \qquad \text{(Eq. 4-4)}$$

where the value of α depends on the geometry of the T-junction. It can be seen from **Fig. 4-6** (a) that the linear evolution between L_B / l and j_G / j_L is experimentally verified, which would indicate that the squeezing mechanism is suitable to predict the bubble length. In the present study, by using the linear least square regression method, it can be obtained:

$$\frac{L_B}{l} = 1 + 1.69 \cdot \frac{j_G}{j_L}, \text{ mean deviation: } 6.40\% \qquad \text{(Eq. 4-5)}$$

The present value of λ is larger in comparison with the one obtained by Roudet et al. (2011) (equals 1.13). This could be explained by the fact that in Roudet et al. (2011), the experiments were not carried out in aqueous solutions of glucose and sodium hydroxide, but in water, and also that the channel's wettability could have changed.

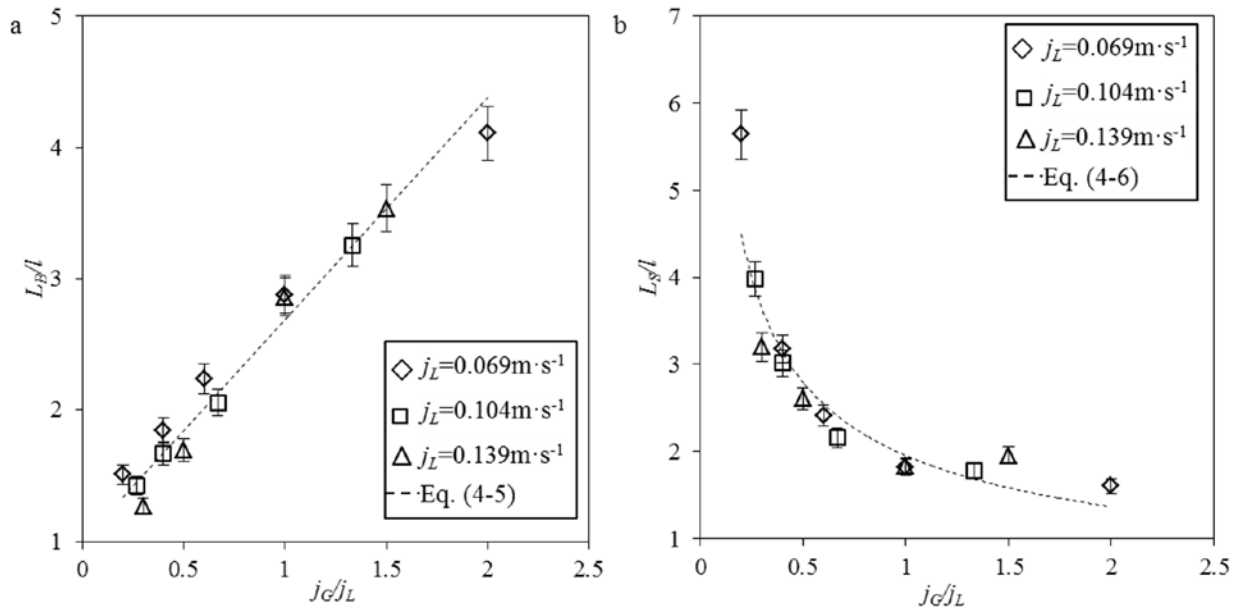

Fig. 4-6 (a) Normalized bubble length and (b) normalized slug length versus gas liquid flow rate ratio for varying liquid phase velocities in Taylor flow regime in the meandering channel.

Fig. 4-6 (b) plots the variation of normalized slug length L_S / l as a function of j_G / j_L. For a given j_L, L_S / l first decreases significantly with the increase of j_G / j_L, and then changes slightly, but remain slightly dependent on j_L. This is consistent with the literature (Qian and Lawal, 2006; Leclerc et al., 2010; Roudet et al., 2011; Abadie et al., 2012). Regression of the experimental data provides the following correlation:

$$L_S / l = 1.87 \cdot (\frac{j_G}{j_L})^{-0.5}, \text{ mean deviation: 8.6\%} \qquad \text{(Eq. 4-6)}$$

The value of the power of j_G / j_L underlines the predominant contribution of the flow rate ratio to L_S.

Table 4-2 summarizes all the measured bubble characteristics.

Table 4-2 Bubble characteristics versus gas and liquid flow rates in the meandering channel. k_La_{Roudet} represent the values obtained by Roudet et al. (2011) under the same operating conditions in meandering channel.

j_L (m·s^{-1})	j_G (m·s^{-1})	U_B (m·s^{-1})	Re	L_B (mm)	L_S (mm)	e	a (m^{-1})	k_La (s^{-1})	k_La_{Roudet} (s^{-1})	k_L (m·s^{-1})
0.069	0.014	0.105	188.6	3.02	11.29	0.786	442	0.115		2.60×10^{-4}
0.069	0.028	0.122	218.5	3.69	6.35	0.883	727	0.128		1.76×10^{-4}
0.069	0.042	0.136	245.3	4.48	4.82	0.925	932	0.147		1.58×10^{-4}
0.069	0.069	0.169	304.5	5.76	3.63	0.959	1216	0.157	0.148	1.29×10^{-4}
0.069	0.139	0.222	399.0	8.22	2.90	0.978	1600	0.207	0.279	1.29×10^{-4}
0.104	0.028	0.163	292.7	2.85	7.97	0.805	554	0.232		4.19×10^{-4}
0.104	0.042	0.197	354.2	3.34	6.03	0.886	725	0.254		3.51×10^{-4}
0.104	0.069	0.211	379.0	4.12	4.31	0.914	1001	0.269		2.69×10^{-4}
0.104	0.139	0.346	621.4	6.51	3.57	0.966	1384	0.353		2.55×10^{-4}
0.139	0.042	0.230	414.3	2.53	6.40	0.808	607	0.309		5.09×10^{-4}
0.139	0.069	0.259	465.1	3.39	4.21	0.886	846	0.324	0.239	3.83×10^{-4}
0.139	0.139	0.324	583.1	5.73	3.67	0.947	1226	0.387	0.441	3.16×10^{-4}
0.139	0.208	0.449	806.5	7.07	3.91	0.976	1442	0.446		3.09×10^{-4}

4.2.1.3 Bubble shape

In the Taylor flow regime, the cartography of bubble shape displayed in **Fig. 4-4** shows that depending on the dimensionless numbers (Ca, We, Ce), the bubble shape changes. It can be observed that:

- when Ca <0.003, the bubble shape is slightly deformed, which is in agreement with what was observed in the creeping flow (Ca <0.01) by Giavedoni and Saita (1999). However, in the present study (0.0015< Ca <0.0066), not only the viscous force could be attributed to the bubble shape, but also the inertial force (0.29< We <5.32).
- when We <1.40, the nose and rear menisci of the bubble could be well described as two hemispherical caps; however, when We >1.40, the front meniscus goes flat, while the rear meniscus turns slender. This phenomenon is consistent with the one observed by

Roudet et al. (2011), which the bubble changes in shape were observed when We >1.5.

- when the bubble passes the bends, the centrifugal effect becomes essential. Compared with the inertial forces, the centrifugal forces have the same order of magnitude (0.39< Ce <7.19), thus the bubble shape is distorted by the contributions from both two forces. When Ce <1.90, the extent of distortion of the bubble is slight; by increasing Ca , We and Ce , the bubble deformation appear to be more pronounced.

4.2.1.4 Interfacial area

The Taylor bubbles flowing in the meandering channel were not only affected by inertial effects, but also by the centrifugal effects induced by their passage in the periodic bends (see **Fig. 4-4**). These shape distortions imply that the bubbles cannot be described, as classically done, by two hemispherical caps for the bubble nose and rear, with a cylindrical shape for the bubble body. As a consequence, the bubbles were here considered as prolate ellipsoid, leading to

$$S_B = \frac{\pi \times l^2}{2} \times [1 + \frac{L_B}{l \cdot e} \arcsin(e)] \quad \text{(Eq. 4-7)}$$

$$V_B = \frac{\pi \times l^2 \times L_B}{6} \quad \text{(Eq. 4-8)}$$

where S_B and V_B represent the surface and the volume of the bubble, respectively, and e is the eccentricity of the ellipsoidal bubble, $e^2 = 1 - \frac{l^2}{L_B{}^2}$.

For the conventional gas-liquid contactors, the definition of interfacial area a can be as follow:

$$a = \frac{S_G}{V_T} \quad \text{(Eq. 4-9)}$$

where S_G is the total surface of the bubbles in the contactor, and V_T the whole volume of gas and liquid phases. In our case, due to the fact that one unit cell, which is constituted of one bubble and one liquid slug, appears repeatedly along the channel for Taylor flow regime, one can define a as below:

$$a = \frac{S_B}{V_{UC}} = \frac{S_B}{V_L + V_B} \quad \text{(Eq. 4-10)}$$

where V_{UC} is the volume of one unit cell, and V_L the volume of the liquid phase, which includes the volume of liquid slug and liquid film. As the gas fraction $\beta = Q_G/(Q_G + Q_L) = V_B/(V_B + V_L)$, (Eq. 4-10) can be rewritten as:

$$a = \beta \times \frac{S_B}{V_B} = \beta \times \frac{3}{L_B} \times [1 + \frac{L_B}{l \cdot e} \arcsin(e)] \quad \text{(Eq. 4-11)}$$

Fig. 4-7 plots the evolution of a as a function of β: a linear relationship exists between a and β. From (Eq. 4-11), it can be known that the slope represents the ratio of S_B and V_B, namely, no matter how L_B varies, $\frac{S_B}{V_B}$ remains almost constant. The values of a, ranged from 400 to 1600 m^{-1}, are reported in **Table 4-2** for the different operating conditions.

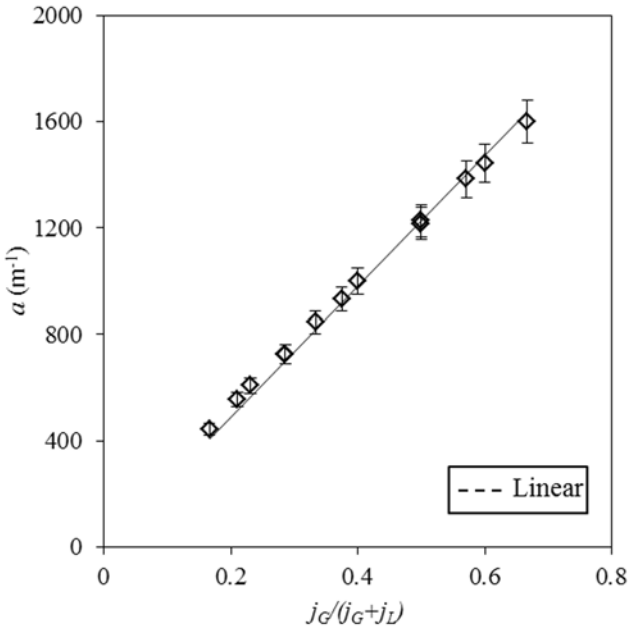

Fig. 4-7 Evolution of the interfacial area *a* as a function of gas fraction *β*.

4.2.2 Gas-liquid mass transfer

With the colorimetric technique, it is possible to locally visualize the oxygen transferred in the liquid slugs as far as the bubbles move along the channel length. Both the evolution of equivalent O_2 concentration fields in the liquid slug and the quantitative characterization of the O_2 transferred could be obtained from the image processing, which will be described in the following subsections, respectively.

4.2.2.1 Equivalent O_2 concentration fields

Firstly, for illustrative purpose, **Fig. 4-8** presents the temporal evolution of the equivalent O_2 concentration fields in a liquid slug located before a bubble, from the moment right after the bubble pinch-off to the following times when the bubble flows along the bends (j_L = 0.139 m·s^{-1}, j_G = 0.069 m·s^{-1}). It can be observed that at the beginning (t = 0 ms, bubble right after the pinch-off):

– oxygen accumulates in the front of the bubble: this is a consequence of the bubble formation stage, during which the transfer of oxygen mainly occurs in the front part of the bubble. This is consistent with what has been observed in the straight channel (see Chapter 3, **Fig. 3-3**.

– several filaments of higher O_2 concentration can be distinguished in the liquid slug. Two non-symmetrical recirculation zones with respect to the channel centerline could be identified, whereas in straight channels, two recirculation loops symmetrical and equal in size take place.

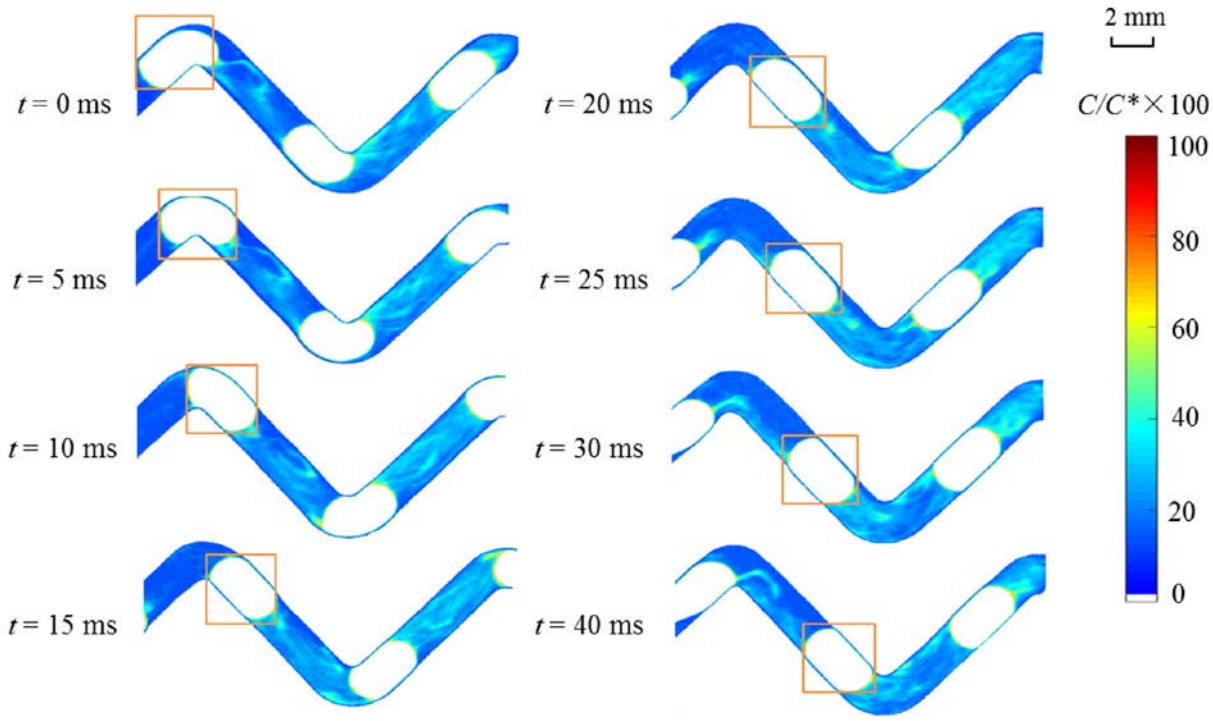

Fig. 4-8 Temporal evolution of the equivalent oxygen concentration fields in a liquid slug, from the moment right after the bubble pinch-off to the following times where the observed bubble moves in the meandering channel (operating condition: j_L = 0.139 m·s^{-1}, j_G = 0.069 m·s^{-1}, flow direction from left to right). The bubble in the orange rectangle represents the bubble observed.

When the liquid slug moves in the straight section between two bends (t = 5 ms and t = 10 ms), the amount of oxygen accumulated just in the front of the bubble tends to decrease as

progressively transported towards the liquid slug core; the recirculation zones are also growing, until reaching to the first bend (t = 15 ms). At this location, they are twisted and split up. Then, the passage through a bend affects significantly the shape and locations of these recirculation zones, and more generally the structure of the flow in the liquid slug. These distortions of the filaments of higher oxygen concentrations can be explained by the centrifugal effects induced by the channel curvature and the occurrence of the Dean vortices (Anxionnaz-Minvielle et al., 2013, Dai et al., 2015b). Herein, the mixing in the liquid slugs can be enhanced, the change in equivalent oxygen concentration fields in the liquid slugs as far as the bubbles moves is an indirect measure of this phenomenon (t = 20 - 40 ms).

The corresponding temporal evolution of the amount of transferred O_2 in the liquid slug is displayed in **Fig. 4-9**. A kind of critical point seems to exist corresponding to the time where the recirculation zones are passing the bend (t = 20 ms). Before this point, the slope of the curve is higher than the one after the point. This would highlight first the contribution of the bubble formation stage to the mass transfer, and then a slowed-down mass transfer due to the mixing effect induced by the bend that could decrease the average driving force in the liquid slugs. Deeper investigations would be required to confirm this first trend.

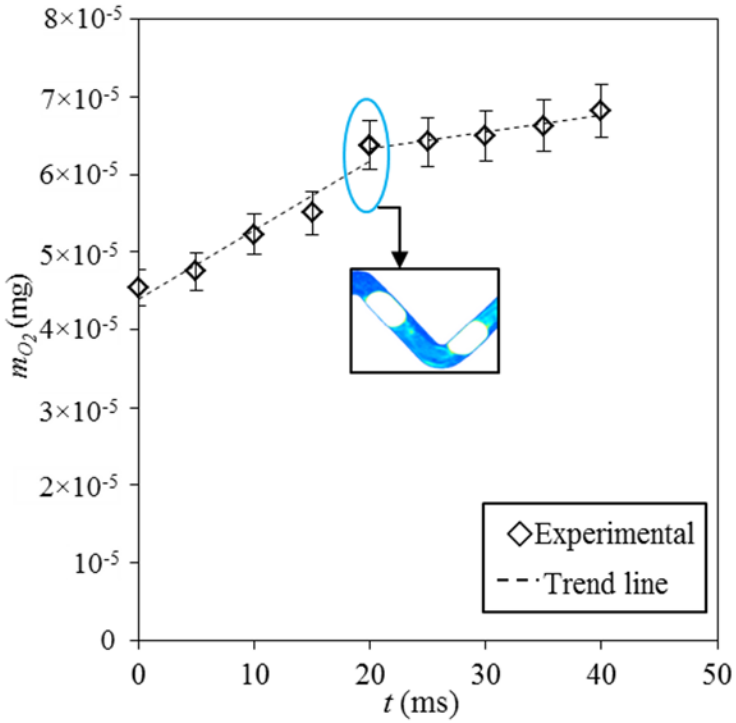

Fig. 4-9 Evolution of the amount of transferred oxygen in the liquid slug as a function of time, from the moment right after the bubble pinch-off to the following times where the observed bubble moves in the meandering channel (operating condition: j_L = 0.139 m·s^{-1}, j_G = 0.069 m·s^{-1}).

Fig. 4-10 shows the evolution of O_2 concentration fields in the liquid slug obtained at different axial positions (X = 0.02, 0.07, 0.12, 0.17, 0.22, 0.32 and 0.42 m) along the meandering channel (j_L = 0.139 m·s^{-1}, j_G = 0.069 m·s^{-1}). It can be seen that the equivalent O_2 concentration level in the liquid slugs is getting greater and greater, until reaching an almost saturated state at X = 0.42 m. The apparent recirculation zones inside the liquid slugs also tend to disappear as far as flowing in the channel and thus the concentration fields become more and more uniform in the liquid slugs. This indicates that after several bends (about 20 bends), the gradient of O_2 concentration within the liquid slug no longer exists. The accumulation of O_2 at the front and at the rear of the bubble can be observed along the first bends, and tend to disappear, as the recirculation zones, for the higher axial locations, namely when the liquid slugs become almost perfectly mixed.

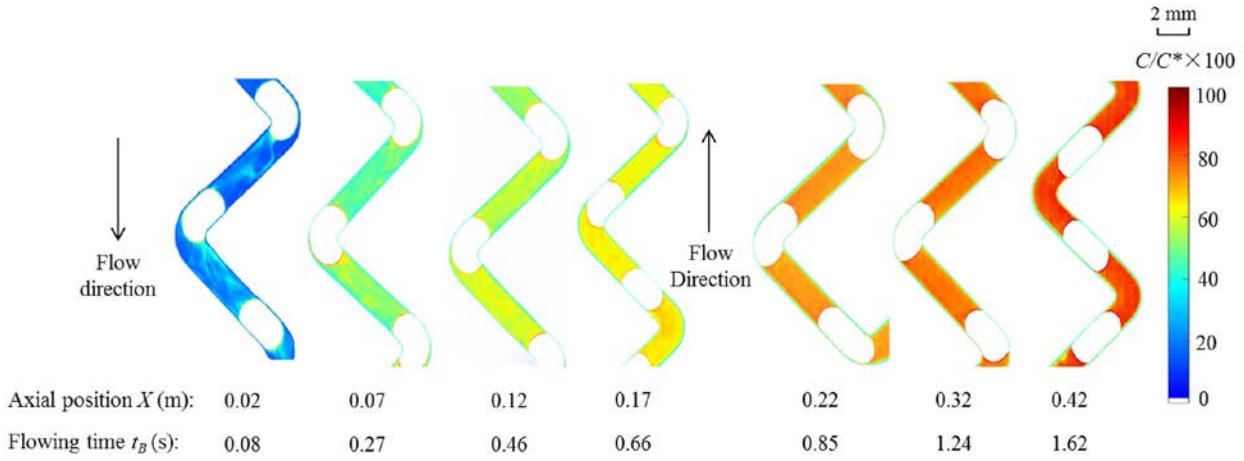

Fig. 4-10 Evolution of the equivalent oxygen concentration fields in the liquid slug as a function of the axial position in the meandering channel. Operating condition: j_L = 0.139 m·s^{-1}, j_G = 0.069 m·s^{-1}.

For different hydrodynamic conditions, a comparison of the equivalent O_2 concentration fields, observed at the axial position X = 0.07 m is proposed in **Fig. 4-11**. It can be logically observed that increasing the gas flow rate (and thus the bubble length) under a given liquid flow rate (i.e. **Fig. 4-11**. a and b, or **Fig. 4-11**. c and d, or **Fig. 4-11**. e and f) leads to a rise in the amount of oxygen transferred in the liquid slugs. The opposite effect is observed for increasing the liquid flow rate (and thus the liquid slug length) at a given gas flow rate.

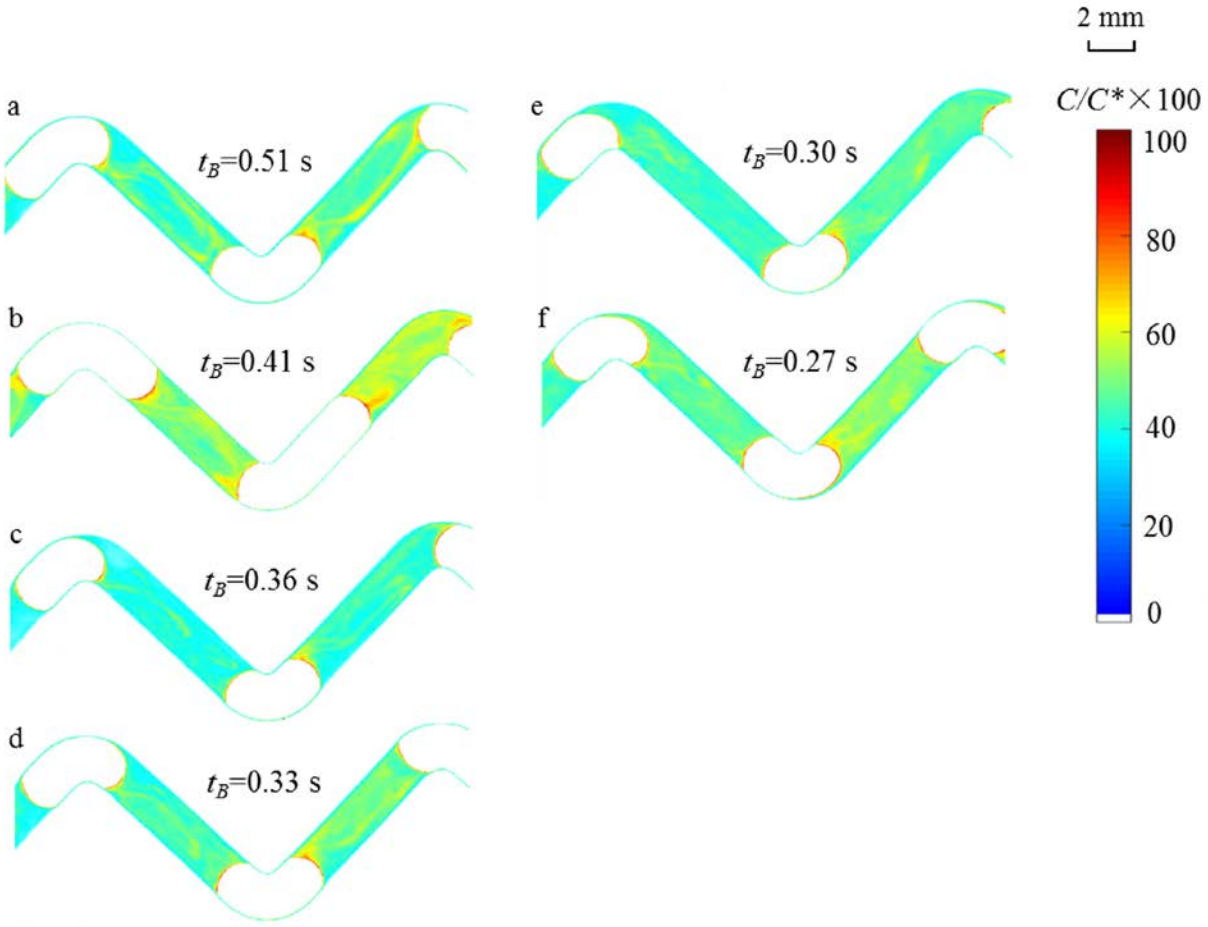

Fig. 4-11 Comparison of the equivalent oxygen concentration fields in the liquid slug under various operating conditions: (a) j_L = 0.069 m·s^{-1}, j_G = 0.042 m·s^{-1}; (b) j_L = 0.069 m·s^{-1}, j_G = 0.069 m·s^{-1}; (c) j_L = 0.104 m·s^{-1}, j_G = 0.042 m·s^{-1}; (d) j_L = 0.104 m·s^{-1}, j_G = 0.069 m·s^{-1}; (e) j_L = 0.139 m·s^{-1}, j_G = 0.042 m·s^{-1}; (f) j_L = 0.139 m·s^{-1}, j_G = 0.069 m·s^{-1}. Axial position X equals to 0.07 m.

4.2.2.2 Overall gas-liquid mass transfer coefficient

The equivalent O_2 concentration at the point (x, y) in the liquid slug could be extracted from the image processing, noted as $C(x, y)$. It is important to remind that the equivalent O_2 concentration field obtained at a given location (x, y) is a mean value along the z-axis (Dietrich et al., 2013a), no discrimination of the equivalent oxygen concentration fields related to each xy-

plane being possible along the channel height. Therefore the mass flux of O_2 transferred per unit of bubble surface at a given axial position *X*, noted as $\varphi_{O_2}(X)$, can be calculated as below:

$$\varphi_{O_2}(X) = \frac{\iiint C(x,y) \times dx \times dy \times dz}{S_B \times t_B} \quad \text{(Eq. 4-12)}$$

where t_B is the time for a bubble for flowing to the axial position *X* after the pinch-off, which is defined according to X / U_B, S_B the bubble surface, which can be calculated from (Eq. 4-7).

Fig. 4-12 (a) illustrates the evolution of φ_{O_2} in the liquid slug as a function of *X* under various j_L at a given $j_G = 0.042\text{m} \cdot \text{s}^{-1}$. It clearly appears that φ_{O_2} is not constant at all along the channel length: higher values are observed for the axial positions close to the gas injection (*X* < 0.02 m). Such result is consistent with the observations made in Chapter 3, outlining how the bubble formation stage could accelerate the mass transfer when compared to the flowing stage. Then, the value of φ_{O_2} decreases significantly as the bubble moves along the meandering channel, and tends to reach a plateau after *X* = 0.3 m.

The averaged equivalent O_2 concentration, $\overline{C}$, in the liquid slug of the unit cell (see **Fig. 4-3**. a) can be also calculated, at the given axial position *X*, from integrating of the equivalent oxygen concentration field in a unit cell, or more precisely in the liquid slug as no information could be acquired in the liquid film close to the walls. This can be expressed as below:

$$\overline{C} = \frac{\iiint C(x,y) \times dx \times dy \times dz}{L_S \times l^2} \quad \text{(Eq. 4-13)}$$

Note that as the visualization of the bubble areas of the nose and rear is also not available due to their ellipsoidal shape, the liquid volume linked to these bubble areas cannot be taken into account for the calculation. It has been estimated that this bias could lead to a maximum error of 18% on the volume estimation of liquid phase in a unit cell.

Fig. 4-12 (b) shows the evolution of the normalized averaged O_2 concentration $\overline{C}/C^*$ (C^* being the O_2 concentration at saturation) in the liquid slug as a function of the axial position X in the channel, under various gas superficial velocities j_G and at given liquid superficial velocity j_L =0.069 m·s^{-1}. It can be observed that $\overline{C}/C^*$ increases as the gas superficial velocity increases under the given liquid superficial velocity, which is consistent with the visualization presented in **Fig. 4-11**.

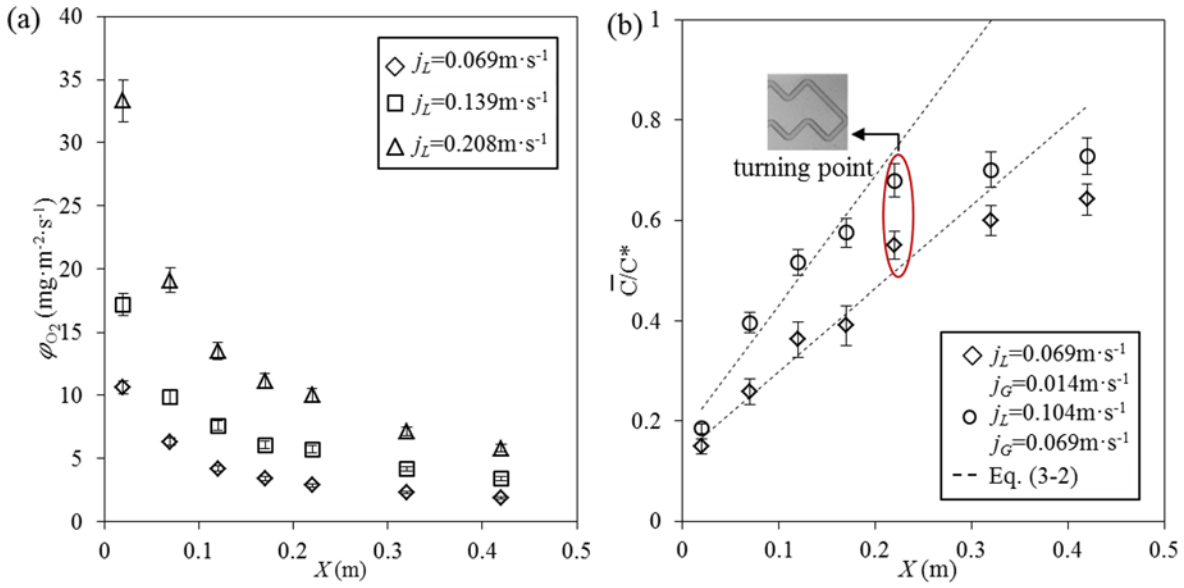

Fig. 4-12 (a) Evolution of mass flux of the transferred oxygen φ_{O_2} per unit of bubble surface as a function of the axial position X under various liquid superficial velocities j_L at a given gas superficial velocity j_G=0.042 m·s^{-1}. (b) Comparison of the evolution of normalized average oxygen concentration in the liquid slug along the channel with the ones predicted by the plug flow model. For j_L = 0.069 m·s^{-1}, j_G = 0.014 m·s^{-1}, Re = 188; j_L = 0.104 m·s^{-1}, j_G = 0.069 m·s^{-1}, Re = 379.

There exists then a linear relationship between $\overline{C}/C^*$ and X, and the slope stands for $k_L a / j_L$. Once applied, it has been found that (Eq. 3-2) could predict well the experimental values of

$\overline{C}/C^*$ only for $Re < 300$; for $Re > 300$, the deviation becomes higher than 18%. Typical examples of the comparison between the experimental and predicted evolutions of $\overline{C}/C^*$ are displayed in **Fig. 4-12** (b). Note that, when a fitting of the experimental values of $\overline{C}/C^*$ with X is applied (taking X =0.02 m as a reference), different values are obtained at X =0; this could be explained by the contribution of the bubble formation stage to the overall mass transfer. **Fig. 4-12** (b) also reveals that, for $Re > 300$, the prediction of (Eq. 3-2) are relevant only before the axial positions below X = 0.22 m. As shown in **Fig. 4-1** (b), this specific location corresponds to the big bend (called "turning point"), namely to the location where the flow direction is changed in 180 º. After X = 0.22 m, $\overline{C}/C^*$ is underestimated by the model, indicating that the big bend leads to slow down the flux of oxygen transferred (this is observed for all the operating conditions when $Re > 300$). More in-depth investigation of the velocity field structure of the two-phase flow when crossing the turning point would be required to explain this phenomenon.

The overall volumetric mass transfer coefficients deduced from the fitting between (Eq. 3-2) with the experimental points just before the turning point, $k_L a$, are reported in **Table 4-2**. They are ranged from 0.1 to 1 s^{-1}, which is in agreement with the values reported by Roudet et al (2011). As already observed in the literature (Nieves-Remacha et al., 2013b; Yao et al., 2014), $k_L a$ increases when the gas superficial velocity j_G increases and when the liquid superficial velocity j_L increases. It is important to keep in mind that these overall volumetric mass transfer coefficients are just global parameters representing the inverse of characteristic time of mass transfer. The values here estimated remain approximate due to the assumptions made in the modelling (plug-flow) and to the fact that the contribution of the film is not taken into account.

At last, as the interfacial area a can be calculated by the assumption of the bubbles as prolate ellipsoid (see section 4. 3.1.4), the liquid-side mass transfer coefficient before the turning point k_L can be calculated by dividing $k_L a$ with a. As shown in **Table 4-2**, for a given j_G, k_L increases with increasing j_L, and is less sensitive to the gas superficial velocity. With such values of k_L, the Hatta number Ha is equal to 14 (Eq. 2-9), and the enhancement factor E to 1.03 ((Eq.

2-13) and (Eq. 2-14)), thus demonstrating that there exists no enhancement of mass transfer by the reaction.

4.3 Conclusion

The colorimetric technique proposed by Dietrich et al. (2013), which was based on an oxygen-sensitive dye, was implemented to locally visualize and characterize the gas-liquid mass transfer in a square meandering millimetric channel. The hydrodynamics characteristics was first investigated in the channel, in terms of gas-liquid flow regime, gas hold-up, bubble length and velocity, liquid slug length and interfacial area. The oxygen concentration field inside the liquid slugs was then visualized at different axial positions. The non-symmetrical recirculation zones inside the liquid slug were observed to be twisted and split by the periodic bends, and tended to disappear as the bubble moving within the channel; the O_2 concentration inside the liquid slug became uniform after passing through several bends (around 20 bends). The existence of the first bend showed a slowed-down mass transfer due to the mixing effect which could decrease the average driving force in the liquid slugs. The occurrence of the "turning point" (i.e. the big bend enabling the flow direction in 180º) seemed to induce a slowing down of the mass transfer, especially when $Re > 300$ and $Ca > 0.002$. The mass flux of O_2 transferred per unit of bubble surface was significantly higher close to the gas injection due to the bubble formation stage, then it decreases significantly as the bubble flowing along the meandering channel, and becomes small after $X = 0.3$ m due to the decreasing driving force for the mass transfer. At last, by coupling this local information with a plug-flow model, overall volumetric mass transfer coefficients could be estimated. All these findings give important information to understand the gas-liquid mass transfer complex mechanism occurring in the meandering channel, which would serve as basis for implementing gas-liquid reaction in HEX reactors.

CHAPTER 5

Does a meandering geometry of millimetric channels enable to intensify the performances of gas-liquid mass transfer, when compared to a straight one?

Résumé: Ce chapitre compare les performances en terme de transfert de matière entre un canal droit et un canal sinueux de section transversale identique égale à 2 × 2 mm^2. Les comparaisons ont été faites en dissociant : (1) l'hydrodynamique gaz-liquide, en caractérisant le régime d'écoulement, la forme des bulles, le taux de gaz, la longueur des bulles, la vitesse des bulle et l'aire interfaciale et (2) le transfert de matière gaz-liquide, en termes de coefficient de transfert de matière volumique, de nombre d'unités de transfert en phase liquide (NTU_L) et d'efficacité de transfert de matière. Les résultats ont révélé que l'utilisation de la géométrie sinueuse permet d'augmenter le coefficient de transfert de matière volumique de 12% en moyenne, ainsi que l'efficacité du transfert. Ceci indique que la géométrie sinueuse du canal pourrait intensifier le transfert de matière. Il a été également montré que le NTU_L est resté similaire dans les deux systèmes utilisés. Ainsi, même si les canaux millimétriques permettent une intensification du transfert de matière gaz-liquide par rapport aux contacteurs gaz-liquides conventionnels, il faudra garder à l'esprit la nécessité de conserver des temps de passage suffisants. Enfin, des nouvelles lois d'échelle ont été proposées pour prédire les flux de matière d'oxygène transférés (via le nombre Sherwood) en fonction de la position axiale (via le nombre de Graetz) dans les deux systèmes et pour différentes conditions opératoires (via le nombre de Péclet).

Abstract: The chapter 5 rigorously compared the performances between the straight and meandering channels by carrying out specific experiments in a straight channel, whose channel cross-section and compactness were identical to those of the meandering channel (channel cross-section equals to 2×2 mm^2). The comparisons were made considering two aspects: (i) gas-liquid hydrodynamics, in terms of the flow regimes, bubble shape, gas hold-up, bubble and slug length, bubble velocity and interfacial area and (ii) gas-liquid mass transfer, in terms of the volumetric mass transfer coefficient, Number of Transfer Units in the liquid phase *(NTU_L)*, and mass transfer efficiency. It answered the scientific question that whether the meandering geometry can improve the gas-liquid mass transfer or not. The results revealed that using the meandering geometry instead of a straight one is an efficient method to increase the volumetric mass transfer coefficient $k_L a$ (by 12% on average), as well as the mass transfer efficiency (up to 0.8-0.9 against 0.55-0.65 for the higher location). It was also showed that NTU_L remained low (close to one) in both straight and meandering channels; thus, even if the millimetric channels allowed gas-liquid mass transfer intensification when compared to the conventional gas-liquid contactors, one should keep in mind the need to generate sufficient residence times. At last, original scaling laws were proposed to predict the variations of the oxygen mass fluxes transferred (via the Sherwood number *Sh*) as a function of the axial position (via the Graetz number *Gz*) in both channels and for different operating conditions (via the Péclet number).

Introduction

The main objective of this chapter is to compare the performances of gas-liquid mass transfer around Taylor bubbles flowing in two geometries of millimetric square channels, namely, straight and meandering ones. The underlying scientific question is to know if the meandering geometry, such as designed, enables or not to intensify the gas-liquid mass transfer. For that, the colorimetric technique has been first implemented in a straight millimetric square channel for comparison purposes.

Section 5.1 will present the material and methods used, which are very similar to the ones described in Chapter 4.

Section 5.2 will be devoted to the investigation of the gas-liquid hydrodynamics in the straight channel, in terms of flow regimes, overall gas hold-up, bubble velocity, bubble and liquid slug lengths, bubble shape and interfacial area. A comparison with the meandering channel will be systematically performed for each parameter studied.

Section 5.3 will investigate the gas-liquid mass transfer in the straight channel, in terms of oxygen concentration fields and mass transfer coefficients. The effect of the large bends composing the channel will be in particular highlighted.

In Section 5.4, both geometries will be compared in terms of mass transfer efficiency using the classical concept of Number of Transfer Units. At last, scaling laws (dimensionless relationships) will be established to predict the variations of the oxygen mass fluxes transferred as a function of the axial position and hydrodynamics conditions, in both channels.

5.1 Materials and methods

5.1.1 Fluid properties

The composition of the dye solution for both hydrodynamic and mass transfer experiments was the same as used for the experiments in meandering channel in Chapter 4. All the physio-chemical properties of solutions were displayed in Chapter 4 (see **Table 4-1**).

5.1.2 Description of the experimental set-up

The experimental set-up was exactly the same as the one in Chapter 4, except for the channel. The new channel, horizontally placed, had a square cross section $A = l^2$, where $l = 2$ mm, identical to the one of the meandering channel. As illustrated in **Fig. 5-1**, every 240 mm, a large bend (curvature radius *R* of 11 mm) was designed to connect two straight channel sections with a change of 180° in the flow direction; this enabled to work with a long channel (the total developed straight length of the channel $L = 1.01\,\text{m}$), while keeping a compact device. The air flow rates Q_G ranged from 0.2 to 9 L·h^{-1} and liquid flow rates Q_L from 1 to 3 L·h^{-1}. The corresponding superficial gas velocities j_G and liquid velocities j_L were: 0.014 m·s^{-1} $\leq j_G = Q_G / l^2 \leq 0.625$ m·s^{-1} and 0.069 m·s^{-1} $\leq j_L = Q_L / l^2 \leq 0.208$ m·s^{-1}.

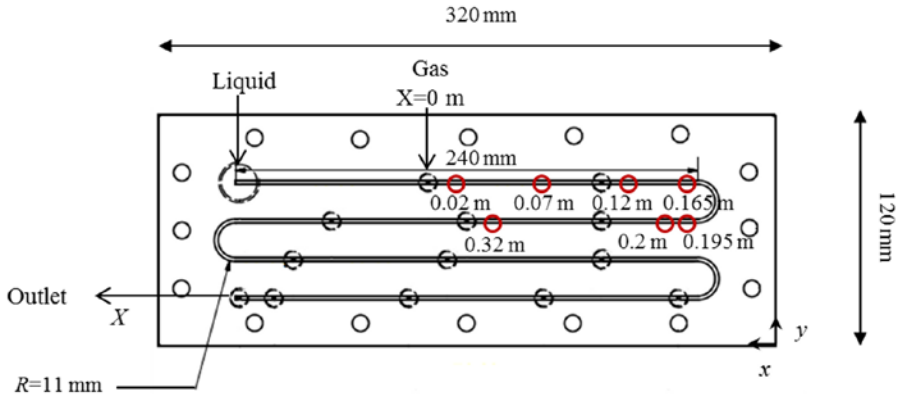

Fig. 5-1 Geometry of the long straight channel. *X* corresponds to the location (curvilinear coordinate) in the channel from the gas inlet. *X*=0: the two phases enter in contact. Cross-sectional area *A*=2×2 mm^2, total developed straight length of channel *L*=1.01 m. Red circles represent the observation positions at different axial positions.

5.1.3 Image acquisition system

The shadowgraph method was here also applied to investigate the gas-liquid hydrodynamics and mass transfer inside the straight channel. Image resolutions were 207 µm per pixel and 17 µm per pixel for the hydrodynamics and mass transfer experiments, respectively; the associated regions of interest were 211.6×105.6 mm^2 and 17.2×4.3 mm^2, respectively. For the mass transfer

experiments, the gas-liquid flow was observed at 7 axial distances X from the gas injection, namely: X = 0.02 m, 0.07 m, 0.12 m, 0.165 m, 0.195 m, 0.2 m and 0.32 m, as depicted in **Fig. 5-1**.

5.1.4 Image processing

A typical raw image of the gas-liquid flow all along the channel length (1.01 m) is shown in **Fig. 5-2** (a). In order to extract the hydrodynamics parameters (gas hold-up, bubble length and velocity, liquid slug length etc.) from the raw image, a background image, corresponding to a channel filled with the liquid phase, was needed, shown in **Fig. 5-2** (b). Then, the same image post-treatment algorithm as in Chapter 4 was implemented on the software Matlab (R2015a). Typical examples of the detection of all the bubbles and liquid slugs inside the channel are displayed in **Fig. 5-2** (c) and (d) respectively. Then, the areas of all the 2D bubbles and 2D liquid slugs appearing along the whole length of the channel, noted as A_B and A_S (i.e. the areas projected in the plane *xy*, respectively, see **Fig. 5-1**) could be obtained, then enabling the gas hold-up to be calculated according to (Eq. 4-1).

Bubble characteristics (i.e. bubble length L_B, liquid slug length L_S, and bubble velocity U_B) were determined only in Taylor flow regime. The averaged values of L_B and L_S were calculated by considering 20 bubbles on one image and 20 images were used. For a given operation condition, the standard deviations of the bubble characteristics (L_B, L_S and U_B) of all the bubbles inside the channel were smaller than 5% of the averaged value and did not change along the channel length.

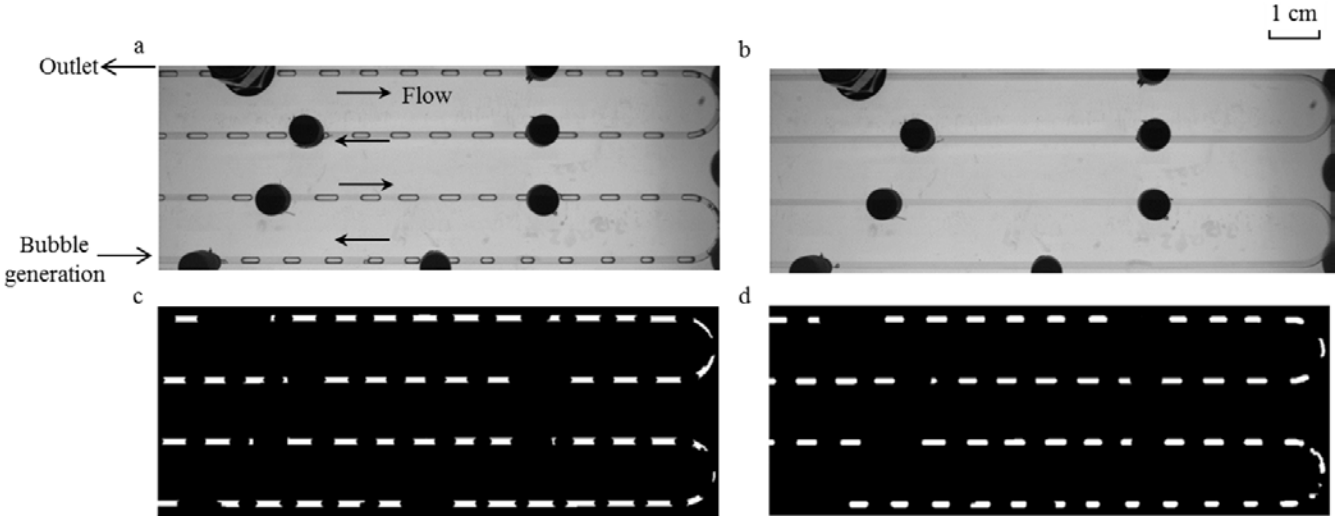

Fig. 5-2 Sequence of image processing in the straight channel. (a) Typical raw image of gas-liquid flows. (b) Raw image of the channel filled with liquid phase. (c) Detection of the bubbles (binary image). (d) Detection of the liquid slugs (binary image). Operating condition: j_L = 0.139 m·s^{-1}, j_G = 0.069 m·s^{-1}.

The gas-liquid mass transfer characteristics were determined by using the same image post-treatment algorithm as in Chapter 4 (see section 4.1.5.2).

5.2 Gas-liquid hydrodynamics

5.2.1 Flow regimes, overall gas hold-up and bubble velocity

The cartography of gas-liquid flow regimes, which depends on j_G and j_L, is displayed in **Fig. 5-3** in the case of the straight channel. Under the present operating conditions (0.014 m·s^{-1} ≤ j_G ≤ 0.625 m·s^{-1}; 0.069 m·s^{-1} ≤ j_L ≤ 0.208 m·s^{-1}), the same regimes than in the meandering channel were identified, namely: the Taylor flow regime ($L_B / l \leq 5$), long slug flow regime ($L_B / l > 5$) and the slug-annular flow regime.

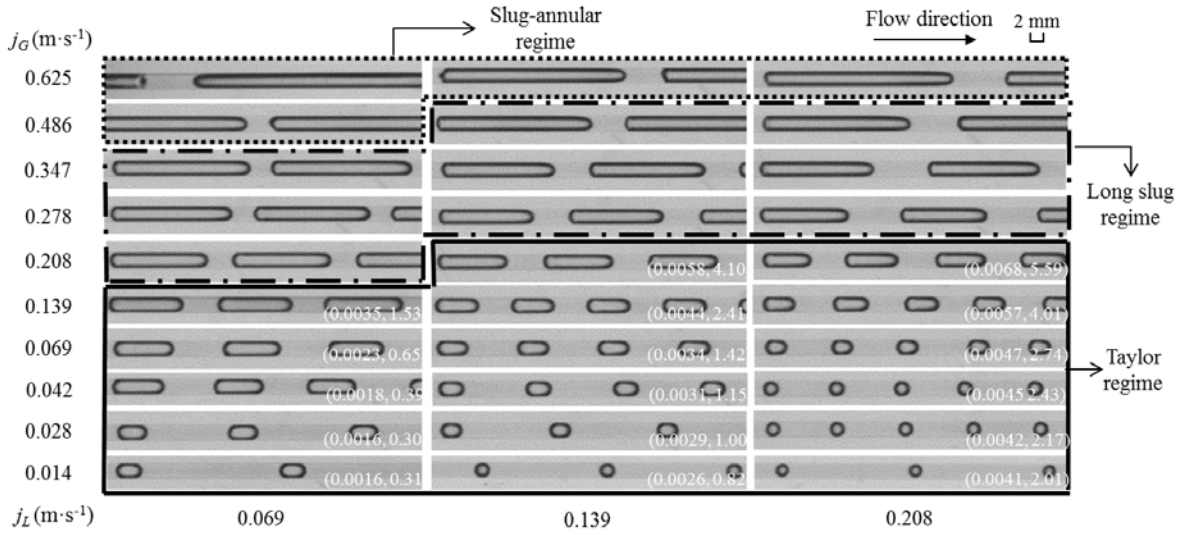

Fig. 5-3 Cartography of gas-liquid flow regimes in the straight channel. The flow regimes in the frame with solid lines correspond to the Taylor regime ($L_B / l \leq 5$), with dash dotted lines the long slug regime ($L_B / l > 5$), and with dotted lines the slug-annular regime. The numbers in the brackets correspond to (*Ca*, *We*).

The comparison of the flow maps between both channels (see **Fig. 5-3** and **Fig. 4-4**, respectively) demonstrates that the transition from Taylor flow regime to slug-annular flow regime occurs at different gas and liquid superficial velocities:

- For the straight channel, the transition occurs at 0.347 m·s^{-1} ≤ j_G ≤ 0.486 m·s^{-1} when j_L ≤ 0.069 m·s^{-1}, and at 0.486 m·s^{-1} ≤ j_G ≤ 0.625 m·s^{-1} when j_L > 0.069 m·s^{-1};
- For the meandering channel, the transition occurs at 0.139 m·s^{-1} ≤ j_G ≤ 0.208 m·s^{-1} when j_L ≤ 0.104 m·s^{-1}, and at 0.208 m·s^{-1} ≤ j_G ≤ 0.278 m·s^{-1} when j_L > 0.104 m·s^{-1}.

These observations indicate that the transition from Taylor flow to slug-annular flow regime is delayed in the straight channel when compared with the meandering channel.

The evolution of gas hold-up ε (measured over the whole length of the channel, see (Eq. 4-1)) is plotted in **Fig. 5-4** (a) as a function of the volumetric quality (fraction) of gas β, defined by the ratio of gas-liquid flow rates $Q_G /(Q_G + Q_L)$. A deviation between ε and β is logically

observed leading to values of ε smaller than β. Such trend, already observed in the meandering channel, is consistent considering the fact that the bubbles travel slightly faster than the superficial two-phase velocity (see mass balance (Eq. 4-2).

The degree of deviation between ε and β depends on the flow regime:

- relatively large for the Taylor flow (ranging from 1.20% to 15.80% with a mean deviation of 8.17%), which confirms the occurrence of bubble slip velocity;
- moderate for the long slug flow, varying from 2.50% to 8.60% with a mean deviation of 6.42 %;
- small for the slug-annular flow, varying from 1.20% to 2.10% with a mean deviation of 1.53%.

Meanwhile, Taylor flow regime is characterized by relatively low and moderate volumetric quality of gas β (between 0.12 and 0.67). The gas hold-up ε is, under the same (j_G , j_L), slightly larger (+4% on average) in the straight channel than that in the meandering channel for the Taylor flow regime. For the slug-annular flow regime, they are almost identical.

The evolution of bubble velocity U_B as a function of the superficial two-phase velocity j is plotted in **Fig. 5-4** (b). The values of U_B are (i) always larger than those of j , (ii) slightly smaller (-7% on average) in the straight channel than that in the meandering channel. The drift-model (Zuber and Findlay, 1965), presented in (Eq. 4-3), is here also used to correlate U_B and j , leading to a distribution parameter P_0 and to a drift velocity U_d equal to 1.11 and to -0.007 m·s^{-1}, respectively. These later values are smaller and larger than in meandering channel (1.27 and -0.0043 m·s^{-1}) respectively. Roudet et al. (2011) have shown, using mass balance equation, that the dimensionless relative slip velocity W can be related to the relative cross-sectional area of the liquid film, as below:

$$W = \frac{U_B - (j_G + j_L)}{U_B} = \frac{A_f}{A} - \frac{q_f}{A \cdot U_B} \qquad \text{(Eq. 5-1)}$$

where A_f is the cross-sectional area of the liquid film ($A_f = A - A_{cross,b}$, with $A_{cross,b}$ the bubble cross-sectional area), q_f the liquid flow rate in the film between channel walls and bubbles. The variations of *W* with *Ca* in both straight and meandering channels are plotted in **Fig. 5-4** (c). Even if no obvious trend can be observed between *W* with *Ca*, the values of *W* in the meandering channel are always higher than those in the straight channel. If one considers that the liquid film is stagnant (q_f = 0), such result would indicate that due to the complex flow induced by the bends, the relative cross-sectional area of liquid film in the meandering channel (ranged from 0.14 to 0.30) could be larger, in average, than that in the straight channel (ranged from 0.08 to 0.19). Nevertheless, deeper investigations (such as liquid film thickness measurement) are at present required to fully understand this difference.

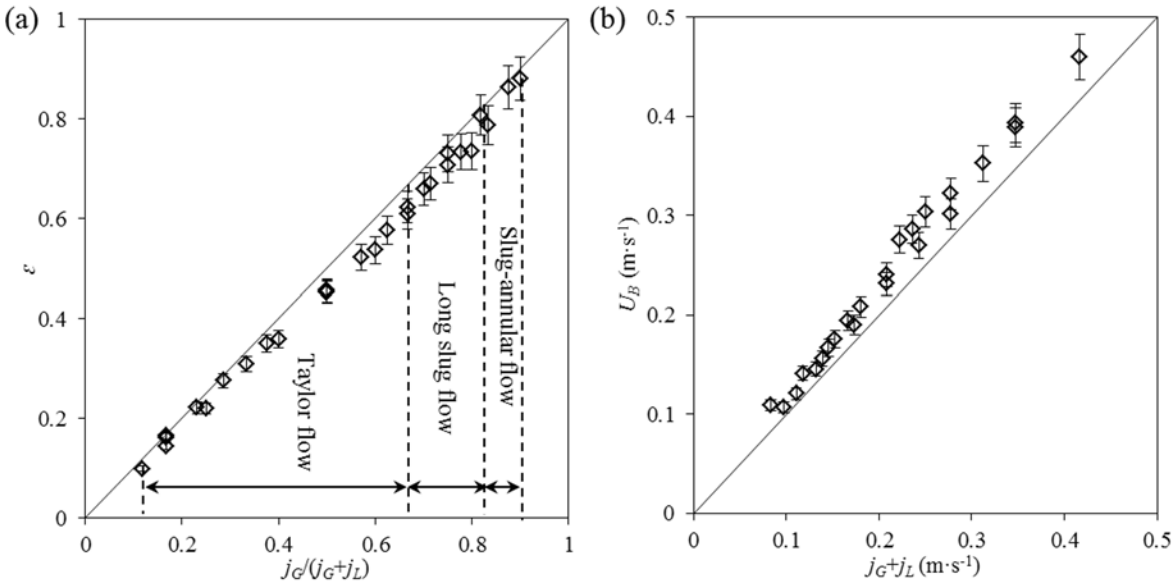

Fig. 5-4 (a) Evolution of gas hold-up as a function of the volumetric quality of gas in the straight channel. (b) Bubble velocity versus two-phase superficial velocity. The solid line represents $U_B = j_G + j_L$.

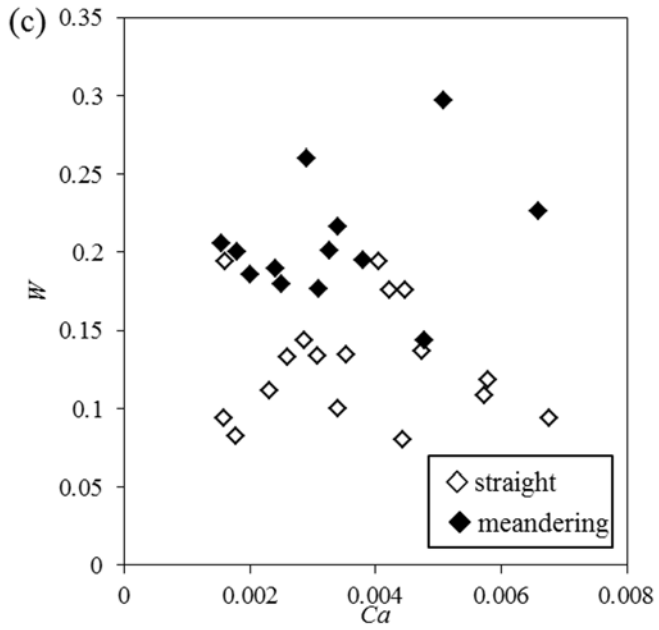

Fig. 5-4 (c) Relative slip velocity versus capillary number in the Taylor flow regime

5.2.2 Bubble length and slug length

The relationship between L_B / l and the ratio of j_G and j_L, is plotted in **Fig. 5-5**. Typically, the smallest and largest bubble lengths are 1.81 mm and 8.05 mm respectively, corresponding to the dimensionless bubble lengths L_B / l ranging from 0.91 to 4.02. Note that no decrease of L_B is observed along the axial distance X (not shown here), indicating that the compressibility effects of the gas phase are also negligible in the straight channel. As for the meandering channel, the squeezing mechanism proposed by Garstecki et al. (2006), (Eq. 4-4) is used to predict the bubble length, leading to:

$$\frac{L_B}{l} = 1 + 1.58 \cdot \frac{j_G}{j_L}, \text{ mean deviation: 7.11\%} \qquad \text{(Eq. 5-2)}$$

The present value of α is slightly smaller than the one obtained in the meandering channel (equal 1.69): smaller L_B are indeed observed in the straight channel at a given operating condition than that in the meandering channel.

Fig. 5-5 also plots the variation of the dimensionless liquid slug lengths L_S / l as a function of j_G / j_L. It can be observed that

- for a given j_L, L_S / l first decreases sharply for increasing j_G / j_L, and then changes slightly. An identical trend was observed, in the meandering channel (see **Fig. 4-6**. b), and also with the literature (Qian and Lawal, 2006; Leclerc et al., 2010; Roudet et al., 2011; Abadie et al., 2012);
- for a given j_G, L_S / l is almost independent of j_G / j_L.

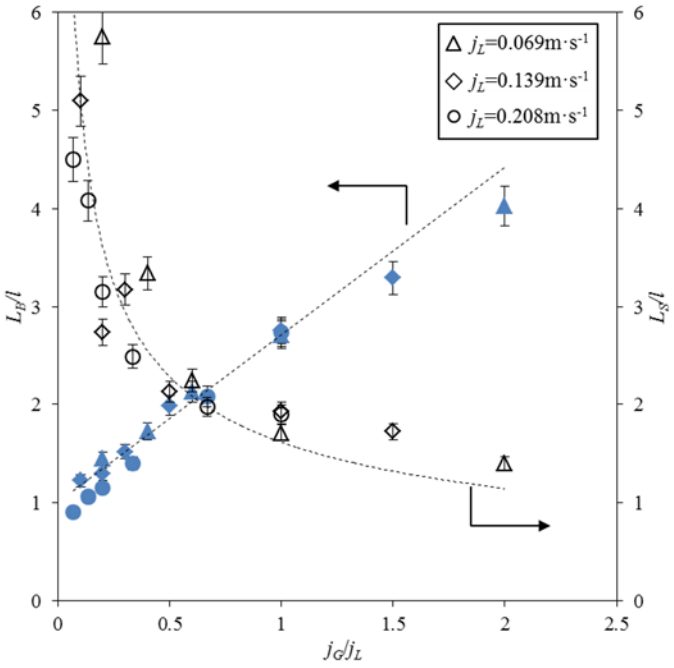

Fig. 5-5 Normalized bubble length and normalized slug length (blue symbols) versus gas liquid flow rate ratio under various liquid phase velocities in Taylor flow regime in the straight channel.

These experimental data can be described by the following scaling law:

$$L_S / l = 1.61 \cdot (\frac{j_G}{j_L})^{-0.5}, \text{ mean deviation: } 15.7\% \qquad \text{(Eq. 5-3)}$$

The value of the constant (1.61) is smaller than that in meandering channel (equals 1.87): at the same j_G / j_L, the liquid slug length L_S in the straight channel is smaller than that in meandering channel.

To sum up, using a meandering channel instead of a straight channel enables:

- bringing forward the transition between the Taylor flow regime to slug-annular flow regime (i.e. it occurs at smaller tow-phase superficial velocities);
- slightly decreasing the gas hold-up (-4%);
- slightly increasing the bubble velocities (+7%);
- slightly rising the bubble lengths and liquid slug lengths.

Such findings could be explained by the strong stretching of bubble ends when they move along the various bends of the meandering channel (see **Fig. 4-4**).

Table 5-1 summarizes all the measured bubble characteristics.

Table 5-1 Bubble characteristics versus gas and liquid flow rates in the straight channel. k_La_{Roudet} represent the values obtained by Roudet et al. (2011) under the same operating conditions in straight channel.

j_L (m·s^{-1})	j_G (m·s^{-1})	U_B (m·s^{-1})	Re_B	L_B (mm)	L_{slug} (mm)	a (m^{-1})	k_La (s^{-1})	$k_La_{meandering}$ (s^{-1})	k_L (m·s^{-1})	$k_{L,Roudet}$ (m·s^{-1})
0.069	0.014	0.109	282	2.89	11.51	424	0.104	0.115	0.000245	0.000143
0.069	0.028	0.107	333	3.45	6.68	691	0.115	0.128	0.000166	
0.069	0.042	0.121	463	4.26	4.49	869	0.139	0.147	0.000160	0.000137
0.069	0.069	0.156	762	5.42	3.42	1117	0.145	0.157	0.000130	
0.069	0.139	0.241	1740	8.05	2.79	1432	0.168	0.207	0.000117	
0.139	0.014	0.176	387	2.44	10.19	246	0.184		0.000748	
0.139	0.028	0.195	451	2.58	5.47	441	0.216		0.000490	
0.139	0.042	0.208	568	3.03	6.34	578	0.254	0.309	0.000439	0.00032
0.139	0.069	0.231	827	3.98	4.26	782	0.296	0.324	0.000379	
0.139	0.139	0.302	1496	5.51	3.86	1115	0.335	0.387	0.000300	
0.139	0.208	0.394	2330	6.58	3.44	1312	0.384	0.446	0.000293	0.00037
0.208	0.014	0.276	450	1.81	9.00	201	0.214		0.001065	
0.208	0.028	0.287	545	2.12	8.16	341	0.265		0.000777	
0.208	0.042	0.303	628	2.30	6.30	463	0.307		0.000663	
0.208	0.069	0.322	807	2.79	4.98	642	0.383		0.000597	
0.208	0.139	0.389	1457	4.16	3.95	930	0.435		0.000468	
0.208	0.208	0.460	2258	5.47	3.79	1116	0.495		0.000444	0.000427

5.2.3 Bubble shape

For the operating conditions corresponding to the Taylor regime (0.014 m·s^{-1} $\leq$ j_G $\leq$ 0.208 m·s^{-1} and 0.069 m·s^{-1} $\leq$ j_L $\leq$ 0.208 m·s^{-1}), the dimensionless Bond number *Bo* equals to 0.52, the Weber numbers *We* range from 0.30 to 5.59, the capillary numbers *Ca* from 0.0016 to 0.0068 and the Reynolds numbers *Re* from 193 to 826. As in the meandering channel, the inertial effects are dominant with respect to viscosity and gravity effects, and thus largely contributed to the deformation of bubbles.

The cartography of bubble shape displayed in **Fig. 5-3** shows that depending on the dimensionless numbers (Ca ,We), the bubble shape changes. It can be observed that:

- When $Ca < 0.0035$, the bubble shape is slightly deformed, which is in agreement with what was observed in the creeping flow ($Ca < 0.01$) by Giavedoni and Saita (1999). However, in the present study ($0.0016 < Ca < 0.0068$), not only the viscous force could be attributed to the bubble shape, but also the inertial force ($0.30 < We < 5.59$).
- When $We < 1.5$, the nose and rear menisci of the bubble could be well described as two hemispherical caps; however, when $We > 1.5$, the front meniscus goes flat, while the rear meniscus turns slender.

These findings are consistent with the one observed by Roudet et al. (2011), and in the meandering channel (see Chapter 4, **Fig. 4-4**). Nevertheless, as no centrifugal effects exist in the straight channel, the bubbles are clearly less distorted than in the meandering channel.

5.2.4 Interfacial area

As slightly distorted, the Taylor bubbles flowing in the straight channel can be reasonably described by two hemispherical caps for the bubble nose and rear, and a cylindrical shape for the bubble body. Thus, the bubble surface S_B and bubble volume V_B can be calculated as below:

$$S_B = \pi \cdot l^2 + 4 \cdot (L_B - l) \cdot l \qquad \text{(Eq. 5-4)}$$

$$V_B = \frac{\pi \times l^3}{6} + (L_B - l) \cdot l^2 \qquad \text{(Eq. 5-5)}$$

According to (Eq. 4-11), the interfacial areas a can be calculated as follow:

$$a = \beta \times \frac{S_B}{V_B} = \beta \times \frac{\pi \cdot l + 4 \cdot (L_B - l)}{\frac{\pi \times l^2}{6} + (L_B - l) \cdot l} \qquad \text{(Eq. 5-6)}$$

Fig. 5-6 plots the evolution of a as a function of the gas fraction β. A linear relationship can be seen between a and β (mean deviation equals 9%), thus showing that, whatever L_B, $\frac{S_B}{V_B}$

remains almost constant, as already observed in the meandering channel. The values of a, ranged from 201 to 1432 m^{-1}, are reported in **Table 5-1** for the different operating conditions. When compared to the meandering channel, the interfacial area a is, under the same (j_G, j_L), slightly smaller (-8% on average) in the straight channel than that in the meandering channel. This could be explained by the higher gas hold-up observed in the straight channel, even if the bubble lengths are slightly smaller.

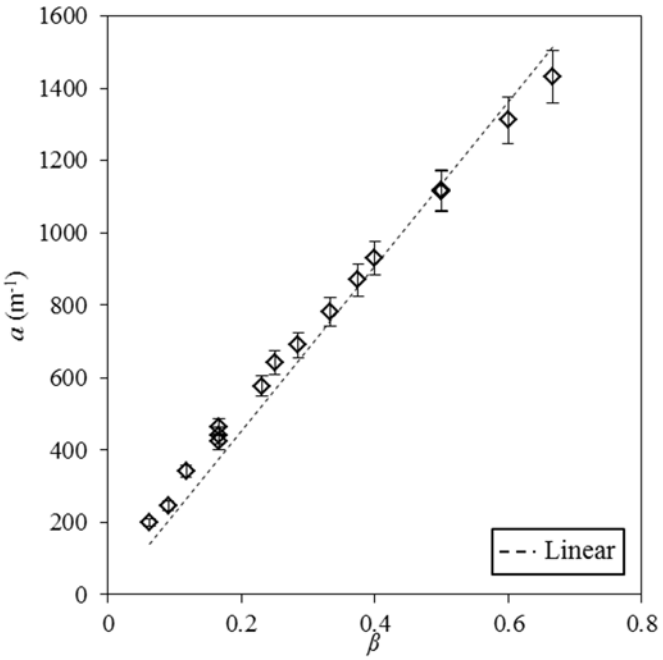

Fig. 5-6 Evolution of the interfacial area a as a function of gas fraction β in the straight channel.

5.3 Gas-liquid mass transfer

5.3.1 Equivalent O_2 concentration fields

Firstly, a comparison of the equivalent O_2 concentration fields, observed at the axial position X = 0.07 m for different hydrodynamic conditions is proposed in **Fig. 5-7**. Firstly, from **Fig. 5-7**. (c-I) and (c-II), it can be logically observed by the color intensity that increasing j_G (and thus L_B) under a given j_L leads to a rise in the average equivalent oxygen concentration fields in the

liquid slugs. The opposite effect is observed from **Fig. 5-7**. (b-I) and (c-I) for increasing j_L (and thus L_S) at a given j_G. Secondly, it is important to note that, at this axial position, which is close to the T-junction, the recirculation loops in the liquid slug are not yet fully established due to the contribution of the bubble formation step (entrance effect): they appear thus as asymmetrical or even undistinguishable at relatively large j_L. This is particularly true for small bubbles and long liquid slugs for which longer times are needed for the recirculation loops to be established. At relatively high axial locations, symmetrical recirculation loops can be observed (e.g. see **Fig. 5-8**, at X = 0.12 m).

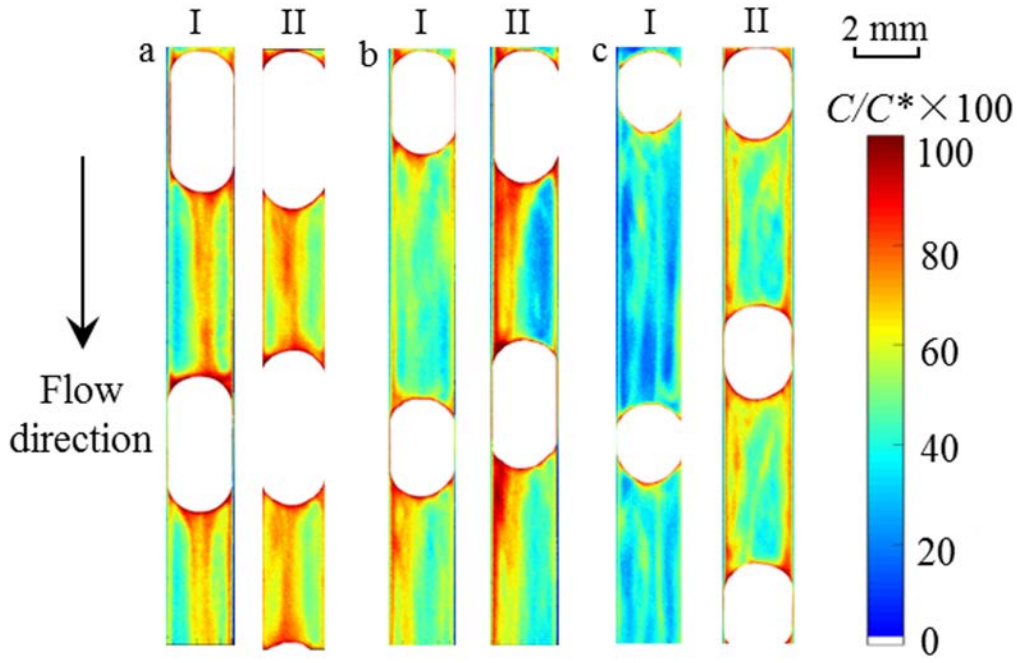

Fig. 5-7 Comparison of the equivalent oxygen concentration fields in the liquid slug under various operating conditions at X = 0.07 m: a) I. j_L = 0.069 m·s^{-1}, j_G = 0.042 m·s^{-1}; II. j_L = 0.069 m·s^{-1}, j_G = 0.069 m·s^{-1}; b) I. j_L = 0.139 m·s^{-1}, j_G = 0.042 m·s^{-1}; II. j_L = 0.139 m·s^{-1}, j_G = 0.069 m·s^{-1}; c) I. j_L = 0.208 m·s^{-1}, j_G = 0.042 m·s^{-1}; II. j_L = 0.208 m·s^{-1}, j_G = 0.069 m·s^{-1}.

Fig. 5-8 shows an example of the evolution of O_2 concentration fields in the liquid slug obtained at different axial positions (X = 0.02, 0.07, 0.12, at the bend, 0.20 and 0.32 m) along the

channel (j_L = 0.069 m·s^{-1}, j_G = 0.042 m·s^{-1}). It can be seen that the equivalent O_2 concentration level in the liquid slugs is getting greater and greater, until reaching an almost saturated state at X = 0.32 m. The apparent recirculation loops inside the liquid slugs can be clearly distinguished along the channel, except in the bend region. As far as the bubbles are flowing in the channel, the concentration fields become more and more uniform in the liquid slugs, namely for the higher axial locations, the liquid slugs become almost perfectly mixed.

In the bend region, due to the centrifugal effects induced by the channel curvature, the recirculation loops are twisted and split up. These distortions enable to enhance the mixing in the liquid slugs when compared to a purely straight channel section. In particular, the high amounts of oxygen accumulated in the front and at the rear of the bubble are progressively transported towards the liquid slug core when the bubbles travel in the bend. After the bend, the recirculation loops begin to establish again, and the symmetrical loops appears when X=0.32 m.

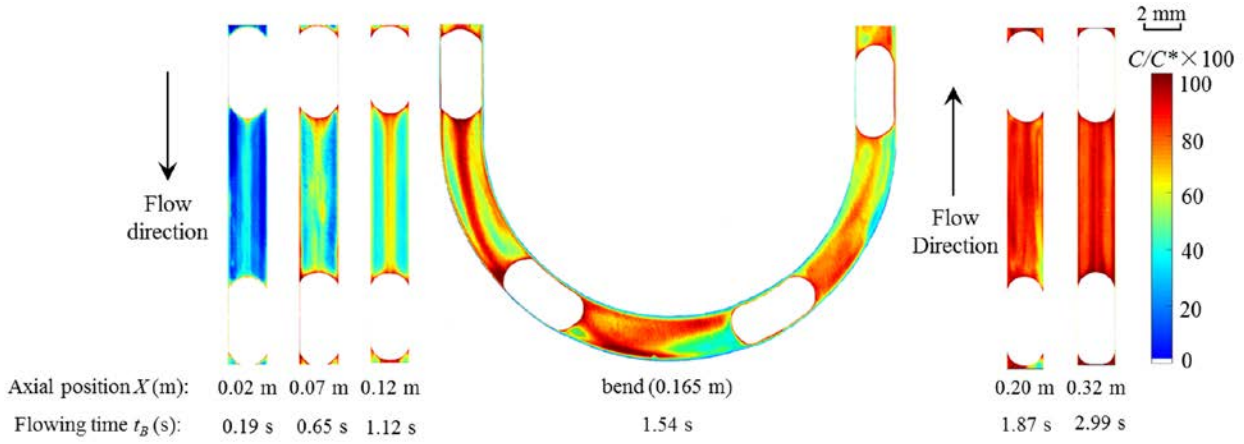

Fig. 5-8 Evolution of the equivalent oxygen concentration fields in the liquid slug as a function of the axial position in the straight channel. Operating condition: j_L = 0.069 m·s^{-1}, j_G = 0.028 m·s^{-1}.

For further insight, the temporal evolution of recirculation loops inside the liquid slugs is presented in **Fig. 5-9**. It can be showed that as the liquid slug passes through the bend, the recirculation patterns are significantly modified compared with those generated (symmetrical ones) in the straight section of the channel. The flow pattern becomes asymmetrical with the

recirculation loops positioned diagonally in the liquid slug, and the recirculation loop on the inner side of the bend has almost disappeared. The mixing inside the liquid slug looks intensified by passing the bend. As shown by **Fig. 5-10**, these phenomena are observed whatever the gas and liquid superficial velocities; nevertheless, they seem to be more pronounced when the liquid slug length decreases, typically see **Fig. 5-10** (a-I, II). It could be explained by the fact that the mixing times in the recirculation loops are shorter when liquid slugs are small. All these observations are in agreement with experimental and numerical works presented in the literature (Fries and von Rohr, 2009; Zaloha et al., 2012), which have also shown the effectiveness of these complex flow patterns for mixing inside the liquid slug.

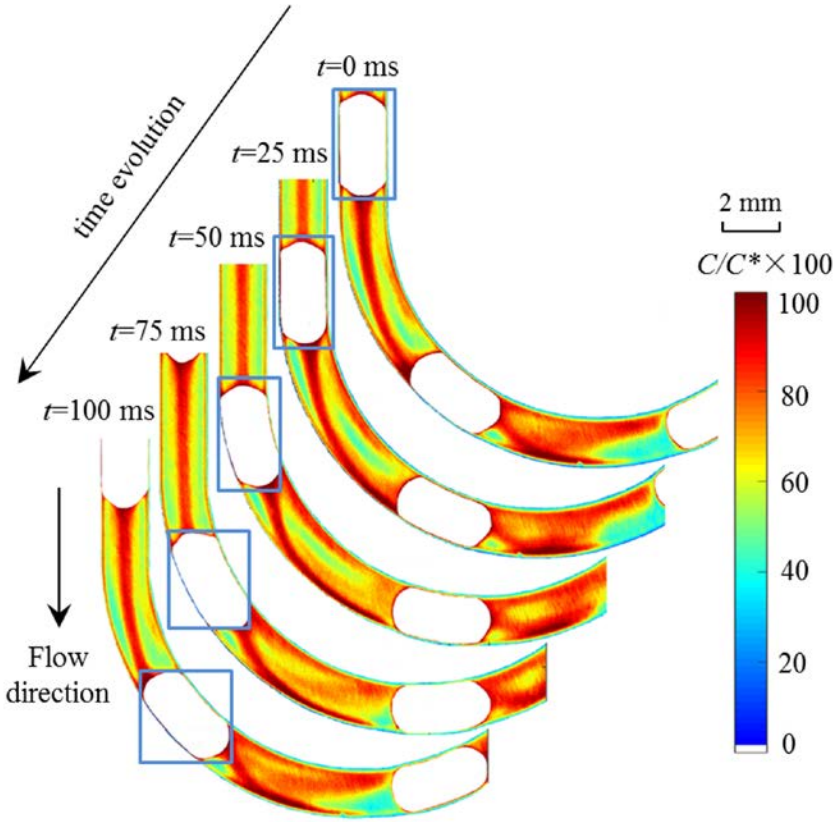

Fig. 5-9 Temporal evolution of the equivalent oxygen concentration fields in one liquid slug. Operating condition: j_L = 0.069 m·s^{-1}, j_G = 0.028 m·s^{-1}. t = 0 ms represents the moment when the entire bubble appears in the observed window. The bubble in the blue rectangle represents the bubble observed.

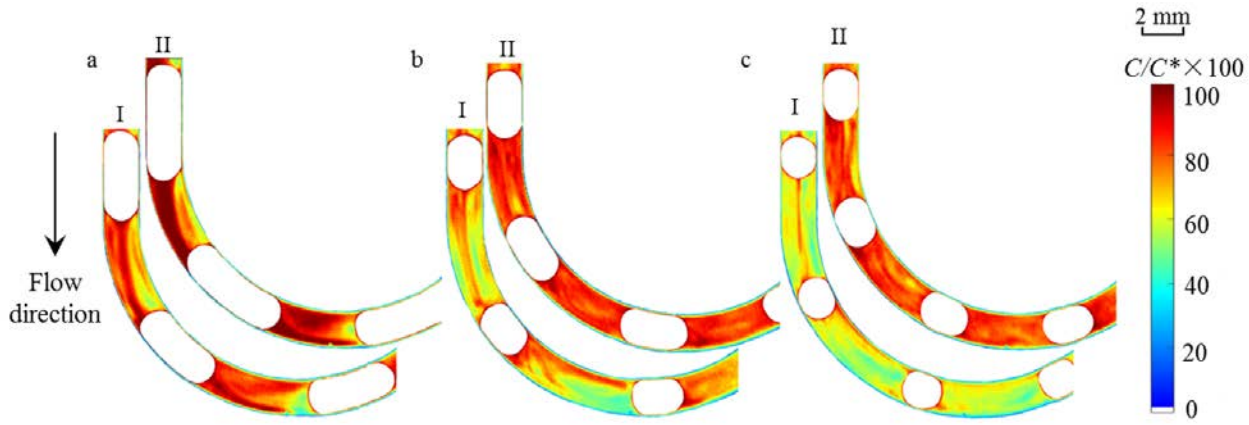

Fig. 5-10 Comparison of the equivalent oxygen concentration fields in the liquid slug under various operating conditions in the bend region: a) I. j_L = 0.069 m·s^{-1}, j_G = 0.042 m·s^{-1}; II. j_L = 0.069 m·s^{-1}, j_G = 0.069 m·s^{-1}; b) I. j_L = 0.139 m·s^{-1}, j_G = 0.042 m·s^{-1}; II. j_L = 0.139 m·s^{-1}, j_G = 0.069 m·s^{-1}; c) I. j_L = 0.208 m·s^{-1}, j_G = 0.042 m·s^{-1}; II. j_L = 0.208 m·s^{-1}, j_G = 0.069 m·s^{-1}.

5.3.2 Mass transfer coefficients

Fig. 5-11 shows the evolution of the normalized averaged O_2 concentration $\overline{C}/C^*$ (where $\overline{C}$ can be calculated by (Eq. 4-13) in the liquid slug as a function of the axial position X in the channel, under various j_L and at a given j_G =0.042 m·s^{-1}. It can be observed that $\overline{C}/C^*$ decreases as j_L increases under a given liquid superficial velocity, which is consistent with the visualization presented in **Fig. 5-7**. An almost linear relationship (deviation equal to be around 10%) between $\overline{C}/C^*$ and X can be observed from **Fig. 5-11** until X = 0.2 m, and according to (Eq. 3-2), the slope stands for $k_L a / j_L$. After X = 0.2 m, the deviation becomes higher than 14%; this can be due to the fact that, as shown in **Fig. 5-1**, this specific location corresponds to the big bend, namely to the location where the flow direction is changed in 180º. According to what was observed in **Fig. 5-8** and **Fig. 5-9**, when the bubbles are flowing along this bend, the recirculation loops in the liquid slugs are distorted, which would tend to favor the mixing in the liquid slugs. This was confirmed by Fries and von Rohr (2009) who investigated the velocity profile by μ-PIV technique and the mixing efficiency in the liquid slug of gas-liquid two-phase flow in an identical meandering channel with a similar geometric structure. They found that the mixing length could

be decreased by geometrical optimization to 12% compared to the straight channel design. In the present case, the eventual enhancement of the mixing in the liquid slug due the bend seems not to have an obvious influence on the gas-liquid mass transfer. Indeed, contrary to what was observed in the meandering channel (see **Fig. 4-12**. b), no strong change in the curve relating $\overline{C}/C^*$ to the axial position X is observed at the location of the bend (X=0.2 m). Further work should be required to understand this phenomenon, for example by carrying out experiments in a straight channel without a bend. At last, one can mention that the deviation between experimental data and the values predicted by (Eq. 3-2) can be also due to the assumptions linked to this model (see Chapter 3, section 3.1.3), in particular to the one related to a plug-flow behavior.

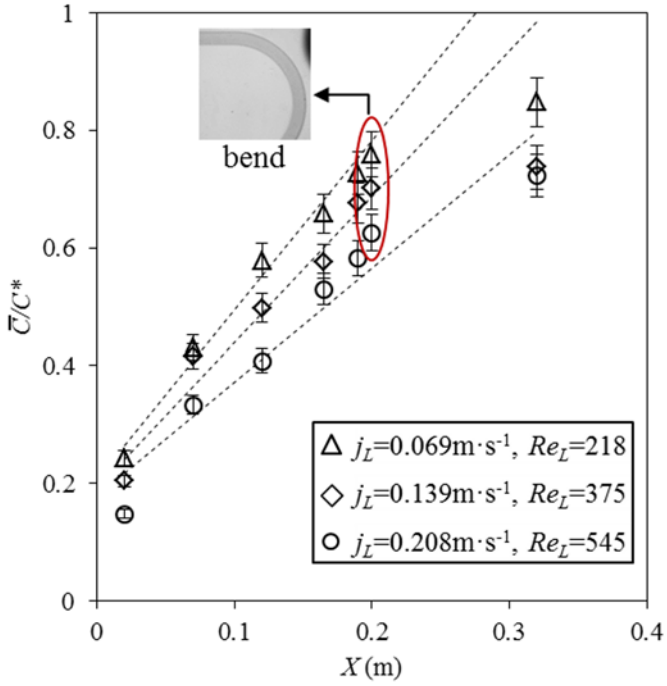

Fig. 5-11 Comparison of the evolution of normalized averaged oxygen concentration in the liquid slug along the channel with the ones predicted by the plug flow model under various liquid superficial velocities j_L at a given gas superficial velocity j_G = 0.042 m·s^{-1}.

The overall volumetric gas-liquid mass transfer coefficients, k_La, deduced from the fitting between (Eq. 3-2) with the experimental points just before the bend, are reported in **Table 5-1**. They are ranged from 0.1 to 0.5 s^{-1}, and compared with those obtained in the meandering channel,

the values of $k_L a$ are smaller (-12% on average). Such result would indicate that the meandering structure of the channel could intensify the gas-liquid mass transfer. At last, the liquid-side mass transfer coefficient before the bend k_L can be calculated by dividing $k_L a$ with a, displayed in **Table 5-1** (see in section 5.2.4). Compared with those obtained in Roudet et al. (2011) under the same operating conditions in straight channel, the values are in good accordance, which is a new proof of the reliability of the colorimetric technique. Most of the values of k_L in the meandering channel are always larger than those in the straight channel.

5.4 Comparison of mass transfer performances of straight and meandering channels

This section aims at rigorously comparing the gas-liquid mass transfer performances between straight and meandering channels, basing on relevant dimensionless numbers. For that, mass transfer efficiency (*E*) will be first compared by using the classical concept of Number of Transfer Units. Then, scaling laws (dimensionless relationships) will be established to predict the variations of the oxygen mass fluxes transferred as a function of the axial position and hydrodynamic conditions in both channels.

5.4.1 Mass transfer efficiency

To characterize the mass transfer efficiency, the concepts of Number of Transfer Units (NTU) and Height of Transfer Units (HTU) in macro-scale gas-liquid contactors could be implemented (Roudet et al., 2011), defined as below:

$$Z = NTU_G \times HTU_G = NTU_L \times HTU_L \qquad \text{(Eq. 5-7)}$$

where Z is the height of gas-liquid contactors. The liquid-side Number of Transfer Units, NTU_L represents the ratio between the residence time of the liquid phase t_r and the characteristic mass transfer time $t_{transfer}$ and can be defined by:

$$NTU_L = \frac{V / q_L}{1 / (k_L a)} = \frac{X / j_L}{1 / (k_L a)} = \frac{t_r}{t_{transfer}} \qquad \text{(Eq. 5-8)}$$

As shown from **Fig. 4-1** (b) and **Fig. 5-1**, both channels have the same compactness, but the meandering channel has a larger developed straight length than the straight channel due to the bends (1.37 m versus 1.01 m). As a consequence, to calculate NTU_L, the maximal observed position X have been considered, i.e. X = 0.32 m and 0.42 m for the straight and meandering channels, respectively. In **Fig. 5-12**. (a), the variation of NTU_L with j_G is plotted for each channel. It can be observed that $NTU_L < 1.1$ for both channels, indicating that in the present millimetric channels, $t_r < t_{transfer}$, which is contrary to commonly observed for macro-scale gas-liquid contactors. This clearly outlines that, even if millimetric channels enable gas-liquid intensification (higher $k_L a$), special attention should be paid for generating sufficient residence times, in particular in the perspective of implementing gas-liquid reactions. **Fig. 5-12** (a) also reveals that the meandering channel leads to higher NTU_L than in the straight channel, consequences of the fact that t_r and $k_L a$ are higher in meandering channel (see Eq. 5-8 and **Table 5-1**).

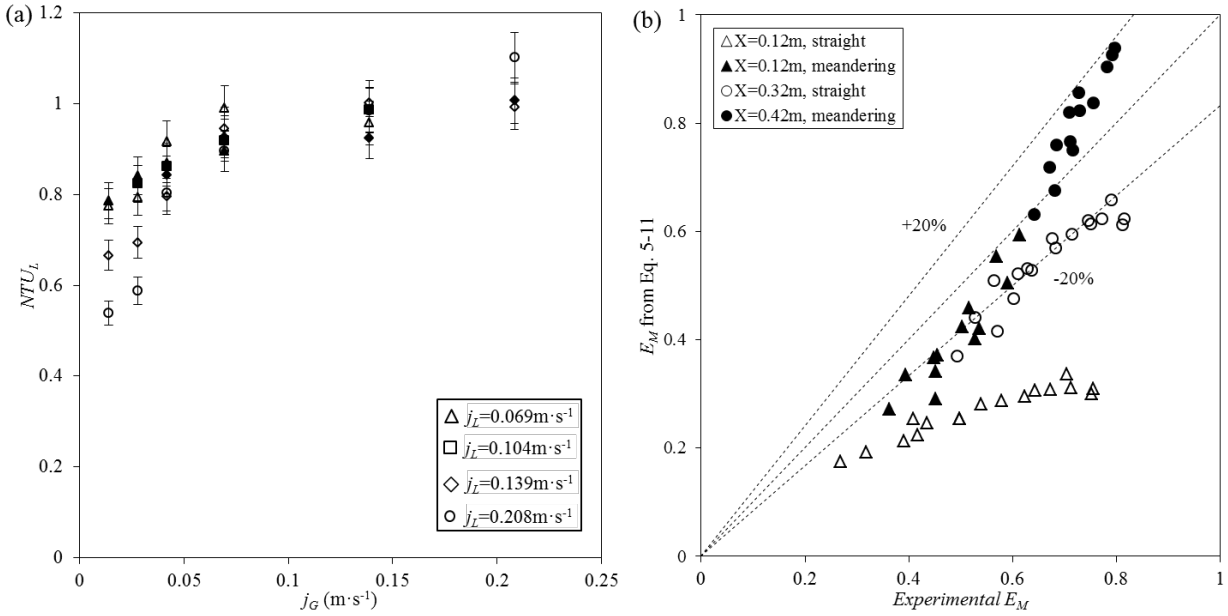

Fig. 5-12 (a) Number of Transfer Units in the liquid phase versus j_G. Empty and dark symbols correspond to the straight and meandering channels, respectively. (b) Comparisons between liquid absorption efficiencies measured and the ones calculated from Eq. (5-11).

According to Roustan (2003), NTU_L can be usually expressed as a function of the absorption ratio p and liquid efficiency E_M. For co-current absorption in macro-scale processes, by assuming plug flows for both liquid and gas phases, one finds

$$NTU_L = \frac{1}{1+p} \ln \frac{1}{1 - E_M \cdot (1+p)} \qquad \text{(Eq. 5-9)}$$

with:

$$p = \frac{L}{GM} \qquad \text{(Eq. 5-10)}$$

where L and G are the molar liquid and gas flow rates, respectively, and M the Henry's constant (M = 39950 at 293 K). The Murphree efficiency in the liquid phase is defined as:

$$E_M = \frac{x_{mol,ex} - x_{mol,in}}{x^*_{mol} - x_{mol,in}} \quad \text{(Eq. 5-11)}$$

where x_{mol} is the molar fraction of dissolved oxygen. Using concentrations instead of molar fractions and considering the oxygen concentration at the inlet equal to 0, (Eq. 5-11) turns to:

$$E_M = \frac{\overline{C}}{C^*} \quad \text{(Eq. 5-12)}$$

Combining (Eq. 5-9) and (Eq. 5-10), the liquid absorption efficiency E_M could be predicted for each operating condition. Comparisons between the experimental E_M and predicted ones at two positions (before the bend: X = 0.12 m for both channels; after the bend: X = 0.32 m and X = 0.42 m for the straight and meandering channels, respectively) are plotted in **Fig. 5-12** (b). It can be observed that:

- before the bend, the prediction quality in the straight channel is worse than that in the meandering channel. The explanation could be linked to the fact, for the straight channel, the flow is not yet established at this location (the recirculation loops in the liquid slugs are not symmetrical ,see **Fig. 5-7** and **Fig. 5-8**), whereas for the meandering channel, the liquid slugs can be considered as perfectly mixed just after several bends (see **Fig. 4-8** and **Fig. 4-9**);
- After the bend, good prediction qualities are observed in both channels. This could be attributed to the fact that the recirculation regions in the liquid slugs are well mixed after the “large” bend in both channels (see **Fig. 4-9** and **Fig. 5-8**).

Wherever the axial position, the mass transfer efficiency E_M is always significantly higher in the meandering channel than that in the straight channel (up to 0.8-0.9 against 0.55-0.65 for the higher location respectively).

5.4.2 Scaling laws

In the case of a confined bubble rising in a thin gap, Roudet et al. (2017) defined a Sherwood number Sh, as follows:

$$Sh_X = \frac{\varphi_{O_2} \cdot d_B}{D_{O_2} \cdot C_{O_2}^*} \quad \text{(Eq. 5-13)}$$

where $\varphi_{O_2}(X)$ is the mass flux of O_2 transferred per unit of bubble surface at a given X, which can be calculated by (Eq. 4-12), and d_B an equivalent diameter of the bubble,.

It is important at this level to remind that $\overline{C}$ represents the equivalent oxygen concentration in the liquid slugs. In the present study, the equivalent oxygen concentration in the liquid film located close to the walls has not been measured. This implies that the mass flux calculated according to (Eq. 4-12) corresponds a priori only to the amount of oxygen transferred from the front and the rear of the bubbles to the liquid slugs, suggesting thus that the contribution of the film would be not taken into account, except if there exists a direct mass flux exchange between the films and the slugs.

Fig. 5-13 illustrates the evolution of φ_{O_2} in the liquid slug as a function of X under various j_L at a given $j_G = 0.042\ \mathrm{m \cdot s^{-1}}$. It clearly appears that φ_{O_2} varies all along the channel length, and that higher values are observed for the axial positions close to the gas injection (X < 0.02 m). Such result is consistent with the findings presented in Chapter 3 (Yang et al., 2016), and obtained in the meandering channel (Chapter 4, see **Fig. 4-12**. a): it indicates the large contribution of bubble formation stage to the global mass transfer when compared to the flowing stage. Then, φ_{O_2} decreases significantly as the bubble moves along the straight channel, and seems to tend towards an almost constant value when the mass transfer becomes fully established.

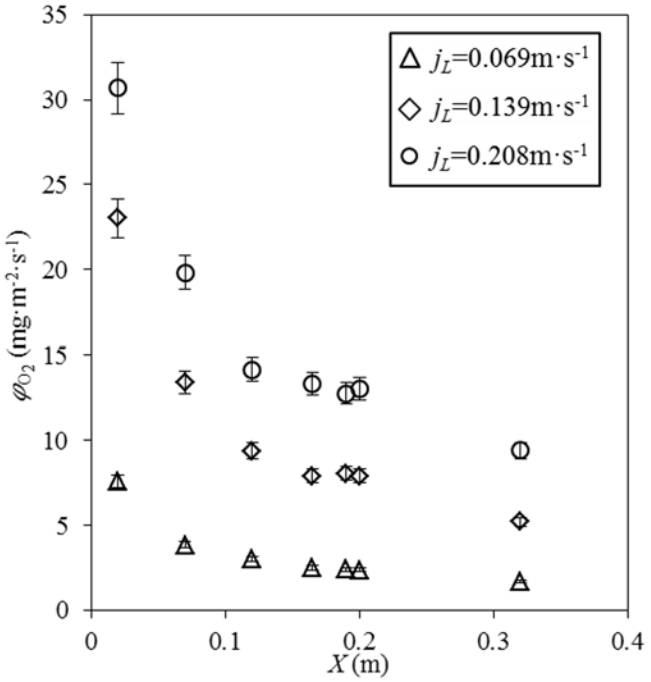

Fig. 5-13 Evolution of the mass flux of the transferred oxygen per unit of bubble surface φ_{O_2} as a function of the axial position X under various liquid superficial velocities j_L at a given j_G = 0.042 m·s^{-1}.

From these measured mass flux densities φ_{O_2} and considering as equivalent diameter d_B the bubble length L_B, the Sherwood number Sh_X can be calculated at a given location X, according to (Eq. 5-13). To correlate the variation of Sh_X with the axial distance X, the dimensionless Graetz number is introduced by analogy with heat transfer problems (Ko and Gau, 2011); it is defined by:

$$Gz_X = \frac{l}{X} \cdot Re_B \cdot Sc = \frac{l}{X} \cdot Pe \qquad \text{(Eq. 5-14)}$$

where l is the channel width, Re_B the bubble Reynolds number, defined as $Re_B = \frac{\rho_L \cdot L_B \cdot U_B}{\mu_L}$; Sc the Schmitt number, defined as $Sc = \frac{\mu_L}{\rho_L \cdot D_{O_2}}$. The product of Re_B and Sc is equal to the Péclet number Pe.

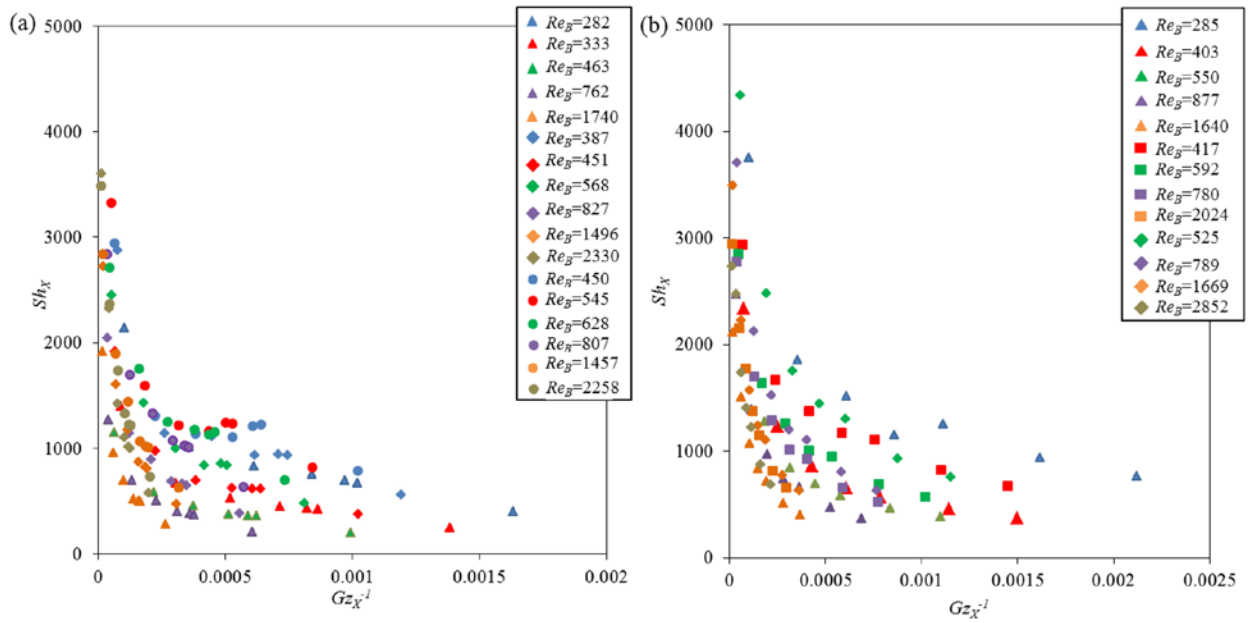

Fig. 5-14 Evolution of the experimental local dimensionless Sherwood number as a function of the dimensionless Graetz number: (a) in the straight channel; (b) in the meandering channel. Triangle marks represent the operating conditions under a given liquid superficial velocity j_L=0.069 m·s^{-1}; square marks under j_L=0.104 m·s^{-1}; diamond marks under j_L=0.139 m·s^{-1}; circle marks under j_L=0.208 m·s^{-1}.

Fig. 5-14 reports the evolution of Sh_X as a function of Gz_X^{-1} in both channels. Whatever the Reynolds number Re, Sh_X shows an identical trend, characterized by relatively high values at the beginning (i.e. to the axial positions close to the gas injection, X < 0.02 m). This phenomenon is fully consistent with **Fig. 5-13**, and indicates the large contribution of bubble formation stage. Then, Sh_X decreases significantly with Gz_X^{-1} (i.e. when the bubbles are flowing along the channel), and tends towards an almost constant value when the mass transfer regime is fully

established. The data of Sh_X as a function of Gz_X under all operating conditions in both channels are displayed in **Table B-1** and **Table B-2**.

Fig. 5-14 also shows the dispersion of the values of Sh_X depending on the operating conditions (gas and liquid flow rates). To group together all the points, it is chosen to introduce the dimensionless number $\frac{L_S}{l}$ in the scaling law, and to impose the exponents of Gz_X and Pe to 0.5 according to the literature (Abiev and Lavretsov, 2012; Kastens et al., 2015; Roudet et al., 2017). This leads to the following scaling laws:

- for straight channel:

$$Sh_X = 3.54 \cdot Gz_X^{0.5} \cdot \left(\frac{L_S}{l}\right) + 0.44 \cdot Pe^{0.5}, \text{ mean deviation: 16.5\%} \quad \text{(Eq. 5-15)}$$

- for meandering channel:

$$Sh_X = 5.23 \cdot Gz_X^{0.5} \cdot \left(\frac{L_S}{l}\right) + 0.48 \cdot Pe^{0.5}, \text{ mean deviation: 18.2\%} \quad \text{(Eq. 5-16)}$$

Note that the occurrence of the turning points has no major impact on the scaling laws. The constants in these two equations indicate that, under the same Gz_X, $\frac{L_S}{l}$, Pe, Sh_X are higher in the meandering channel (5.23 and 0.48) than that in the straight channel (3.54 and 0.44). The comparison between the experimental Sh_X and the predicted ones in both channels, reported in **Fig. 5-15**, shows the good fitting qualities.

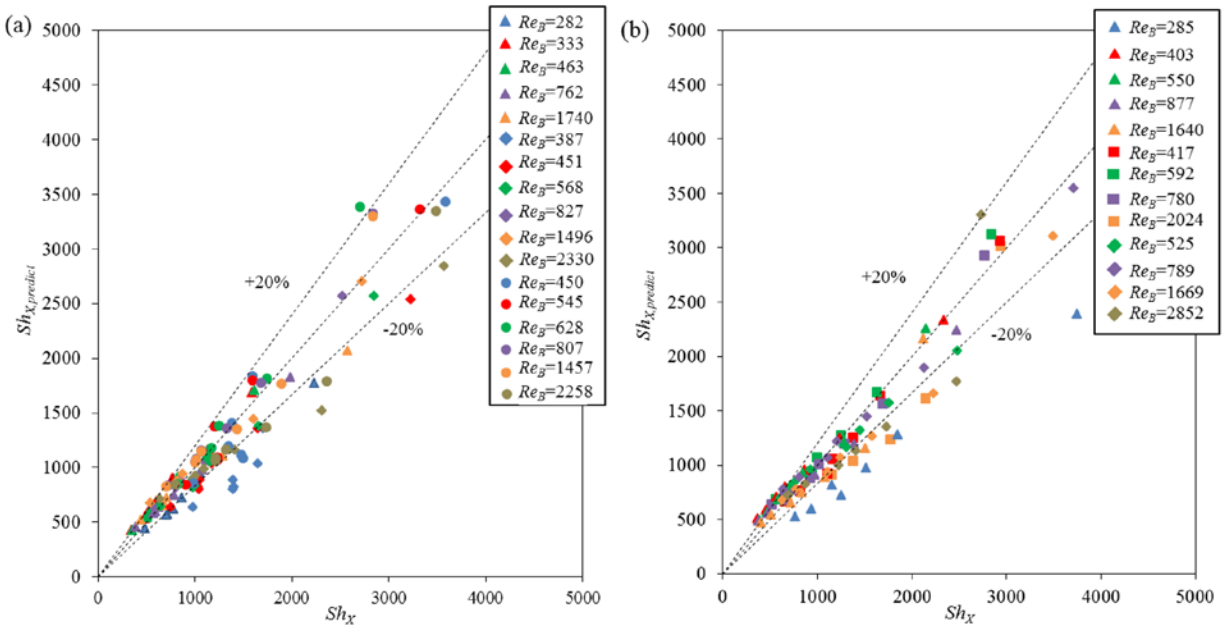

Fig. 5-15 Comparison of the experimental local dimensionless Sherwood number with the predicted ones: (a) in straight channel; (b) in meandering channel. Triangle marks represent the operating conditions under a given liquid superficial velocity j_L=0.069 m·s^{-1}; square marks under j_L=0.104 m·s^{-1}; diamond marks under j_L=0.139 m·s^{-1}; circle marks under j_L=0.208 m·s^{-1}.

These scaling laws ((Eq. 5-15) and (Eq. 5-16)) are composed by two terms. (1) The first term, involving the Graetz number Gz_X (thus the axial position X), represents the contribution of the bubble formation stage to the overall mass transfer, or in other words, the entrance effects. It can be deduced that the entrance effect is 1.5 time larger in the meandering channel than in the straight channel. (2) The second term, involving the Péclet number Pe, is constant at a given operating condition, and corresponds to the fully established mass transfer regime far from the entrance. It can be deduced that Sh_X for the full established regime in the meandering channel is 1.1 time larger than in the straight channel at a given Pe. All these show that the geometry effect seems to be more important at the entrance than for the full established mass transfer regime (1.5 time compared to 1.1 time). In addition, the first term in both the straight and meandering channels is always higher than the second term, which indicates the considerable contribution of the bubble formation stage to the overall mass transfer.

For each channel, one can thus define a critical location X (provided that no mass transfer limitation exists, i.e. no saturation limitation), after which Sh_X tends towards an infinite value, noted as Sh_∞. This infinite Sherwood number Sh_∞ is reached when the contribution of bubble formation stage to the mass transfer become negligible compared to the global mass transfer. From the scaling laws (Eq. 5-15 and Eq. 5-16), it can be known that the values of Sh_∞ in the meandering channel are slightly higher (+8% on average) than those in the straight channel, confirming again that the gas-liquid mass transfer could be intensified by using the meandering structure of the channel.

From the latter results, one can calculate, as in Chapter 3, the mass amount fraction ϕ (see Eq. 3-4). This ratio compares the amounts of transferred oxygen right after the pinch-off and for the complete unit cell flowing at a static location equal to 14 times the channel width from the junction where the two phases began to contact in the microreactor. The mass amount fraction ϕ can be predicted as follow:

$$\phi = \frac{m_{O_2}}{m_{O_2}'} = \frac{\varphi_{O_2} \cdot t_B}{\varphi_{O_2}' \cdot t_B'} = \frac{Sh_X \cdot t_B}{Sh_{X'} \cdot t_B'} \qquad \text{(Eq. 5-17)}$$

where φ_{O_2} and t_B are the mass flux of transferred O_2 per unit of bubble surface and the related time at the bubble pinch-off, respectively; φ_{O_2}' and t_B' at the position when the bubble reaches a static location equal to 14 times the channel width from the inlet. Sh_X and $Sh_{X'}$ are calculated from (Eq. 5-15).

The predicted mass amount fraction ϕ ranges from 46% to 58%, which have the same order of magnitude than the experimental values obtained in Chapter 3 with a channel cross-section equal to 500×500 µm^2 equipped with a flow-focusing injection (see **Fig. 3-1**). The slight underestimation of the predicted fractions ϕ can be explained by the fact that the present scaling law (Eq. 5-15) was established for the millimetric channel, and that the geometries of the inlet in each channel are also different (T-junction versus flow-focusing).

5.5 Conclusion

In this chapter, the comparison of gas-liquid hydrodynamics and mass transfer characteristics was performed between straight and meandering geometries of channels, aiming at evaluating the benefits of meandering geometry with respect to straight channel.

From the hydrodynamics' point of view, one should remember that: (1) the transition from Taylor flow regime to slug-flow regime was delayed in the straight channel when compared to the meandering channel. (2) the deformation of bubble from hemispherical ends to a more slender/flatter shape of nose/rear occurred approximately at We=1.5, and was accentuated by the action of gravity and, in the meandering channel, by the presence of centrifugal forces. (3) Using a meandering channel instead of a straight channel enabled a slight rise in bubble lengths (+7% on average) and larger liquid slug lengths (+16% on average). (4) Whatever the channel, the bubble velocities were always larger than the total superficial velocities, demonstrating that a slip phenomenon between the bubbles and the liquid film took place. (5) The interfacial areas were slightly increased by 8% on average by using the meandering channel.

From the mass transfer's point of view, one should remember that: (1) the volumetric mass transfer coefficient k_La was increased by 12% on average in the meandering channel. (2) The Number of Transfer Units in the liquid phase (NTU_L) were higher in the meandering channel and remained close to one due to insufficient residence times. (3) Original scaling laws were proposed to predict the variations of the oxygen mass fluxes transferred (via the Sherwood number Sh) as a function of the axial position (via the Graetz number Gz) in both channels and for different operating conditions. The geometry effect (meandering or straight) seems to be more important at the entrance than for the full established mass transfer regime (1.5 time compared to 1.1 time). The constants in the two scaling laws indicate that Sh_X were higher in the meandering channel (5.23 and 0.48) than that in the straight channel (3.54 and 0.44) under the same Gz_X, $\frac{L_S}{l}$ and Pe. When the contribution of bubble formation stage to the mass transfer became negligible when compared to the global mass transfer, a so-called infinite Sherwood number, Sh_∞, could be obtained and its dependency to the Péclet number was established. The values of Sh_∞ in the

meandering channel were slightly higher (+8% on average) than those in the straight channel. All these findings confirm that the gas-liquid mass transfer could be intensified by using the meandering structure of the channel.

CHAPTER 6

Conclusion and outlook

6.1 General conclusion of the thesis

The global objective of this thesis was to locally visualize and characterize the gas-liquid mass transfer around Taylor bubbles flowing in meandering millimetric channels constituting HEX reactors, by using the colorimetric technique proposed by Dietrich et al. (2013). The underlying scientific question was to better understand how and why such meandering geometry of channel enables to intensify gas-liquid mass transfer when compared with the straight one.

First of all, the occurrence of a possible enhancement of the gas-liquid mass transfer by the reaction involved was studied as this technique is a chemical method. For that, the parameters concerning the kinetics of the reaction and the diffusion coefficients of both oxygen and dihydroresorufin into the liquid were determined by implementing optical methods in microfluidic devices and coupling them with modeling approaches. The knowledge of these parameters enabled to calculate the Hatta number *Ha* and the enhancement factor *E* associated with the colorimetric reaction, as well as providing the guidelines to evaluate the conditions required to implement the colorimetric method at other scales or in other gas-liquid systems.

Secondly, the feasibility of the technique at microscale was demonstrated. For that, a special focus was made on the study of the gas-liquid mass transfer occurring in Taylor flows right after the bubble pinch-off in a flow-focusing microreactor (with a channel cross-section equal to 500×500 μm^2). The important contribution of mass transfer right after the bubble formation stage to the overall gas-liquid mass transfer was quantified, which constituted an original result when compared to the state-of-art.

Then, the colorimetric method was implemented in a meandering millimetric square channel (channel cross-section equals to 2×2 mm^2) to locally visualize and characterize the gas-liquid mass transfer around Taylor bubbles flowing inside. The gas-liquid hydrodynamics were

beforehand characterized, in particular in terms of bubble and slug lengths, bubble velocity, gas hold-up, interfacial area. The evolution of the equivalent O_2 concentration fields in the liquid slugs passing through one and several bends were described as well as the influence of the "turning point" joining two "straight" sections of the meandering channel.

At last, the performances between the straight and meandering channel were rigorously compared by carrying out specific experiments in a straight channel, whose channel cross-section and compactness were identical to those of the meandering channel.

In the following subsections, the main findings will be summarized.

6.1.1 Hatta number and enhancement factor of the colorimetric reaction

Under the classical conditions where the colorimetric technique was implemented in millimetric channels (resazurin concentration: C_{Bb} = 0.1 g·L^{-1}, liquid side mass transfer coefficient: k_L close to 10^{-4} m·s^{-1}), the Hatta number *Ha* was found to be equal to 14.4, and the enhancement factor *E* to 1.03. This demonstrated that, even if the colorimetric reaction was fast, and even quasi-instantaneous, there was no enhancement of the gas-liquid mass transfer by the reaction. Such a result was opposite to the general knowledge that high Ha lead to high E; it was the consequence of the fact that the diffusion of the dye (dihydroresorufin) in the liquid film was very slow (D_B = 8.65×10^{-11} m^2·s^{-1}) when compared to the diffusion of oxygen (D_{O_2} = 3.2×10^{-9} m^2·s^{-1}), thus preventing the reaction to occur in the liquid film.

For the implementation of the colorimetric technique at other scales or in other gas-liquid systems, a special care should be taken to choose the initial concentration of resazurin. For this purpose, some guidelines were established, as presented in Chapter 1 (section 1.3) and in Chapter 2 (section 2.5) (note that the solubility of resazurin in water is limited to 1 g·L^{-1}). It became now possible to calculate the Hatta number *Ha* by (Eq. 2-9) and the knowledge acquired on the reaction constant k_2, the diffusion coefficient of oxygen D_{O_2}, and k_L of the system under test. Knowing the value of Ha, the enhancement factor E could be further calculated. When Ha>3, the magnitude of k_L for implementing this colorimetric technique should be approximately below

1.41×10^{-3} $m\cdot s^{-1}$, and a maximum value of 1.23 was found for E (i.e. when the initial concentration of resazurin was equal to its solubility), using (Eq. 2-13) and (Eq. 2-14). In this case, an enhancement of the mass transfer by the reaction existed, but it could be quantified and the experimental values of mass transfer coefficient could be indeed corrected by E to obtain the intrinsic k_L.

6.1.2 Contribution of the bubble formation stage to the overall mass transfer in microreactors

The results obtained showed that the bubble formation stage made a reasonably large contribution to the overall mass transfer related to a relatively short bubble formation times (4.75-10.50 ms). The mass transfer amount fraction ϕ, which was defined by the ratio between the amount of transferred O_2 in the liquid slug right after the pinch-off and for the complete unit cell flowing at a static location equal to 14 times the channel width, could be quantified. It was ranged from 45 to 90%; at a given j_G, ϕ slightly increased when rising j_L, and for a given j_L, ϕ seemed to globally increase as j_G increases. The scaling laws proposed in Chapter 5 (see Eq. 5-15) in the straight millimetric channel was used to predict ϕ. It led ϕ ranging from 46 to 58%: this difference can be explained by the different scales of the system under study (micro/milli scale), and the different geometries of the inlet (flow-focusing/T-junction).

All these findings gave important information to understand the contributions of the bubble formation stage to the overall gas-liquid mass transfer occurring in a microchannel. In the future, they could serve as basis for elaborating a complete model, accounting for the bubble formation stage.

6.1.3 Effect of the meandering geometry on the gas-liquid mass transfer mechanism

In the meandering channel, the recirculation loops classically observed inside the liquid slugs were observed to be no more symmetrical. They were indeed twisted and split by the periodic

bends, and tended to disappear as the bubble moved within the channel; the O_2 concentration inside the liquid slug became uniform after passing through several bends (around 20 bends): the gradient of O_2 concentration within the liquid slug no longer existed. The accumulation of O_2 at the front and at the rear of the bubble could be observed along the first bends, and tended to disappear, as well as the recirculation zones, for the higher axial locations, namely when the liquid slugs became almost perfectly mixed. The existence of the first bend showed a slowed-down mass transfer due to the mixing effect which could decrease the average driving force in the liquid slugs. The occurrence of the "turning point" (i.e. the big bend enabling the flow direction in 180°) seemed to induce a slowing down of the mass transfer, especially when $Re >$ 300 and $Ca > 0.002$. The mass flux of O_2 transferred per unit of bubble surface was significantly higher close to the gas injection due to the important contribution of the bubble formation stage, then it decreased significantly as the bubble flowed along the meandering channel, and became small after $X = 0.3$ m due to the decreasing driving force for the mass transfer.

6.1.4 Benefits of the meandering geometry with respect to straight one on the performance of gas-liquid mass transfer

The results obtained in this thesis revealed that using the meandering geometry instead of a straight is an efficient method to increase the volumetric mass transfer coefficient $k_L a$ by 12% on average, as well as the mass transfer efficiency E_M. This indicated that the meandering geometry of the channel could intensify the mass transfer. It was also showed that the Number of Transfer Units in the liquid phase (NTU_L), which represented the ratio between the residence time of liquid phase and the characteristic mass transfer time, remained low (close to one) in both straight and meandering channels used; thus, even if the millimetric channels allowed gas-liquid mass transfer intensification when compared to the conventional gas-liquid contactors, one should keep in mind the need to generate sufficient residence times.

At last, original scaling laws were proposed to predict the variations of the oxygen mass fluxes transferred (via the Sherwood number *Sh*) as a function of the axial position (via the Graetz number *Gz*) in both channels and for different operating conditions (via the Reynolds and

Peclet numbers). The values of the first term in the scaling law which represented the contribution of the bubble formation stage to the overall mass transfer were always larger than those of the second term which was constant at a given operating condition, and corresponded to the fully established mass transfer regime far from the entrance. It demonstrated that the considerable contribution of the bubble formation stage to the overall mass transfer in our case. The geometry effect seemed to be more important at the entrance than for the full established mass transfer regime (1.5 time compared to 1.1 time). When the contribution of bubble formation stage to the mass transfer (i.e. the inlet effects) became negligible when compared to the global mass transfer, a so-called infinite Sherwood number, Sh_{∞}, could be obtained and its dependency to the Péclet number was established. The values of Sh_{∞} in the meandering channel were found to be slightly higher (+8% on average) than those in the straight channel, which confirmed that the gas-liquid mass transfer could be intensified by using the meandering structure of the channel.

6.2 Outlook

In this section, as further developments of this thesis, several possibilities are proposed.

- This work should be completed for improving the understanding of the present results; in particular the contribution of the liquid film (not quantified in this study) should be imperatively addressed and the effect of the turning point more precisely quantified, so as to improve its design. This will require also specific experiments (μPIV) and/or numerical simulations to be carried out for accessing local velocity field in the liquid slugs. A deeper knowledge of the liquid flow structure would clearly help to understand the distortions of the recirculation loops in the bends, and so the exact mass transfer mechanism. The influence of fluid properties (viscosity, surface tension, etc.) on mass transfer will be also an important point to investigate in the future.

- The present technical limitations, such as the illumination system and the resolution of the camera, should be overcome to access to the equivalent oxygen concentration fields in the liquid film. This will be essential to know if the saturation of oxygen is reached or not in the film, and

thus if the contribution of the liquid film to the gas-liquid mass transfer is (or is not) considerable compared to the mass transfer in the liquid slugs.

- As resazurin is a fluorescent dye, which presents a maximum absorption at wavelength equals 572 nm, and maximum emission at 600 nm, it could be interesting to implement laser to visualize and characterize the concentration fields at each *xy*-plane along the channel height, as well as in the areas around the hemispheric rear and nose of the Taylor bubbles in order to reach a 3D characterization. Such implementations would make possible to appreciate the axisymmetric character of the concentration fields.

- Another fluorescent dye, such as indigo carmine, could be interesting to be used to visualize and characterize the oxygen mass transfer. As in the oxidized form (when the saturation in oxygen is not reached), indigo carmine is characterized by an intensity red color (from yellow to red); if the amount of transferred oxygen increases (almost reach the saturation), indigo carmine becomes green (from red to green). This feature would enable indigo carmine to be an efficient indicator for direct visualization of the saturation extent of the transferred oxygen along the channel.

- The gas-liquid mass transfer could be investigated in other geometries of milli/microsystem by the implementation of the colorimetric technique, for example in the spiral-shaped microreactor used for flow photochemistry studies (Aillet et al., 2016), in helical reactors (Kurt et al., 2017), and in other meandering configurations, illustrated as below in **Fig. 6-1**. Original scaling laws could be also established to predict the mass transfer performances depending on the geometry.

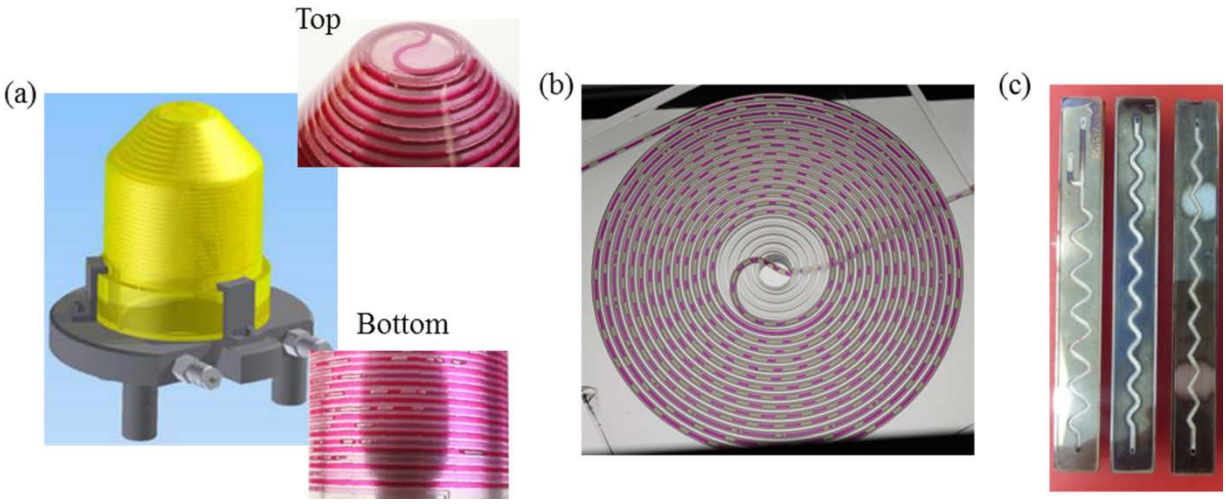

Fig. 6-1 Illustration of: (a) helical reactor; (b) spiral-shaped microreactor; (c) different meandering channels, adapted from Dai et al. (2015).

REFERENCES

Abadie, T., Aubin, J., Legendre, D., Xuereb, C., 2012. Hydrodynamics of gas–liquid Taylor flow in rectangular microchannels. Microfluid. Nanofluidics 12, 355–369.

Abadie, T., Xuereb, C., Legendre, D., Aubin, J., 2013. Mixing and recirculation characteristics of gas–liquid Taylor flow in microreactors. Chem. Eng. Res. Des. 91, 2225–2234.

Abiev, R.S., Lavretsov, I. V., 2012. Intensification of mass transfer from liquid to capillary wall by Taylor vortices in minichannels, bubble velocity and pressure drop. Chem. Eng. Sci. 74, 59–68.

Aillet, T., Loubière, K., Dechy-Cabaret, O., Prat, L., 2016. Microreactors as a Tool for Acquiring Kinetic Data on Photochemical Reactions. Chem. Eng. Technol. 39, 115–122.

Ambrosini, D., Paoletti, D., Rashidnia, N., 2008. Overview of diffusion measurements by optical techniques. Opt. Lasers Eng. 46, 852–864.

Anderson, L., Wittkopp, S.M., Painter, C.J., Liegel, J.J., Schreiner, R., Bell, J.A., Shakhashiri, B.Z., 2012. What Is Happening When the Blue Bottle Bleaches: An Investigation of the Methylene Blue-Catalyzed Air Oxidation of Glucose. J. Chem. Educ. 89, 1425–1431.

Anxionnaz-Minvielle, Z., Cabassud, M., Gourdon, C., Tochon, P., 2013. Influence of the meandering channel geometry on the thermo-hydraulic performances of an intensified heat exchanger/reactor. Chem. Eng. Process. Process Intensif. 73, 67–80.

Anxionnaz, Z., 2009. Etude de l’influence de la géométrie des canaux sur les performances d’un réacteur/échangeur. University of Toulouse.

Anxionnaz, Z., Cabassud, M., Gourdon, C., Tochon, P., 2008. Heat exchanger/reactors (HEX reactors): Concepts, technologies: State-of-the-art. Chem. Eng. Process. Process Intensif. 47, 2029–2050.

Astaria, G., Savage, D.W., Bisio, A., 1983. Gas treating with chemical solvents. J. Wiley and Sons,New York.

Benbelkacem, H., 2002. Modélisation du transfert de matière couplé avec une réaction chimique en réacteur fermé. INSA Toulouse.

Berčič, G., Pintar, A., 1997. The role of gas bubbles and liquid slug lengths on mass transport in the Taylor flow through capillaries. Chem. Eng. Sci. 52, 3709–3719.

Butler, C., Cid, E., Billet, A.-M., 2016. Modelling of mass transfer in Taylor flow: Investigation with the PLIF-I technique. Chem. Eng. Res. Des. 115, 292–302.

Canny, J., 1986. A Computational Approach to Edge Detection. IEEE Trans. Pattern Anal. Mach. Intell. PAMI-8, 679–698.

Commenge, J.-M., Falk, L., 2014. Methodological framework for choice of intensified equipment and development of innovative technologies. Chem. Eng. Process. Process Intensif. 84, 109–127.

Crank, J., 1975. The mathematics of diffusion, 2nd ed. Clarendon Press, Oxford, England.

Culbertson, C., 2002. Diffusion coefficient measurements in microfluidic devices. Talanta 56, 365–373.

Dai, Z., Fletcher, D.F., Haynes, B.S., 2015a. Influence of Tortuous Geometry on the Hydrodynamic Characteristics of Laminar Flow in Microchannels. Chem. Eng. Technol. 38, 1406–1415.

Dai, Z., Fletcher, D.F., Haynes, B.S., 2015b. Impact of tortuous geometry on laminar flow heat transfer in microchannels. Int. J. Heat Mass Transf. 83, 382–398.

Darvas, F., Dorman, G., Hessel, V., 2014. Flow chemistry. Boston : De Gruyter Textbook, Berlin.

Dessimoz, A.-L., Raspail, P., Berguerand, C., Kiwi-Minsker, L., 2010. Quantitative criteria to define flow patterns in micro-capillaries. Chem. Eng. J. 160, 882–890.

Dietrich, N., Loubière, K., Jimenez, M., Hébrard, G., Gourdon, C., 2013a. A new direct technique for visualizing and measuring gas–liquid mass transfer around bubbles moving in a straight millimetric square channel. Chem. Eng. Sci. 100, 172–182.

Dietrich, N., Mayoufi, N., Poncin, S., Midoux, N., Li, H.Z., 2013b. Bubble formation at an orifice: A multiscale investigation. Chem. Eng. Sci. 92, 118–125.

Dietrich, N., Poncin, S., Midoux, N., Li, H.Z., 2008. Bubble Formation Dynamics in Various Flow-Focusing Microdevices. Langmuir 24, 13904–13911.

Dong, Z., Yao, C., Zhang, Y., Chen, G., Yuan, Q., Xu, J., 2016. Hydrodynamics and mass transfer of oscillating gas-liquid flow in ultrasonic microreactors. AIChE J. 62, 1294–1307.

Elgue, S., Aillet, T., Loubiere, K., Conté, A., Dechy-Cabaret, O., Prat, L., Horn, C.R., Lobet, O., Vallon, S., 2015. Flow photochemistry: A meso-scale reactor for industrial applications. Chim. Oggi/Chemistry Today 33, 58–61.

Erb, R.E., Ehlers, M.H., 1950. Resazurin Reducing Time as an Indicator of Bovine Semen Fertilizing Capacity. J. Dairy Sci. 33, 853–864.

Falk, L., Commenge, J.-M., 2010. Performance comparison of micromixers. Chem. Eng. Sci. 65, 405–411.

Fehling, H., 1849. Die quantitative Bestimmung von Zucker und Stärkmehl mittelst Kupfervitriol. Ann. der Chemie und Pharm. 72, 106–113.

Fick, A., 1855. Ueber Diffusion. Ann. der Phys. und Chemie 170, 59–86.

Fries, D.M., von Rohr, P.R., 2009. Liquid mixing in gas–liquid two-phase flow by meandering microchannels. Chem. Eng. Sci. 64, 1326–1335.

Fries, D.M., Waelchli, S., Rudolf von Rohr, P., 2008. Gas–liquid two-phase flow in meandering microchannels. Chem. Eng. J. 135, S37–S45.

Günther, A., Khan, S. a, Thalmann, M., Trachsel, F., Jensen, K.F., 2004. Transport and reaction in microscale segmented gas-liquid flow. Lab Chip 4, 278.

Galambos, P., Forster, F.K., 1998. Micro-Fluidic Diffusion Coefficient Measurement, in: Harrison, D.J., Berg, A. van den (Eds.), Micro Total Analysis Systems ’98. Springer Netherlands, Dordrecht, pp. 189–192.

Garstecki, P., Fuerstman, M.J., Stone, H. a, Whitesides, G.M., 2006. Formation of droplets and bubbles in a microfluidic T-junction—scaling and mechanism of break-up. Lab Chip 6, 437.

Giavedoni, M.D., Saita, F.A., 1999. The rear meniscus of a long bubble steadily displacing a Newtonian liquid in a capillary tube. Phys. Fluids 11, 786.

Gourdon, C., Elgue, S., Prat, L., 2015. What are the needs for Process Intensification? Oil Gas Sci. Technol. – Rev. d'IFP Energies Nouv. 70, 463–473.

Günther, A., Jhunjhunwala, M., Thalmann, M., Schmidt, M.A., Jensen, K.F., 2005. Micromixing of Miscible Liquids in Segmented Gas−Liquid Flow. Langmuir 21, 1547–1555.

Günther, A., Khan, S. a, Thalmann, M., Trachsel, F., Jensen, K.F., 2004. Transport and reaction in microscale segmented gas–liquid flow. Lab Chip 4, 278–286.

Haase, S., Bauer, T., 2011. New method for simultaneous measurement of hydrodynamics and reaction rates in a mini-channel with Taylor flow. Chem. Eng. J. 176–177, 65–74.

Haase, S., Murzin, D.Y., Salmi, T., 2016. Review on hydrodynamics and mass transfer in minichannel wall reactors with gas–liquid Taylor flow. Chem. Eng. Res. Des. 113, 304–329.

Haghnegahdar, M., Boden, S., Hampel, U., 2016. Mass transfer measurement in a square milli-channel and comparison with results from a circular channel. Int. J. Heat Mass Transf. 101, 251–260.

Hauf, W., Grigull, U., 1970. Optical methods in heat transfer, in: Hartnett, J.P., Thomas F, Irvine, J. (Eds.), Advances in Heat Transfer, Vol. 6. Academic Press, New York.

Hecht, K., Kraut, M., Kölbl, A., 2007. Microstructured mixing devices: an efficient tool for the determination of chemical kinetic data? AIChE. Spring Meet. Houston, Texas, USA 22–26.

Hessel, V., Angeli, P., Gavriilidis, A., Löwe, H., 2005. Gas−Liquid and Gas−Liquid−Solid Microstructured Reactors: Contacting Principles and Applications. Ind. Eng. Chem. Res. 44, 9750–9769.

Hesselgreaves, J.E., Richard, L., David, R., 2016. Compact Heat Exchangers: Selection, Design and Operation. Butterworth-Heinemann.

Higbie, R., 1935. The rate of absorption of a pure gas into still liquid during short periods of exposure. Inst. Chem. Eng. 35, 36–60.

Hikita, H., Asai, S., Ishikawa, H., Honda, M., 1977. The kinetics of reactions of carbon dioxide with monoethanolamine, diethanolamine and triethanolamine by a rapid mixing method. Chem. Eng. J. 13, 7–12.

Izquierdo-Guerra, W., García-Reyes, E., 2010. Background Division, A Suitable Technique for Moving Object Detection, in: Iberoamerican Congress on Pattern Recognition. Springer Berlin Heidelberg, pp. 121–127.

Jimenez, M., Dietrich, N., Cockx, A., Hébrard, and G., 2013. Experimental study of O_2 diffusion coefficient measurement at a planar gas-liquid interface by planar laser-induced fluorescence with inhibition. AIChE J. 59, 325–333.

Jimenez, M., Dietrich, N., Grace, J.R., Hébrard, G., 2014. Oxygen mass transfer and hydrodynamic behaviour in wastewater: Determination of local impact of surfactants by visualization techniques. Water Res. 58, 111–21.

Kamholz, A.E., Schilling, E.A., Yager, P., 2001. Optical Measurement of Transverse Molecular Diffusion in a Microchannel. Biophys. J. 80, 1967–1972.

Karale, C.M., Bhagwat, S.S., Ranade, V. V., 2013. Flow and heat transfer in serpentine channels. AIChE J. 59, 1814–1827.

Kashid, M.N., Renken, A., Kiwi-Minsker, L., 2011. Gas–liquid and liquid–liquid mass transfer in microstructured reactors. Chem. Eng. Sci. 66, 3876–3897.

Kastens, S., Hosoda, S., Schlüter, M., Tomiyama, A., 2015. Mass Transfer from Single Taylor Bubbles in Minichannels. Chem. Eng. Technol. 38, 1925–1932.

Kherbeche, A., Milnes, J., Jimenez, M., Dietrich, N., Hébrard, G., Lekhlif, B., 2013. Multi-scale analysis of the influence of physicochemical parameters on the hydrodynamic and gas–liquid mass transfer in gas/liquid/solid reactors. Chem. Eng. Sci. 100, 515–528.

Ko, H.S., Gau, C., 2011. Local heat transfer process and pressure drop in a micro-channel integrated with arrays of temperature and pressure sensors. Microfluid. Nanofluidics 10, 563–577.

Kolb, W.B., Cerro, R.L., 1991. Coating the inside of a capillary of square cross section. Chem. Eng. Sci. 46, 2181–2195.

Kreutzer, M.T., Kapteijn, F., Moulijn, J. a., Heiszwolf, J.J., 2005. Multiphase monolith reactors: Chemical reaction engineering of segmented flow in microchannels. Chem. Eng. Sci. 60, 5895–5916.

Kuhn, S., Jensen, K.F., 2012. A pH-Sensitive Laser-Induced Fluorescence Technique To Monitor Mass Transfer in Multiphase Flows in Microfluidic Devices. Ind. Eng. Chem. Res. 51, 8999–9006.

Kurt, S.K., Warnebold, F., Nigam, K.D.P., Kockmann, N., 2017. Gas-liquid reaction and mass transfer in microstructured coiled flow inverter. Chem. Eng. Sci. 1–15.

Kuzmin, D., 2010. A guide to numerical methods for transport equations, University of Erlangen-Nuremberg. University of Erlangen-Nuremberg, Erlangen.

Leaist, D.G., 1988. The effects of aggregation, counterion binding, and added sodium chloride on diffusion of aqueous methylene blue. Can. J. Chem. 66, 2452–2457.

Leclerc, A., Philippe, R., Houzelot, V., Schweich, D., de Bellefon, C., 2010. Gas-liquid Taylor flow in square micro-channels: New inlet geometries and interfacial area tuning. Chem. Eng. J. 165, 290–300.

Leung, S.S.Y., Liu, Y., Fletcher, D.F., Haynes, B.S., 2010. Heat transfer in well-characterised Taylor flow. Chem. Eng. Sci. 65, 6379–6388.

Mohan, N., Rastogi, P., 2003. Recent developments in digital speckle pattern interferometry. Opt. Lasers Eng. 40, 439–588.

Nieves-Remacha, M.J., Kulkarni, A.A., Jensen, K.F., 2013. Gas–Liquid Flow and Mass Transfer in an Advanced-Flow Reactor. Ind. Eng. Chem. Res. 52, 8996–9010.

O'Brien, J., Wilson, I., Orton, T., Pognan, F., 2000. Investigation of the Alamar Blue (resazurin) fluorescent dye for the assessment of mammalian cell cytotoxicity. Eur. J. Biochem. 267, 5421–5426.

Pan, Z., Zhang, X., Xie, Y., Cai, W., 2014. Instantaneous Mass Transfer under Gas-Liquid Taylor Flow in Circular Capillaries. Chem. Eng. Technol. 37, 495–504.

Pelleter, J., Renaud, F., 2009. Facile, Fast and Safe Process Development of Nitration and Bromination Reactions Using Continuous Flow Reactors. Org. Process Res. Dev. 13, 698–705.

Pohorecki, R., Sobieszuk, P., Kula, K., Moniuk, W., Zielinski, M., Cyganski, P., Gawinski, P., 2008. Hydrodynamic regimes of gas–liquid flow in a microreactor channel. Chem. Eng. J. 135, S185–S190.

Qian, D., Lawal, A., 2006. Numerical study on gas and liquid slugs for Taylor flow in a T-junction microchannel. Chem. Eng. Sci. 61, 7609–7625.

Quinn, J. a., Lin, C.H., Anderson, J.L., 1986. Measuring diffusion coefficients by Taylor's method of hydrodynamic stability. AIChE J. 32, 2028–2033.

Robinson, C., 1935. The Diffusion Coefficients of Dye Solutions and their Interpretation. Proc. R. Soc. Lond. A. Math. Phys. Sci. 148, 681–695.

Roizard, C., Wild, G., Charpentier, J.-C., 1997. Absorption avec réaction chimique. TECHNIQUES DE L'INGÉNIEUR.

Roudet, M., Billet, A.-M., Cazin, S., Risso, F., Roig, V., 2017. Experimental investigation of interfacial mass transfer mechanisms for a confined high-reynolds-number bubble rising in a thin gap. AIChE J. 63, 2394–2408.

Roudet, M., Loubiere, K., Gourdon, C., Cabassud, M., 2011. Hydrodynamic and mass transfer in inertial gas–liquid flow regimes through straight and meandering millimetric square channels. Chem. Eng. Sci. 66, 2974–2990.

Roustan, M., 2003. Transferts gaz-liquide dans les procédés de traitement des eaux et des effluents gazeux, Dec&Doc Pa. ed.

Ruiz-Bevia, F., Fernandez-Sempere, J., Celdran-Mallol, A., Santos-Garcia, C., 1985. Liquid diffusion measurement by holographic interferometry. Can. J. Chem. Eng. 63, 765–771.

Shao, N., Gavriilidis, A., Angeli, P., 2009. Flow regimes for adiabatic gas–liquid flow in microchannels. Chem. Eng. Sci. 64, 2749–2761.

Shao, N., Gavriilidis, a., Angeli, P., 2010. Mass transfer during Taylor flow in microchannels with and without chemical reaction. Chem. Eng. J. 160, 873–881.

Shvydkiv, O., Limburg, C., Nolan, K., Oelgemöller, M., 2012. Synthesis of Juglone (5-Hydroxy-1,4-Naphthoquinone) in a Falling Film Microreactor. J. Flow Chem. 2, 52–55. 2

Sigma-Aldrich®. Product information.

Sobieszuk, P., Aubin, J., Pohorecki, R., 2012. Hydrodynamics and Mass Transfer in Gas-Liquid Flows in Microreactors. Chem. Eng. Technol. 35, 1346–1358.

Sobieszuk, P., Pohorecki, R., 2010. Gas-side mass transfer coefficients in a falling film microreactor. Chem. Eng. Process. Process Intensif. 49, 820–824.

Sobieszuk, P., Pohorecki, R., Cygański, P., Grzelka, J., 2011. Determination of the interfacial area and mass transfer coefficients in the Taylor gas–liquid flow in a microchannel. Chem. Eng. Sci. 66, 6048–6056.

Stankiewicz, A.I., Moulijn, J. a., 2000. Process Intensification : transforming chemical engineering. Chem. Eng. Prog. 22–34.

Su, Y., Hessel, V., Noël, T., 2015. A compact photomicroreactor design for kinetic studies of gas-liquid photocatalytic transformations. AIChE J. 61, 2215–2227.

Taha, T., Cui, Z.F., 2004. Hydrodynamics of slug flow inside capillaries. Chem. Eng. Sci. 59, 1181–1190.

Tan, J., Lu, Y.C., Xu, J.H., Luo, G.S., 2012a. Mass transfer performance of gas–liquid segmented flow in microchannels. Chem. Eng. J. 181–182, 229–235.

Tan, J., Lu, Y.C., Xu, J.H., Luo, G.S., 2012b. Mass transfer characteristic in the formation stage of gas–liquid segmented flow in microchannel. Chem. Eng. J. 185–186, 314–320.

Taylor, G., 1953. Dispersion of Soluble Matter in Solvent Flowing Slowly through a Tube. Proc. R. Soc. A Math. Phys. Eng. Sci. 219, 186–203.

Taylor, G.I., 1961. Deposition of a viscous fluid on a plane surface. J. Fluid Mech. 9, 218.

Théron, F., Anxionnaz-Minvielle, Z., Cabassud, M., Gourdon, C., Tochon, P., 2014. Characterization of the performances of an innovative heat-exchanger/reactor. Chem. Eng. Process. Process Intensif. 82, 30–41.

Thulasidas, T.C., Abraham, M.A., Cerro, R.L., 1997. Flow patterns in liquid slugs during bubble-train flow inside capillaries. Chem. Eng. Sci. 52, 2947–2962.

Tochon, P., Couturier, R., Anxionnaz, Z., Lomel, S., Runser, H., Picard, F., Colin, A., Gourdon, C., Cabassud, M., Peerhossaini, H., Della Valle, D., Lemenand, T., 2010. Toward a Competitive Process Intensification: A New Generation of Heat Exchanger-Reactors. Oil Gas Sci. Technol. – Rev. d'IFP Energies Nouv. 65, 785–792.

Trachsel, F., Günther, A., Khan, S., Jensen, K.F., 2005. Measurement of residence time distribution in microfluidic systems. Chem. Eng. Sci. 60, 5729–5737.

Triplett, K.A., Ghiaasiaan, S.M., Abdel-Khalik, S.I., Sadowski, D.L., 1999. Gas–liquid two-phase flow in microchannels Part I: two-phase flow patterns. Int. J. Multiph. Flow 25, 377–394.

Tsoligkas, A.N., Simmons, M.J.H., Wood, J., 2007. Influence of orientation upon the hydrodynamics of gas-liquid flow for square channels in monolith supports. Chem. Eng. Sci. 62, 4365–4378.

van Baten, J.M., Krishna, R., 2004. CFD simulations of mass transfer from Taylor bubbles rising in circular capillaries. Chem. Eng. Sci. 59, 2535–2545.

van Krevelen, D.W., Hoftijzer, P.J., 1948. Kinetics of gas-liquid reactions part I. General theory. Recl. des Trav. Chim. des Pays-Bas 67, 563–586.

Vandu, C.O., Liu, H., Krishna, R., 2005. Mass transfer from Taylor bubbles rising in single capillaries. Chem. Eng. Sci. 60, 6430–6437.

Völkel, N., 2009. Design and characterization of gas-liquid microreactors. Universite de Toulouse.

W.R.Dean, 1928. Fluid motion in a curved channel. Proc. R. Soc. London A Math. Phys. Eng. Sci. 121, 402–420.

Waelchli, S., Rudolf von Rohr, P., 2006. Two-phase flow characteristics in gas–liquid microreactors. Int. J. Multiph. Flow 32, 791–806.

Wang, X., Yong, Y., Yang, C., Mao, Z.-S., Li, D., 2014. Investigation on pressure drop characteristic and mass transfer performance of gas–liquid flow in micro-channels. Microfluid. Nanofluidics 16, 413–423.

Wilke, C.R., Chang, P., 1955. Correlation of diffusion coefficients in dilute solutions. AIChE J. 1, 264–270.

Winkler, L.W., 1888. Die Bestimmung des im Wasser gelösten Sauerstoffes. Berichte der Dtsch. Chem. Gesellschaft 21, 2843–2854.

Xiong, R., Chung, J.N., 2007. Flow characteristics of water in straight and serpentine micro-channels with miter bends. Exp. Therm. Fluid Sci. 31, 805–812.

Yang, L., Dietrich, N., Hébrard, G., Loubière, K., Gourdon, C., 2017a. Optical methods to investigate the enhancement factor of an oxygen-sensitive colorimetric reaction using microreactors. AIChE J. 63, 2272–2284.

Yang, L., Dietrich, N., Loubière, K., Gourdon, C., Hébrard, G., 2016. Visualization and characterization of gas–liquid mass transfer around a Taylor bubble right after the formation stage in microreactors. Chem. Eng. Sci. 143, 364–368.

Yang, L., Loubière, K., Dietrich, N., Le Men, C., Gourdon, C., Hébrard, G., 2017b. Local investigations on the gas-liquid mass transfer around Taylor bubbles flowing in a meandering millimetric square channel. Chem. Eng. Sci. 165, 192–203.

Yang, L., Tan, J., Wang, K., Luo, G., 2014. Mass transfer characteristics of bubbly flow in microchannels. Chem. Eng. Sci. 109, 306–314.

Yano, T., 1998. Electrochemical Behavior of Highly Conductive Boron-Doped Diamond Electrodes for Oxygen Reduction in Alkaline Solution. J. Electrochem. Soc. 145, 1870.

Yao, C., Dong, Z., Zhao, Y., Chen, G., 2015. Gas-liquid flow and mass transfer in a microchannel under elevated pressures. Chem. Eng. Sci. 123, 137–145.

Yao, C., Dong, Z., Zhao, Y., Chen, G., 2014. An online method to measure mass transfer of slug flow in a microchannel. Chem. Eng. Sci. 112, 15–24.

Yoshida, J., 2015. Basics of Flow Microreactor Synthesis, SpringerBriefs in Molecular Science. Springer Japan, Tokyo.

Yue, J., Chen, G., Yuan, Q., Luo, L., Gonthier, Y., 2007. Hydrodynamics and mass transfer characteristics in gas–liquid flow through a rectangular microchannel. Chem. Eng. Sci. 62, 2096–2108.

Yue, J., Luo, L., Gonthier, Y., Chen, G., Yuan, Q., 2009. An experimental study of air–water Taylor flow and mass transfer inside square microchannels. Chem. Eng. Sci. 64, 3697–3708.

Zaloha, P., Kristal, J., Jiricny, V., Völkel, N., Xuereb, C., Aubin, J., 2012. Characteristics of liquid slugs in gas–liquid Taylor flow in microchannels. Chem. Eng. Sci. 68, 640–649.

Zhang, Y., Song, P., Fu, Q., Ruan, M., Xu, W., 2014. Single-molecule chemical reaction reveals molecular reaction kinetics and dynamics. Nat. Commun. 5, 4238.

Zhao, Y., Su, Y., Chen, G., Yuan, Q., 2010. Effect of surface properties on the flow characteristics and mass transfer performance in microchannels. Chem. Eng. Sci. 65, 1563–1570.

Zhu, C., Li, C., Gao, X., Ma, Y., Liu, D., 2014. Taylor flow and mass transfer of CO_2 chemical absorption into MEA aqueous solutions in a T-junction microchannel. Int. J. Heat Mass Transf. 73, 492–499.

Zuber, N., Findlay, J.A., 1965. Average Volumetric Concentration in Two-Phase Flow Systems. J. Heat Transfer 87, 453–468.

APPENDICES

Appendix A

Details of image processing

Let $GV(x,y,t)$ be the grey level of a pixel with coordinates x, y of an untreated raw image at time t. As shown in **Fig. A-1** (a), this grey level is darkest at the bubble surface and lightest in the region free of oxygen, the intermediate grey levels being linked to the different coloured forms taken by the dye solution in presence of oxygen. The purpose of the present section is to extract an accurate quantification of the oxygen transferred from the raw images. For this purpose, an image processing technique had to be developed, which mainly identified the boundaries demarcating these three ranges of grey levels.

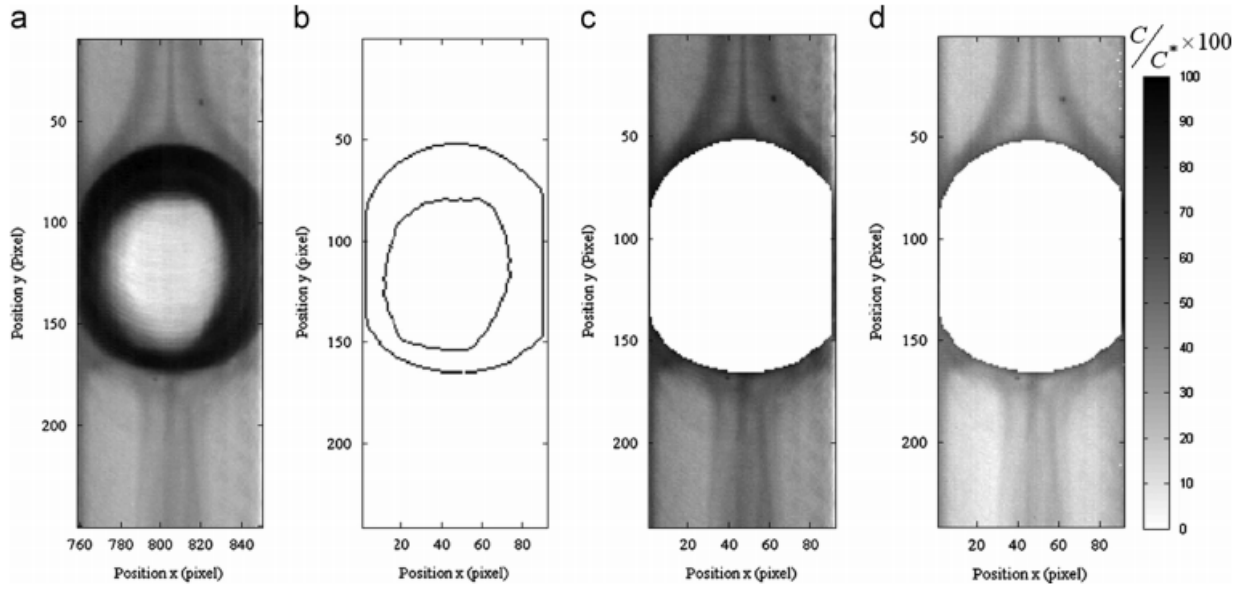

Fig. A-1 Image processing: (a) raw image; (b) detection of the bubble contour; (c) corrected image after subtracting the contribution of background and noise, and masking the bubble; (d) equivalent oxygen concentration field obtained after applying the calibration curve. The experiments were conducted with a concentration of resazurin of 0.1 $g \cdot L^{-1}$. Adapted from Dietrich et al. (2013a)

The first step was the characterization of the “lightest” region mentioned above, a zone without bubbles or mass transfer. For all experiments, the positions of the camera, LitePad backlight and channel remained unchanged and there was no alteration of the “uncoloured” form of the dye. Consequently, the grey levels corresponding to this “no-transfer zone” should theoretically remain constant from one recorded image to another. In practice, a variation of less than 3 grey levels was observed in this zone over the whole set of recorded images. Based on this observation, a reference image, determined by averaging 20 images without bubbles, was considered and subtracted from the raw images. The average grey level of the corrected image background thus became close to 0.

From the resulting image, a threshold was fixed to determine the boundary between mass transfer and noise. Then, all the grey levels lighter than this threshold were considered as noise and set to 0. This threshold is chosen in such a way that the remaining noise is minimized while ensuring that the mass transfer is not disrupted. It has been found that twice the standard deviation is the optimal threshold for the most considered cases. Then, all the pixels whose grey level is below this threshold are considered as noise and their value is set to 0. The following step of the image processing concerned the second extreme values of grey levels, namely the “darkest” ones, corresponding to the bubble surface. The Canny edge detector algorithm (extracted from the Image Processing ToolBox in Matlab®), was used to determine the bubble contours. It is mainly based on the location of local maximum gradients of grey levels for a given image, to which a Gaussian filter has previously been applied to reduce the noise level. The larger the gradient is, the more likely it is that the pixel represents an edge. Then a thresholding procedure with hysteresis is considered to determine whether the pixel is an edge or not. For further details about this method, the reader is invited to consult (Canny, 1986). An example of edge detection using the Canny detector is shown in **Fig. A-1** (b). It can be observed that two circular edges have been detected: the largest one describes the global shape of the bubble and enables the bubble diameter to be determined, whereas the second edge is due to the bubble part in contact with the square channel and under a strong light due to the backlight positioned behind the recorded bubble. Finally, to cancel this rear reflect, each pixel belonging to the largest detected edge is considered as belonging to the bubble and its corresponding grey value is then

set to 0. **Fig. A-1** (c) represents the corrected image after application of the bubble mask. The grey level of the corrected image is noted $GV^*(x,y,t)$.

Thanks to this image processing, the pixels on the final corrected image which had non null values of grey levels could be directly attributed to the quantity of oxygen transferred per unit of liquid volume. By considering a pixel-by-pixel summation on the remaining grey levels and applying the calibration curve mentioned above, an accurate quantification of the oxygen transferred by bubbles was possible (see **Fig. A-1** d).

The following reports a general Matlab script for the image processing procedure.

General Matlab script:

```
I=imread('1.tif'); bcg=imread('background.tif'); % read the raw image and
background image
I1=bcg-I; %subtraction of the background
I1=imcomplement(I1);
figure(1); imshow(I1);title('bubbles');

p=ginput(2); %choose the investigated region
A = I1(p(1,2):p(2,2) , p(1,1):p(2,1));
figure(2); imshow(A);title('bubbles');
thresh=graythresh(A);
contour=edge(A,'canny',thresh); % detect the contour of the bubble
figure(3); imagesc(contour); axis image;

for i=1:size(contour,1)
  if sum(contour(i,:)~=0)
  [Jmin]=find(contour(i,:)==1,1);
  [Jmax]=find(contour(i,:)==1,1,'last');
  A(i,Jmin:Jmax)=255;
  end
end
figure(4);colormap(gray(256));image(A);axis image; % mask the bubble

[m,n]=size(A);
C_O2_ratio= 0.0912*AA/8.15; % apply the calibration curve
B=C_O2_ratio*255;
figure(5); imagesc(B); axis image; title('equivalent O2 concentration') %
equivalent concentration of O2
```

Appendix B

Data of Sh_X as a function of Gz_X

Table B-1 Data of Sh_X as a function of Gz_X under all operating conditions in straight channel.

j_L (m·s^{-1})	j_G (m·s^{-1})	L_S/l	Pe	X (m)	Gz_X	Sh_X	j_L (m·s^{-1})	j_G (m·s^{-1})	L_S/l	Pe	X (m)	Gz_X	Sh_X
				0.02	9809	2144					0.02	13451	2873
				0.07	2803	1013					0.07	3843	1141
				0.12	1635	833					0.12	2242	1110
0.069	0.014	6.26	132090	0.17	1189	750	0.139	0.014	7.59	134514	0.17	1630	933
				0.19	1033	692					0.19	1416	944
				0.20	981	676					0.20	1345	933
				0.32	613	405					0.32	841	562
				0.02	11568	1397					0.02	15671	1917
				0.07	3305	674					0.07	4478	979
				0.12	1928	531					0.12	2612	694
0.069	0.028	3.94	115680	0.17	1402	448	0.139	0.028	4.73	156714	0.17	1900	626
				0.19	1218	432					0.19	1650	614
				0.20	1157	428					0.20	1567	618
				0.32	723	251					0.32	979	375
				0.02	16109	1148					0.02	19759	2455
				0.07	4603	582					0.07	5645	1428
				0.12	2685	456					0.12	3293	998
0.069	0.042	3.24	161094	0.17	1953	377	0.139	0.042	3.72	197587	0.17	2395	841
				0.19	1696	361					0.19	2080	855
				0.20	1611	359					0.20	1976	843
				0.32	1007	199					0.32	1235	478
				0.02	26494	1274					0.02	28767	2046
				0.07	7570	695					0.07	8219	1147
				0.12	4416	508					0.12	4794	898
0.069	0.069	2.71	264936	0.17	3211	405	0.139	0.069	2.63	287670	0.17	3487	689
				0.19	2789	382					0.19	3028	662
				0.20	2649	372					0.20	2877	648
				0.32	1656	211					0.32	1798	386
				0.02	60503	1916					0.02	51997	2727
				0.07	17287	960					0.07	14856	1606
				0.12	10084	694					0.12	8666	1172
0.069	0.139	1.90	605034	0.17	7334	524	0.139	0.139	1.93	519965	0.17	6303	873
				0.19	6369	508					0.19	5473	826
				0.20	6050	494					0.20	5200	806
				0.32	3781	281					0.32	3250	476
											0.02	81001	3602
											0.07	23143	2326
											0.12	13500	1427
							0.139	0.208	1.72	810011	0.17	9818	1101
											0.19	8526	1019
											0.20	8100	1000
											0.32	5063	577

(continued)

j_L (m·s^{1})	j_G (m·s^{-1})	L_S/l	Pe	X (m)	Gz_X	Sh_X		j_L (m·s^{1})	j_G (m·s^{-1})	L_S/l	Pe	X (m)	Gz_X	Sh_X
				0.02	15638	2938						0.02	28073	2838
				0.07	4468	1303						0.07	8021	1691
				0.12	2606	1134						0.12	4679	1330
0.208	0.014	5.50	156382	0.17	1896	1107		0.208	0.069	2.49	280728	0.17	3403	1069
				0.19	1646	1209						0.19	2955	1020
				0.20	1564	1227						0.20	2807	1005
				0.32	977	783						0.32	1755	631
				0.02	18947	3324						0.02	50641	2835
				0.07	5413	1594						0.07	14469	1895
				0.12	3158	1213						0.12	8440	1435
0.208	0.028	4.08	189470	0.17	2297	1162		0.208	0.139	1.98	506412	0.17	6138	1065
				0.19	1994	1236						0.19	5331	1013
				0.20	1895	1232						0.20	5064	1009
				0.32	1184	818						0.32	3165	628
				0.02	21826	2706						0.02	78514	3487
				0.07	6236	1749						0.07	22433	2363
				0.12	3638	1249						0.12	13086	1733
0.208	0.042	3.15	218258	0.17	2646	1177		0.208	0.208	1.90	785138	0.17	9517	1327
				0.19	2297	1125						0.19	8265	1222
				0.20	2183	1148						0.20	7851	1216
				0.32	1364	700						0.32	4907	730

Table B-2 Data of Sh_X as a function of Gz_X under all operating conditions in meandering channel.

j_L (m·s^{1})	j_G (m·s^{-1})	L_S/l	Pe	X (m)	Gz_X	Sh_X		j_L (m·s^{1})	j_G (m·s^{-1})	L_S/l	Pe	X (m)	Gz_X	Sh_X
				0.02	9897	3750						0.02	14502	2933
				0.07	2828	1854						0.07	4143	1669
				0.12	1650	1518						0.12	2417	1375
0.069	0.014	5.64	98972	0.17	1164	1154		0.104	0.028	3.98	145017	0.17	1706	1167
				0.22	900	1257						0.22	1318	1108
				0.32	619	940						0.32	906	821
				0.42	471	766						0.42	691	670
				0.02	14014	2338						0.02	20569	2847
				0.07	4004	1237						0.07	5877	1634
				0.12	2336	863						0.12	3428	1255
0.069	0.028	3.17	140143	0.17	1649	656		0.104	0.042	3.02	205687	0.17	2420	1003
				0.22	1274	570						0.22	1870	947
				0.32	876	459						0.32	1286	690
				0.42	667	372						0.42	979	570
				0.02	19120	2151						0.02	27115	2774
				0.07	5463	1281						0.07	7747	1699
				0.12	3187	848						0.12	4519	1290
0.069	0.042	2.41	191198	0.17	2249	697		0.104	0.069	2.16	271153	0.17	3190	1015
				0.22	1738	581						0.22	2465	926
				0.32	1195	466						0.32	1695	657
				0.42	910	384						0.42	1291	520
				0.02	30491	2470						0.02	70366	2941
				0.07	8712	1389						0.07	20105	2151
				0.12	5082	976						0.12	11728	1774
0.069	0.069	1.82	304911	0.17	3587	744		0.104	0.139	1.78	703659	0.17	8278	1377
				0.22	2772	661						0.22	6397	1149
				0.32	1906	473						0.32	4398	816
				0.42	1452	374						0.42	3351	658
				0.02	57015	2117								
				0.07	16290	1506								
				0.12	9503	1078								
0.069	0.139	1.45	570154	0.17	6708	842								
				0.22	5183	717								
				0.32	3563	515								
				0.42	2715	407								

(continued)

j_L ($m \cdot s^{-1}$)	j_G ($m \cdot s^{-1}$)	L_S/l	Pe	X (m)	Gz_X	Sh_X	j_L ($m \cdot s^{-1}$)	j_G ($m \cdot s^{-1}$)	L_S/l	Pe	X (m)	Gz_X	Sh_X
				0.02	18249	4334					0.02	58037	3492
				0.07	5214	2483					0.07	16582	2226
				0.12	3041	1756					0.12	9673	1575
0.139	0.042	3.20	182486	0.17	2147	1450	0.139	0.139	1.84	580372	0.17	6828	1240
				0.22	1659	1304					0.22	5276	1107
				0.32	1141	931					0.32	3627	776
				0.42	869	756					0.42	2764	633
				0.02	27425	3709					0.02	99177	2733
				0.07	7836	2128					0.07	28336	2476
				0.12	4571	1528					0.12	16530	1735
0.139	0.069	2.11	274247	0.17	3226	1205	0.139	0.208	1.96	991771	0.17	11668	1404
				0.22	2493	1109					0.22	9016	1229
				0.32	1714	806					0.32	6199	877
				0.42	1306	634					0.42	4723	690